

UNIVERSITÀ
DEGLI STUDI
DI PADOVA

Sede Amministrativa: Università degli Studi di Padova
Dipartimento di Scienze Chimiche

Scuola di Dottorato di Ricerca in Scienza e Ingegneria dei Materiali
XXIV ciclo

Synthesis and Engineering of *Easy&Cheap* Silver Based Optical Sensors

Direttore della Scuola: Ch.mo Prof. Gaetano Granozzi

Supervisore: Prof. Gian Andrea Rizzi

Dottorando: Giuseppe Giallongo

*Real progress happens only
when advantages of a new technology
become available to everybody*

Henry Ford

Abstract

Nel corso degli ultimi decenni la sensoristica ottica ha assunto un ruolo di primaria importanza in campo analitico. In particolare, la plasmonica, ovvero quella branca della sensoristica che sfrutta l'eccitazione dei *plasmoni di superficie*, dovuta all'oscillazione collettiva degli elettroni in banda di conduzione, ha permesso di raggiungere risultati eccellenti in termini di limiti di rivelabilità e accuratezza. Questo tipo di sensoristica sfrutta l'interazione tra le nanoparticelle metalliche che godono di proprietà plasmoniche (Au, Ag, Cu) e le molecole interagenti. Infatti, in condizioni di risonanza, si sviluppa sulla superficie della nanostruttura un fortissimo campo elettrico localizzato che, interagendo con una molecola posizionata all'interfaccia, può amplificare o attenuare le sue proprietà ottiche.

In questa tesi sono state esplorate diverse metodiche di sintesi di substrati basati su nanostrutture di argento, ordinate e non, su film sottile per applicazioni in Sensoristica Raman e UV-Visibile (LSPR). I campioni sono stati caratterizzati dal punto di vista chimico, fisico e morfologico e sono stati testati sistematicamente per valutarne l'efficienza e la qualità.

Nella prima fase della tesi sono stati preparati dei campioni su substrati di basso costo e facilmente reperibili. A tale scopo sono stati utilizzati dei DVD scrivibili disponibili in commercio, che contengono una distribuzione a spirale di scanalature di forma rettangolare ricoperte da un film sottile di Ag (AgDVD): per la prima volta sono stati usati per produrre substrati per *surface-enhanced Raman scattering* (SERS) tramite deposizione elettrochimica di nanoparticelle di Ag (AgNPs@AgDVD). La procedura generale richiede solo materiali economici, ampiamente disponibili e può essere facilmente realizzata. Le immagini effettuate tramite *Scanning*

electron microscopy (SEM) mostrano che nelle valli dell'AgDVD sono presenti piccole nanoparticelle di Ag (Ag NPs, diametro medio di circa 15 nm), mentre sulle creste, le Ag NPs sono più grandi, più densamente impaccate e in alcune zone presentano una morfologia di tipo dendritico. Le proprietà SERS di questi substrati sono state studiate in termini di *enhancement factor* (EF), di ripetibilità da punto a punto e di riproducibilità da campione a campione. Si è scoperto che i requisiti di alti SERS EF e di una buona riproducibilità sono entrambi soddisfatti. Per quanto riguarda la ripetibilità, sono stati raggiunti risultati di gran lunga migliori rispetto ai valori tipici riportati in letteratura. Tale preparazione *easy&cheap* con efficienti proprietà SERS rende i substrati SERS derivati dai DVD ottimi candidati per lo sviluppo di sensori convenienti e monouso.

Nella seconda fase della tesi sono state cresciute nanostrutture di Ag (Ag NSs) mediante elettrodeposizione in corrente alternata utilizzando come *template* delle membrane di allumina nanoporosa (AAO) direttamente connesse al substrato metallico. A seconda dello spessore del template e del voltaggio applicato durante il processo di crescita è possibile ottenere differenti Ag NSs con differenti proprietà ottiche. Quando si usano AAO da circa 1 μm di spessore, le nanostrutture che si formano sono nanobarre di Ag (Ag NRs), alla base dei pori, e nanotubi di Ag (Ag NTs) che partono dalle nanobarre e riempiono il poro in quasi tutta la sua lunghezza. Quando si usano AAO da circa 3 μm di spessore, le nanostrutture che si formano sono sferoidi, alla base dei pori, e nanofili di Ag (Ag NWs) che non raggiungono la parte superiore dei pori dell'allumina. Nel caso delle AAO da circa 1 μm di spessore, un semplice trattamento di erosione in NaOH, seguito da sonicazione in etanolo, permette di ottenere una disposizione ordinata (array) di Ag NRs, adatta per il SERS, mentre nell'altro caso (per le AAO da 3 μm di spessore) i campioni possono essere utilizzati per misure di *Localized Surface Plasmon Resonance sensing* (LSPR).

La procedura di elettrodeposizione in corrente alternata è stata estesa anche al rame al fine di ottenere Cu NSs da utilizzare come anodi sacrificali per la successiva deposizione di Ag.

Anche in questo caso i campioni sono stati caratterizzati chimicamente, fisicamente e morfologicamente ed infine testati come sensori.

Infine sono stati preparati dei substrati SERS tramite deposizione elettroforetica (EPD) di Ag NPs. La sospensione colloidale di Ag NPs è stata preparata utilizzando semplicemente $[\text{Ag}(\text{NH}_3)_2]^+$ come precursore d'argento e glucosio come agente riducente. Questa semplice "sintesi verde" permette di ottenere una sospensione di Ag NPs con una buona monodispersione dimensionale e buone prestazioni ottiche. Le Ag NPs ottenute sono caratterizzate da un potenziale z negativo e quindi adatte per l'EPD. La stabilità della sospensione, ottenuta in questo modo semplice, è garantita dalla "protezione" offerta dall'acido gluconico adsorbito sulle Ag NPs, che si forma durante la reazione redox tra il complesso $[\text{Ag}(\text{NH}_3)_2]^+$ e il glucosio. Grazie alla protezione offerta dall'acido gluconico le Ag NPs mantengono la loro dimensione originaria anche dopo l'EPD. Inoltre, le molecole che si legano più fortemente all'Ag, come tioli o ammine, possono facilmente sostituire l'acido gluconico adsorbito sulla superficie delle Ag NPs (interazione debole). Tali campioni sono stati caratterizzati tramite XPS, SEM, UV-Vis e infine sono stati testati come substrati SERS.

Abstract

Over the last decades optical sensors assumed a major role in the analytical field. In particular, *plasmonics*, that is the branch of sensors that exploits the excitation of *surface plasmons* due to the collective oscillation of the electrons in the conduction band, allowed to achieve excellent results in terms of detection limits and accuracy. This kind of sensors exploits the interaction between the metal nanoparticles that possess plasmonic properties (Au, Ag, Cu) and an interacting molecules. In fact, under resonance conditions, a strong localized electric field is produced on the surface of the nanostructure, that, by the interaction with a molecule located at the interface, may amplify or attenuate its optical properties.

In this thesis various methods of synthesis of substrates based on silver nanostructures, ordered or otherwise, as thin films for applications in Raman and UV-Visible (LSPR) sensors were explored. The samples were characterized in terms of chemical, physical and morphological properties and were systematically tested to assess their efficiency and quality.

In the first part of the thesis, commercially available digital versatile discs (DVDs) were used to fabricate SERS easy&cheap substrates. DVDs contain a silver-coated spiral distribution of rectangular-shaped grooves (AgDVD): for the first time, they were used to produce surface-enhanced Raman scattering (SERS) substrates by electrochemical deposition of silver nanoparticles (AgNPs@AgDVD). The overall procedure only requires cheap and widely available materials and can be easily accomplished. Scanning electron microscopy images of AgNPs@AgDVD revealed that small Ag NPs (average diameter about 15 nm) are present within the valleys of AgDVD, whereas over the ridges, the Ag NPs are bigger, more densely packed and with a

dendrite-like morphology somewhere. The SERS properties of these substrates were studied in terms of the enhancement factor (EF), point-to-point reproducibility and sample-to-sample repeatability. It turned out that high SERS EF and good reproducibility are both fulfilled. As for repeatability, remarkably better results than typical literature values were achieved. Such an easy&cheap preparation along with efficient SERS properties make DVD-derived SERS substrates very good candidates for the development of convenient and disposable sensing platforms.

In the second part of the thesis, Ag nanostructures (Ag NSs) were grown by AC electrodeposition on Anodic Alumina Oxide (AAO) connected membranes acting as templates. Depending on the thickness of the template and on the voltage applied during the growth process, different Ag NSs with different optical properties were obtained. When ca 1 μm thick AAO membranes are used, the Ag NSs consist in Ag nanorods, at the bottom of the pores, and Ag nanotubes (Ag NTs) departing from the nanorods and filling the pores almost for the whole length. When ca 3 μm thick AAO membranes are used, the nanostructures are Ag spheroids, at the bottom of the pores, and Ag nanowires (Ag NWs) that do not reach the upper part of the alumina pores. The samples were characterized by Angle Resolved X-Ray Photoelectron Spectroscopy, Scanning Electron Microscopy measurements and UV-Vis and Raman Spectroscopies. In the case of μm thick AAO membranes, a simple NaOH etching procedure, followed by sonication in ethanol, allows one to obtain an exposed ordered array of Ag nanorods (Ag NRs), suitable for Surface Enhanced Raman Spectroscopy, while in the other case (3 μm thick AAO membranes) the sample can be used in Localized Surface Plasmon Resonance sensing.

The AC electrodeposition procedure was extended to copper in order to obtain Cu NSs to be used as sacrificial anodes for the subsequent deposition of Ag.

Also in this case the samples were chemically, physically and morphologically characterized and finally tested as sensors.

Finally, SERS substrates were produced by electrophoretic deposition (EPD) of Ag NPs. The Ag NPs colloidal suspension was prepared by simply using $[\text{Ag}(\text{NH}_3)_2]^+$ as silver source and glucose as reducing agent. This simple

“green synthesis” allows to obtain an Ag NPs suspension with a good dimensional monodispersion and good optical performances. The obtained Ag NPs are characterized by a negative z-potential and therefore suitable for EPD. The stability of the suspension, obtained by this simple way, is guaranteed by the “protection” of the adsorbed gluconic acid on the Ag NPs surface, that forms during the redox reaction between the $[\text{Ag}(\text{NH}_3)_2]^+$ complex and glucose. Because of the gluconic acid protection the Ag NPs maintain their original dimension even after the EPD. Moreover, molecules that bind more strongly to Ag, like thiols or amines, can easily substitute the gluconic acid adsorbed on the Ag NPs surface (weak interaction). Such samples were characterized by XPS, SEM, UV-Vis and finally tested as SERS substrates.

Contents

Chapter 1

Introduction	1
1.1 Optical properties at nanoscale	1
1.2 Plasmonics	2
1.3 Nanotechnology and Plasmonics	3
1.4 Silver and its Amazing Plasmonics Properties	5
1.5 Template Assisted Nanotextured Arrays	9
1.6 Anodic Alumina Oxide Templates	10
1.7 Ultra-Thin Alumina Masks	14
1.8 Electromagnetic Field Enhancement in Ordered Arrays	17
1.9 Aim of the thesis	19
References	21

Chapter 2

Nanomaterials characterization techniques	25
2.1 X-Ray Photoelectron Spectroscopy	25
2.1.1 The Auger parameter	28
2.2 Scanning Electron Microscopy	29
2.3 Transmission Electron Microscopy	32
2.4 Atomic Force Microscopy	34
2.5 Surface Enhancement Raman Spectroscopy	36
2.5.1 Technique and fundamental relations of SERS	37
2.5.2 Experimental set up for SERS	39

2.6 Diffuse Reflectance Spectroscopy	41
References	43

Chapter 3

Silver nanoparticle arrays on a DVD derived template: an easy&cheap SERS substrate	45
3.1 Introduction	45
3.2 Experimental Section	47
3.2.1 Substrates preparation	47
3.2.2 Morphological and chemical characterization	48
3.2.3 Optical measurements	49
3.3 Results and discussion	50
3.3.1 Preparation and characterization of the substrate	50
3.4 Optical measurements	54
3.4.1 Diffuse Reflectance Measurements	54
3.4.2 Surface Enhanced Raman Scattering Measurements	55
3.5 Conclusions	60
References	62

Chapter 4

Growth and optical properties of Silver Nanostructures obtained on Connected Anodic Aluminum Oxide Templates	65
4.1 Introduction	65
4.2 Experimental Section	68
4.3 Results and Discussion	70
4.3.1 AAO preparation by anodization and AC electrodeposition of Ag	70
4.3.2 SEM and AR-XPS characterization of the Ag nanostructures	73

4.3.3 Optical characterization of the Ag NSs arrays	79
4.4 Discrete Dipole Approximation Study on Ag NRs	82
4.4.1 Discrete Dipole Approximation Model	82
4.4.2 Results of DDA calculation on Ag NRs Arrays	84
4.5 Ag@Cu Nanostructures grown into AAO	86
4.5.1 Experimental section	86
4.5.2 Results and discussion	88
4.6 Conclusions	91
References	93

Chapter 5

“Green Synthesis” and electrophoretic deposition of Ag nanoparticle on SiO₂/Si(100)	97
5.1 Introduction	97
5.2 Experimental Section	99
5.3 Results and Discussion	101
5.3.1 Optical and Morphological characterization of as-prepared Ag NPs colloidal suspension	101
5.3.2 Preparation and characterization of the AgEPD substrates	108
5.3.3 Optical characterization	114
5.4 Conclusions	118
References	119

Chapter 6

Conclusions	121
--------------------	-----

Chapter 1

Introduction

1.1 Optical properties at nanoscale

Today noble metals, such as Au, Ag, and Cu, are widely used in electronics, catalysis and as structural materials, but when they form structures with nanometer-sized dimensions, they become suitable for a completely different set of applications that involve light. These new applications go far beyond merely reflecting light and have renewed our interest in maneuvering the interactions between metals and light in a field known as plasmonics.¹ In plasmonics, metal nanostructures can serve as antennas to convert light into localized electric fields (E-fields) or as waveguides to route light to desired locations with nanometer precision. These applications are made possible through a strong interaction between incident light and free electrons in the nanostructures. By controlling the nanostructures in terms of size and shape, light can be effectively manipulated and controlled with unprecedented accuracy.^{2,3} Although many new technologies stand to be realized from plasmonics, with notable examples including superlenses,⁴ invisibility cloaks,⁵ and quantum computing,^{6,7} conventional technologies like microprocessors and photovoltaic devices could also be made significantly faster and more efficient with the integration of plasmonic nanostructures.^{8,9} Among transition metals, Ag and Au have probably played the most important role in the development of plasmonics, and their unique properties make them well-suited for most of the next-generation plasmonic technologies.^{10,11}

1.2 Plasmonics

Plasmonics is related to the localization, guiding, and manipulation of electromagnetic waves beyond the diffraction limit and down to the nanometer-length scale.^{12,13} The key component of plasmonics is a noble metal, because it supports surface plasmon polariton modes (SPs), which are electromagnetic waves coupled to the collective oscillations of free electrons. Although there are a rich variety of plasmonic metal nanostructures, they can be differentiated based on the plasmonic modes they support: localized surface plasmons (LSPs) or propagating surface plasmons (PSPs).^{14,15} In LSPs, the time-varying electric field associated with the light (E_o) exerts a force on the gas of negatively charged electrons in the conduction band of the metal and drives them to oscillate collectively. At a certain excitation frequency (ω), this oscillation will be in resonance with the incident light, resulting in a strong oscillation of the surface electrons, commonly known as a localized surface plasmon resonance (LSPR) mode.¹⁶

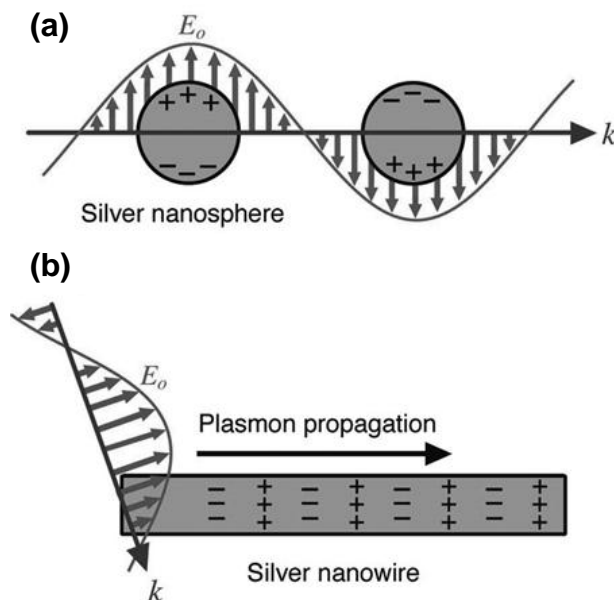


Figure 1.1. Schematic illustration of the interaction between plasmonic nanostructures and light with electric field E_o and wavevector k . In (a) the nanostructure is smaller than the wavelength, and the free electrons can be displaced from the lattice of positive ions (consisting of nuclei and core electrons) and collectively oscillate in resonance with the light. This is known as a localized surface plasmon resonance (LSPR). In (b) the nanowire has one dimension much larger than the wavelength of light. In this case, light coupled to the nanostructure will excite the free electrons to create a propagating surface plasmon (PSP) that can travel along the surface of the metal nanostructure.

This phenomenon is illustrated in **Figure 1.1a**. Structures that support LSPRs experience a uniform E_0 when excited by light as their dimensions are much smaller than the wavelength of the light. In contrast, PSPs are supported by structures that have at least one dimension that approaches the excitation wavelength, as shown in Figure 1.1b.¹⁷ In this case, the E_0 is not uniform across the structure and other effects must be considered. In such a structure, like a nanowire for example, SPs propagate back and forth between the ends of the structure (see **Figure 1.2**). This can be described as a Fabry-Perot resonator with resonance condition $l = n\lambda_{sp}$, where l is the length of the nanowire, n is an integer, and λ_{sp} is the wavelength of the PSP mode.^{18,19} Reflection from the ends of the structure must also be considered, which can change the phase and resonant length. Propagation lengths can be in the tens of micrometers (for nanowires), and the PSP waves can be manipulated by controlling the geometrical parameters of the structure.²⁰

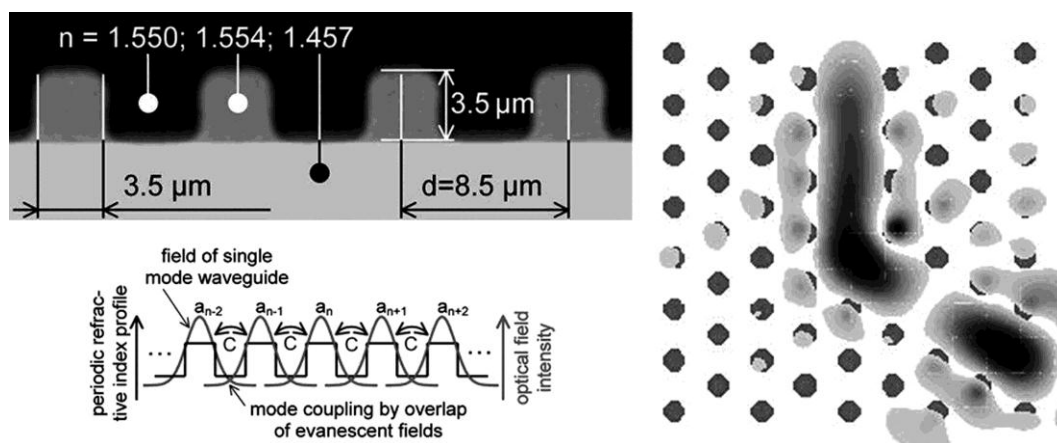


Figure 1.2 Silver Nanorods waveguide

1.3 Nanotechnology and Plasmonics

In the past, the ability to focus light was solely in the realm of dielectric materials. These materials, however, cannot localize light to areas smaller than half a wavelength of light ($\lambda/2$) or confine electromagnetic modes to volumes less than $(\lambda/2)^3$. In contrast, surface plasmon modes are primarily limited by the size of the plasmonic structure that supports them: a nanostructure can thereby focus and guide light down to the nanometer

regime. By tailoring the size, shape, and environment of a metal nanostructure, light can be manipulated in many unique ways.^{21,22} It is no surprise that recent advances in the preparation and assembly of metal nanostructures have opened new doors to the precise manipulation and control of light and, consequently, to applications that were previously considered impossible.²³ As an optical phenomenon, SPs have been known for more than 150 years, with the first demonstration being documented by Michael Faraday in 1857.¹ Its connection with nanoscale science and technology was not widely or actively explored until recently.²⁴ Plasmonics is part of nanotechnology because nanostructures are used as active components to focus, guide, and manipulate light and as building blocks for larger, more complex “metamaterials” sought for controlling light. Although the interaction of light and metal nanoparticles has long attracted the interest of scientists, plasmonics represents a relatively new level of control and study involving both nanostructures and light. In contrast to simply establishing the valuable optical properties of metal nanostructures, this interaction is now controlled for the specific purpose of manipulating the propagation of light. Plasmonics is also a very interesting field of nanoscience because sophisticated models, theories, and methods are being developed to understand the interaction between a metal nanostructure and light.^{25,26} Plasmonics is also different from many past applications and studies of nanoparticles that rely on the material properties of the nanostructure or its small size. These nonplasmonic applications include, for example, electron confinement,²⁷ electron tunneling,²⁸ ballistic transport,²⁹ and superparamagnetism.³⁰ In contrast to these applications, plasmonics requires a coupling between an electromagnetic wave and the metal nanostructure to generate a surface plasmon. Without incident light, the structure does not have a plasmonic function. More importantly, plasmonics is unique in that it can use nanostructures of many different sizes (tens to hundreds of nanometers) and thus bridge the gap between the micrometer and nanometer levels. This is best seen in the example of Ag nanowires, which can guide light at deep subwavelength scales over micrometer distances.²⁰ Plasmonics is therefore a new subfield of nanoscale science and

technology that aims to understand and control light using metal nanostructures in novel ways.

1.4 Silver and its Amazing Plasmonics Properties

Silver is probably the most important material in plasmonics. It offers many advantages over Au, Cu, Li, and Al other metals known to support SPs in the visible (vis) and near-infrared regions (NIR).^{10,31} In terms of plasmonics, it is important to choose a metal that can support a strong SP at the desired resonance wavelength.^{32,33} Silver is able to do so across the spectrum from 300 to 1200 nm. The ability of a metal nanoparticle to support a SP is dependent on its dielectric function ϵ , which includes a real part (ϵ_r) and an imaginary part (ϵ_i), both of which vary with excitation wavelength (λ). The dielectric function of a material reflects the unique interaction between its electrons and the light. The simplest way to describe LSPR can be found in Mie theory for calculating the extinction (absorption + scattering) cross section of a metal nanosphere:

$$C_{\text{ext}} = \frac{24\pi^2 R^3 \epsilon_m^{3/2}}{\lambda} \left[\frac{\epsilon_i}{(\epsilon_r + 2\epsilon_i)^2 + \epsilon_i^2} \right] \quad (1.1)$$

where C_{ext} is the extinction cross section, R is the nanosphere radius, and ϵ_m is the relative dielectric constant of the medium surrounding the nanosphere. This equation shows that the interaction between a metal nanoparticle and light depends strongly on its dielectric properties (ϵ_r and ϵ_i). Although other factors are also important, from an engineering perspective, the material properties of the plasmonic structure are the key, as the environment and other parameters (like excitation wavelength) are often fixed. When the denominator of the bracketed expression in equation 1.1 approaches zero, C_{ext} will become extremely large and the optical absorption and scattering at this particular frequency would also be exceedingly strong. This is known as a resonance condition. To achieve this, ϵ_r must be close to $-2\epsilon_m$, which is not possible for standard dielectrics and nonmetals that typically have ϵ_r values

between 1 and 50.³⁴ Equation 1.1 also indicates that ϵ_i should be close to zero to support a strong resonance, a condition that can only be satisfied by some of the metals.³⁵ In general, no LSP or PSP sufficiently strong for plasmonic applications can be formed without a negative ϵ_r , and large ϵ_i values mean a lossier or weaker plasmon. The SP strength (or damping) can be described using the quality factor Q :³¹

$$Q = \frac{\omega(d\epsilon_r/d\omega)}{2(\epsilon_i)^2} \quad (1.2)$$

The SP strength is directly proportional to Q ; large values of Q mean strong plasmons (both LSPs and PSPs), and small values indicate a lossy or weak SP with a small C_{ext} . In general, Q should be larger than ~ 10 for most plasmonic applications.

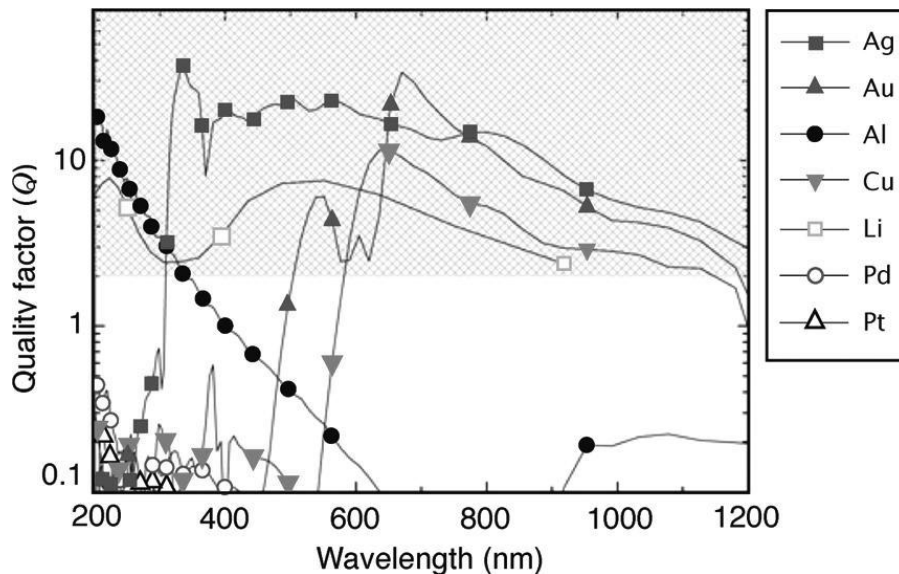


Figure 1.3. Quality factor Q of the LSPR for a metal/air interface. A higher Q denotes less damping and a stronger plasmon resonance. The shaded area represents the region of interest for many plasmonic applications.³⁶

In **Figure 1.3** are plotted the quality factors for some of the most important plasmonic metals. It is easy to see that, Ag has the largest quality factor across most of the spectrum from 300 to 1200 nm. In **Table 1.1**³⁶ (see next page) are reported some of the possible Ag nanostructures (Ag NSs) and their applications that demonstrate the possibility to use Ag in the whole UV-VIS Spectrum.

Moreover, interband transitions, where electrons are excited from the conduction band to higher energy levels, also play an important role in dampening the SP modes.³⁷ Typically, these transitions take place at much higher frequencies than the LSPRs, as in the case of Ag. For Au and Cu, however, these transitions limit their LSPR excitation to wavelengths longer than 500 and 600 nm, respectively.³⁸ In practical applications, the material properties of metals may outweigh their differences in plasmonic properties. On the basis of the quality factor, Li should be a candidate as good as Au and Cu in supporting surface plasmons. However, this metal is so reactive and hard to handle that it is seldom considered and explored for plasmonic applications.

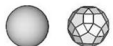












Shape	Illustration	LSPR ^a	Applications ^b	Method of Synthesis	Ref#
Sphere and quasi-sphere		320 - 450	SERS; LSPR sensing; assembly	Polyol process (single-crystal); Citrate reduction (quasi-sphere)	58, 85, 95, 330, 358
Cube and truncated cube		400 - 480	SERS; LSPR sensing; assembly	Polyol process; Seed-mediated growth	53, 80, 96, 200, 214, 371
Tetrahedron and truncated tetrahedron		350 - 450	SERS	Polyol process; Light-mediated Growth	113
Octahedron and truncated octahedron		400 - 500	Assembly	Polyol process; seed-mediated growth; light-mediated growth	105, 334, 346, 364
Bar		350 - 900	SERS	Polyol process	93
Spheroid		350 - 900	SERS	Polyol process	93, 529
Right bipyramid		500 - 700	-	Polyol process	81, 112
Beam		-	Electron transport	Polyol process	73
Decahedron		350 - 450	-	Seed-mediated growth; light-mediated growth; citrate reduction	101
Wire and rod		380 - 460	Wave guiding; electronics; SERS; assembly	Seed-mediated growth	17, 47, 63, 83, 98, 99, 100, 222, 244, 256, 329, 357
Polygonal plates and disc		350 - 1000	SERS; LSPR sensing	Light-mediated growth; polyol process	18, 92, 111, 123, 126, 134, 183
Branched structures		400 - 1100	SERS	Seed-mediated growth	251
Hollow structures		380 - 800	SERS; LSPR sensing	Template-directed growth	131, 137, 146, 192, 262

Table 1.1 Ag nanostructures and their applications

Historically, Ag has been known for its widespread use in photography and staining of biological tissues because of the black color associated with the large aggregates of Ag nanoparticles.³⁹ Silver also has the highest electrical and thermal conductivity among all metals, making it an ideal component for

electrical interconnection. When exposed to air, Ag is reactive with respect to oxygen (oxide formation: few atomic layers), but it is more reactive with respect to H₂S, present in the environment, which forms silver sulfide film on its surface, and should be more or less transparent to the visible light.^{40,41} This thin film of silver sulfide can form in one day and, over a month, can become 60 Å in thickness. It is worth pointing out that the black coating commonly observed on the surface of silverware is due to sulfuration with the sulfur in air,⁴² not to oxidation. As a disadvantage, Ag nanostructures (or more appropriately, Ag⁺ ions coming off the nanostructures) are considered to be toxic, although passivating the surface can greatly increase their stability and thus attenuate or eliminate their toxicity.⁴³ Instability and toxicity are also two major concerns for Cu, especially for the nanoscale structures. In contrast, Au is well-known for its bioinertness, and its surface is believed to be oxide-free. For these reasons, Au nanostructures are well-suited for in vivo applications with humans.⁴⁴ In contrast, Ag nanostructures are largely used in plasmonic applications outside a human body (e.g., plasmonic antennas and circuits for concentrating and guiding light), where they have consistently reported much better performance than Au-based nanostructures.^{45,46} The difficulty of fabricating nanostructures, and their cost, will also determine the usefulness of a metal for plasmonic applications, especially for large-scale applications. The cost varies dramatically across the metals from ~\$1,207 (per ounce) for Pt to ~\$0.049 for Al. Silver is relatively cheap (~\$13.4) among the metals that support plasmons³⁶. Although both Al and Cu are cheaper, they have a limitation in terms of the plasmons they can support, as discussed above. More important is the simplicity with which these metals can be prepared as nanostructures with controllable sizes and shapes.

Over the past decade, Au, Ag, and Pd have all been prepared in a large variety of nanostructures using chemical methods.⁴⁷ Taking into account the unsuitability of Pd for plasmonic applications, Au and Ag are the most promising, and indeed the most widely used, materials in plasmonics. Gold is, however, almost 50 times more expensive than Ag. While the application and scale of production will ultimately decide which metal is the best. Ag compared with the other metals is unique for its excellent qualities in terms of

plasmonic ability, available nanostructures, and material cost. In table 1.1 a list of Ag NSs, their method of synthesis and applications is reported.

1.5 Template Assisted Nanotextured Arrays

Plasmonic nanostructured substrates can be produced by very different synthesis methods, such as seed-mediated growth, nanoscale lithography, thin-film techniques, template assisted growth etc. In order to have more reproducible plasmonic substrates with well ordered arrays, lithographically generated structures and template assisted nanostructures are of course the best method. In a periodic lattice, coupling between neighboring nanostructures, can lead to unique emergent properties that have motivated an understanding of the assembly of these materials.⁴⁸ Such phenomena have already led to applications as diverse as ultrasensitive detection schemes^{49,50,51} that represent one of the principal aim of Plasmonic Scientists. For this reason, and because of its low cost, its simplicity and its accuracy, template assisted nanofabrication method has become one of the most used nanofabbrication techniques.

Template growth synthesis refers to the use of a prefabricated, nanostructured material to influence and/or order the placement of building blocks (typically atomic or molecular species) in specific locations during the growth of the material (**Figure 1.4**)

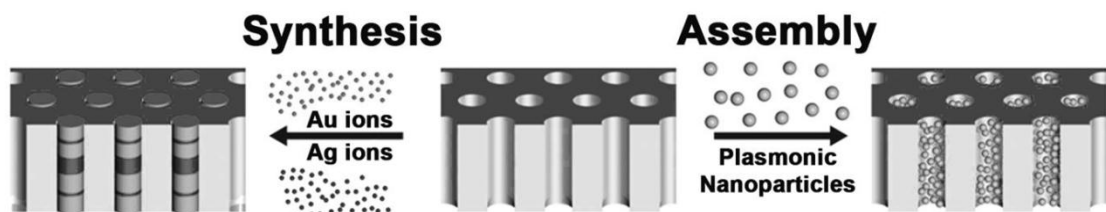


Figure 1.4 Templated synthesis and assembly: Schematic illustration of the distinction between templated synthesis (left) and assembly (right) of plasmonic materials. In the former, nanostructures are synthesized directly on or in the template; in the latter, nanostructures are first synthesized and then placed on or in the template structure. In each case, the size and shape of the final structure are dictated by the geometry of the template.⁵²

This kind of synthesis is especially effective in growing physically restricted (particles with identical geometry and dimensions) metal deposition in order

to have a specific geometry (e.g. growth of a metal in a rod-shaped pore) and in directing growth to a preferential direction. This diversity of strategies, unified by their common use of a guiding template, represents a central theme of nanoscience and nanostructuring of plasmonic substrates formed by anisotropic structures that can be easily controlled. By changing the properties of the template it is possible to tune very well all the parameters of the grown nanostructures, also with more complex shapes, which is usually obtained only by the more expensive and sophisticated lithographic methods. For all these reasons, today, template assisted synthesis has attracted the attention of the scientific community in order to produce plasmonic nanotextured devices for physical, chemical and biological applications.

1.6 Anodic Alumina Oxide Templates

Anodic Alumina Oxide (AAO) Membranes are some of the most known and studied templates in the last 50 years.^{53,54,55} AAO is quite simple to obtain by anodization of ultrapure aluminum (99.998%). AAO are characterized by a well ordered nanoporous array with tunable structure parameters on the whole area covered by the film. **Figure 1.5** shows the morphology of AAO membranes. It is possible to appreciate the regularity of the surface and the hexagonal close-packed array of nanopores that extends on the whole surface. The pores grow perpendicular to the surface and extend down to the bottom of the membrane where they are separated from the substrate by an alumina barrier layer. This non-porous barrier layer, shown in Figure 1.5d, has a hemispherical and scalloped geometry and its thickness is half of the pore wall. It is possible to adjust the pores dimensions by etching the membrane in selected acidic solution. In this way it is possible to widen the pores and to thin the barrier layer, that represents a big drawback for electrochemical applications. One of the most important advantages of the AAO is the tunable porosity and cell size.

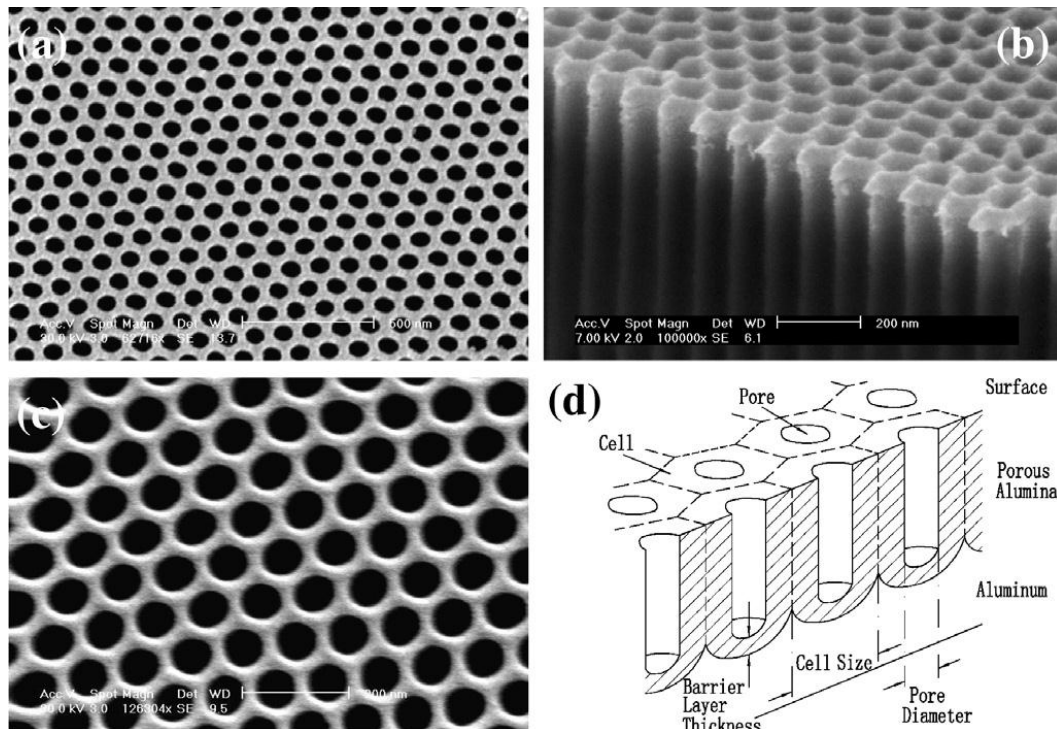


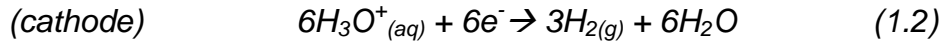
Figure 1.5 AAO: Top view (a) and cross-sectional view (b) of a membrane with pore diameter and cell size of about 65 and 105 nm, respectively. (c) is the top view of a pore-widened membrane with ultra-thin pore walls and (d) is the AAO configuration sketch.

The pores diameter and cell parameters are proportional to the voltage and to the concentration of the acid used in the anodization process and can be adjusted in the range of about 10-200 nm. The three principal acid used to prepare AAO are: sulfuric, oxalic and phosphoric.^{56,57} Anodization in sulfuric acid solution allows to have membranes with a pores diameter of 10-30 nm, in oxalic acid solution allows to have membranes with a pores diameter of 30-80 nm and in phosphoric acid solution membranes with a pores diameter larger than 80 nm. It is very difficult to have a good control of the structural parameters of membranes with pores larger than 100 nm and for this reason it is preferable to work in sulfuric or oxalic acid if a very regular arrangement of the pores is desired. The chemical reactions that occur during the anodizing process in the electrochemical cell, in which the anode is pure Al and the cathode is a plate/rod made of a material chemically inert in the acidic electrolyte (Platinum, Carbon, Stainless Steels, Nickel), are the following:^{58,59,60}

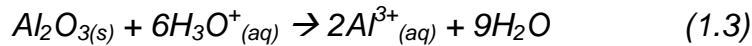
- 1) At the anode, Al^{3+} ions form at the metal/oxide interface and distribute in the oxide layer near the oxide/metal interface. Here they react with H_2O molecules to form Al_2O_3 .



- 2) At the cathode, H_2 forms at the electrolyte/metal interface. The kinetics of this process directly influences the AAO growth rate, that depends strongly on the total charge flowing through the system.



- 3) Simultaneously to the anodic and cathodic reactions, a partial dissolution of Al_2O_3 occurs at the electrolyte/oxide interface. This process is due to electric-field-enhanced oxide dissolution and strongly depends on the pH.



The balance of these three reactions is at the base of the AAO ordered porous structure formation.

The electric-field-enhanced oxide dissolution is clearly the key of this process, because the anodization reaction determines the process of dissolution and reconstruction of aluminum oxide along the direction of the pores formation process.

The formation of the highly-ordered nanopores array can be seen as a self-organization process during the Al anodization, promoted by the repulsive forces between the neighboring pores at the metal/oxide interface.⁶¹

At the beginning of the anodization, pores nucleate at random positions on the Al foil surface. As the pores grow into the aluminum with the anodization process, the pores self-organize and hence the regularity of the pore arrays improves. Normally the regularity of the pores and pore arrangement increases with the anodization time. Therefore, a conventional one-step anodization process with a relatively long anodization period will produce

disordered pores on the top and regular pores at the bottom of the membranes, i.e. alumina membranes with quite different pore regularity on the top and the bottom of the membranes.

A two-step anodization process, that was proposed by Masuda and Satoh,⁶² successfully lead to the fabrication of alumina membranes with regular pores throughout the whole membranes. In this process, after a long first anodization step, the disordered AAO layer is removed from the Al foil by etching in a mixture of chromic and phosphoric acid, leaving a highly ordered concave pattern on the surface of the Al foil. Then, a second anodization is carried out on this surface-patterned Al foil, resulting in alumina membranes with high regular porosity at both sides of the sample.

To improve the pore regularity and the surface smoothness of the anodic alumina membranes, some pretreatments of the Al foils are necessary before the anodization, such as annealing and electropolishing. The annealing process of Al foils under vacuum conditions can remove the mechanical stresses in the Al foils and increases the grain size. This will facilitate the self-organization process of the pores and the following anodization. The electropolishing process (normally using perchloric acid and ethanol solutions) of Al allows to obtain a very smooth Al surface suitable for anodization. This last pretreatment step is fundamental in order to improve the formation of highly ordered arrays. In the literature it is reported that the pore arrangement of anodic porous alumina is usually far from an ideally packed hexagonal columnar array over a sizable region of some millimeters. The defect-free areas of the pore arrays are typically several square micrometers. The size of the defect-free areas increases with the anodization time. However, there is a limitation of this improvement, since so far the reported defect-free area of the self-organized alumina membranes is seldom larger than $10 \mu\text{m}^2$, even with a quite long anodization period. To overcome this limitation in obtaining long-range ordered pores of the self-organized alumina membranes, that limits their applications, in 1997 Masuda et al proposed a “pretexturing” process⁶³. This procedure consists in using a SiC single-crystal to stamp an Al foil in order to give an imprinting to the surface before the anodization process thus allowing to have a large area homogeneity. The very attractive advantages of AAO membranes make it an

excellent template in fabricating ordered arrays of one-dimensional nanostructures like nano-wires and nanotube arrays.

It is clear that by using AAO membranes the size of the grown nanostructures are tunable by simply modifying the properties of the AAO template. This is possible by changing the duration of anodizing process, the applied voltage, the acidic solution and its concentration and finally widening the pores after the anodization process. Another important feature of AAO is the possibility to release the obtained nanostructure just by etching the AAO template using acid or alkali solution. This explains why in the last years a lot of nano-structures were synthesized using AAO templates.

However, because of the difficulty of working directly from the upper side of the membrane, due to the barrier layer at the bottom of the pores, in order to obtain one-dimensional nano-structures, it is preferable to peel-off the membrane from the Al foil and to attach it to the substrate to pattern. Alternatively, it is possible to replicate the membrane through a negative transfer in order to obtain a new semiconductor or metal with the exact structure of AAO.^{53,64}

It is important to remind that it is difficult to fabricate zero-dimensional nano-materials (such as nano-particles and nano-holes) on substrates directly using conventional alumina membranes characterized by a thickness of several μm because it is difficult to have a good adhesion of the membrane on the substrate to pattern. This represents the new goal of AAO template technology.

1.7 Ultra-Thin Alumina Masks

Ultra-thin Alumina Masks (UTAM) are a new special type of AAO with through-holes pores and a thickness less than 1 μm , while commercial and most common AAO membranes have a thickness of several microns to allow their manipulation, otherwise impossible (AAO membranes are very thin and brittle).

UTAMs porous structure is very regular and can be as large as several square centimeters. The pores of UTAMs are short and can be used as masks to deposit, on any smooth surface, highly ordered nano-structures with low aspect ratio or nanoparticles. In this way the pores regularity of UTAMs can be easily transferred to the substrate that will support the nano-structures. Moreover, it is possible to use UTAMs to etch selectively the surface of any kind of substrates in order to obtain a nano-hole array. This “non-lithographic” surface nano-patterning approach provides an efficient and low-cost alternative in fabricating large-scale ordered arrays of surface nanostructures.

The “UTAM nano-patterning” represents a valid and advantageous alternative to the classic and more expensive nano-patterning methods such as EBL, SPM, and self-assembly processes. After the first work of Masuda⁵³, several nano-structures were fabricated by this method and every year hundreds of papers around the world report synthesis that exploit UTAM nano-patterning procedure. One of the reason of this success is the simplicity, the reproducibility and the accuracy of the technique. Using UTAMs to have nano-structure arrays grant a well defined tailoring of the morphological properties. In this direction the engineering of the substrate, in order to reach the desired properties by simply changing the UTAM synthesis parameters, is possible. Furthermore, UTAM nano-patterning can be easily exported to the industrial field. This new nano-patterning approach, compared to conventional lithographic methods, possesses attractive advantages such as large pattern area ($>1 \text{ cm}^2$), high throughput, and low equipment costs. Moreover, the ultra-high density of the ordered nanostructures (10^{10} – 10^{12} cm^{-2}) allows to use these nanostructures in producing high-density data storage media, ultra-thin display devices, high-sensitivity sensors, photonic crystal devices and high-brightness light emitting diodes.⁶⁵

There are two different types of UTAMs exist: attached UTAM and connected UTAM. Attached UTAMs (**Figure 1.6a**) are first fabricated on Al foils, and then they are detached from the foils using a transfer material, like special wax or polymers, and attached to the surface of the chosen substrate. On the

contrary, connected UTAMs (Figure 1.6b) are grown from the Al films that is deposited on the substrate to nano-pattern.

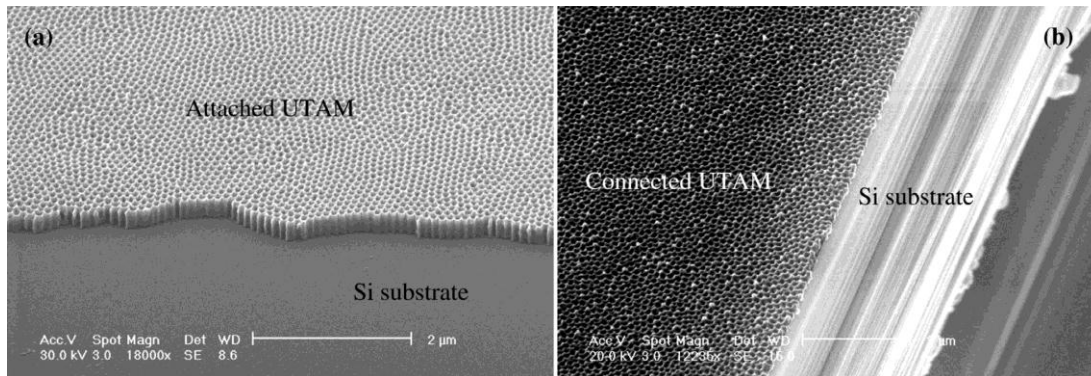


Figure 1.6 An attached UTAM (a) and a connected UTAM (b) on Si substrates. The pore diameter, cell size and thickness of the attached UTAM (a) are about 80, 105, and 350 nm, respectively. The pore diameter, cell size and thickness of the connected UTAM (b) are about 100, 150, and 200 nm, respectively. The connected UTAM is prepared from a 4 μm-thickness evaporated Al layer on Si.⁶⁵

This two different method of UTAM nano-patterning represent both a good choice in order to have well ordered nanopatterned samples on a large area. The “connected” approach represents a good alternative because it is possible to have a high regularity and samples produced in this way can be easily manipulated. Nevertheless, the nanoporous array is usually not highly ordered like the attached one. This is due to the thickness of the Al evaporated on the surface that usually is limited to few microns (less than 10 μm) and as explained before, only with a two-step procedure, that dissolves a lot of Al (about 10 μm per hour), it is possible to obtain a highly ordered UTAM. On the contrary the “attached” approach, that uses UTAM grown on Al foil and then attached on the desired substrate, guarantees to obtain a highly ordered sample and simplifies depositions which require electrochemical methods. In this case the UTAM is front-side attached on the sample and the barrier layer, on the back-side, can be easily removed after ultrapure Al excess elimination by chemical etching. It is clear that depending on the application, it is possible to choose the one or the other approach.

1.8 Electromagnetic Field Enhancement in Ordered Arrays

Periodically ordered metal nanostructures arrays are one of the principal aims of plasmonics scientists because they can generate an electromagnetic field enhancement (EFE) in a broad spectral range and at selected frequencies. Periodicity plays a key role in tuning the optical response and this has been documented in experimental and theoretical investigations of plasmon enhanced effects such as surface-enhanced Raman scattering (SERS),^{66,67,68} extraordinary optical transmission,^{69,70,71} and robust photonic band gaps at visible and NIR wavelengths.^{72,73,74} Especially SERS, because of its potential for single-molecule spectroscopy and chemical sensing with high information content, has attracted a widespread attention. The optimization of ordered substrates for SERS applications with high signal enhancement represents one the most important goal in this field in order to reach lower detection limits.

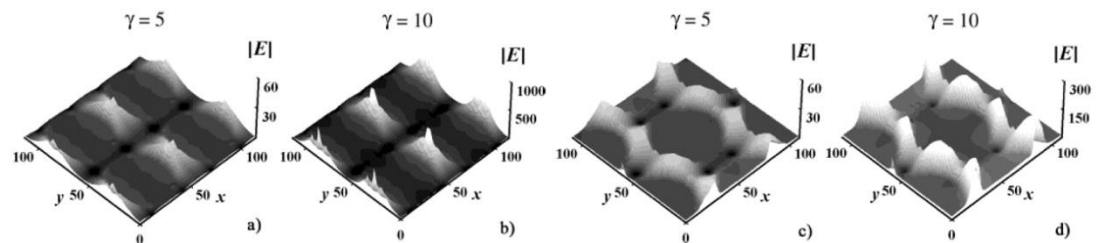


Figure 1.7 Cross-sectional view of local EFE factors produced by p-polarized light ($\lambda = 647$ nm, $E_0 = E_x$) within periodic 2D arrays of Au nanodisks embedded in a low-dielectric medium ($\epsilon_d = 1.5$). Two different lattice geometries are shown: (a, b) 2D square lattice; (c, d) 2D hexagonal lattice. Two different diameterspacing ratios are shown: (a, c) $\gamma = 5$; (b, d) $\gamma = 10$. Note the change in scale for $|E_{loc}(r)/E_0|$ for arrays with different values of γ . Discretization was performed using a 120×120 square lattice.

The highly localized EFE factor $G_{loc} = |E_{loc}(\lambda)/E_0(\lambda)|^4$ at the junction of metal nanostructures (see **Figure 1.7**), that in the case of a two-particle system can be higher than $10^{11} - 10^{12}$, was well studied and described in the literature^{68,75,76,77}. This approach is very useful to understand the physics of these systems, but it is difficult to apply to sensors. In order to engineer and optimize SERS sensors it is better to have an approach that considers the average EFE factors $\bar{G} = \langle G_{loc} \rangle$. Electrodynamics calculation made by García-

Vidal and Pendry⁶⁸ demonstrates that on periodic nanostructured metal \bar{G} values are on the order of 10^6 as are commonly observed in many experimental system.

In his work Genov⁷⁸ have calculated the EFE in two-dimensional arrays of metal nanoparticles embedded in a dielectric medium. The calculations were performed on 2D arrays with square and hexagonal lattices with different structural parameters (Figure 1.7), using simple shapes for the metal structures, to simplify the system, and quasistatic conditions.

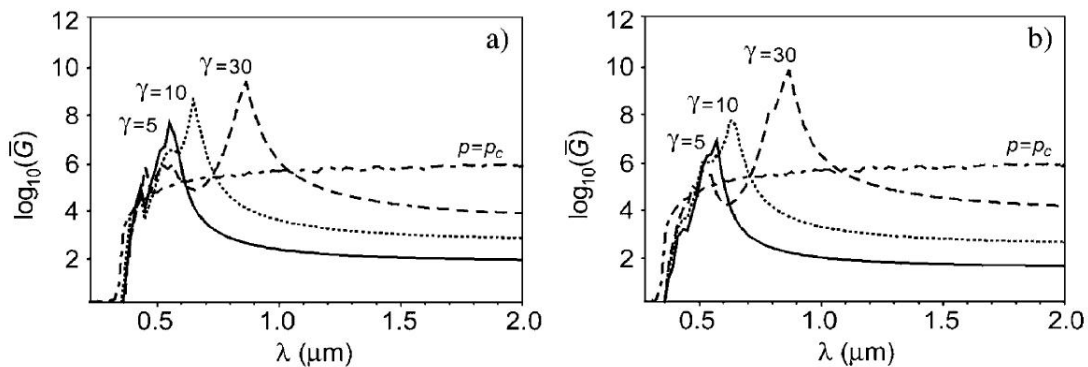


Figure 1.8 Average EFE (\bar{G}) from 2D arrays of Au nanodisks as a function of incident wavelength (λ) at fixed particle diameter-spacing ratios ($\gamma = 5, 10$, and 30): (a) 2D square lattice; (b) 2D hexagonal lattice. A plot of (\bar{G}) from random metal-dielectric films at the percolation threshold ($p = p_c$) is included for comparison.

In a 2D array $E_{loc}(r)/E_0$ can be calculated as a continuous function of the packing density, described by a single geometric parameter $\gamma = d/\bar{\delta}$ (Figure 1.8), where d is the diameter of the nanoparticles and $\bar{\delta}$ is the separation between the nanostructures. To confirm the validity of the numerical calculations, Genov developed an analytical approach to estimate (\bar{G}). The EFE between metal nanoparticles can be thought as an array of RLC circuits across the interparticle gap, with each element i representing a resonance defined by local spacing $\bar{\delta}_i$ (see Figure 1.9).^{79,80}

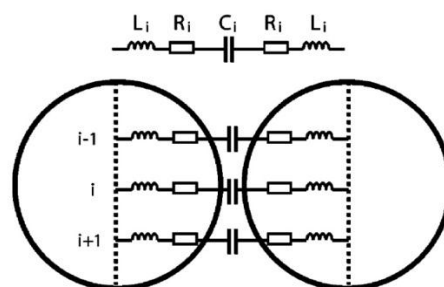


Figure 1.9 Frequency-dependent plasmon response depicted as an array of RLC circuits.

The negative permittivity of the metal ($\epsilon_r < 0$) and the dielectric function of the substrate ϵ_d are represented respectively by inductance R - L and capacitance C . The RLC model suggests that the collective plasmon resonances of the 2D nanoparticle arrays should shift strongly toward lower frequencies (high LC) with increasing γ , in agreement with numerical simulations and recent calculations involving metal nanoparticle dimers.⁸¹ With this work Genov demonstrated that the EFE in ordered array depends dramatically on γ and that numerical simulations and analytical models are in good agreement and yield (\bar{G}) values as high as $2 \cdot 10^{11}$ for arrays of cylindrical Ag nanodisks and $5 \cdot 10^{10}$ for arrays of Au nanodisks. Analytical values can also be obtained for 2D arrays of metal nanospheres, yielding (\bar{G}) values on the order of $2 \cdot 10^9$ and $5 \cdot 10^8$ for Ag and Au nanoparticles, respectively.

1.9 Aim of the thesis

A quick visual inspection of Figure 1.8 clearly shows that a random metal-dielectric films, at the percolation threshold, can in principle present EFE as high as 10^6 on a quite large λ range. This means that a good SERS substrate could in principle be prepared by simply assembling NPs uniformly on a surface and keeping at the same time their dimensions below a critical size. In fact, as written in the previous paragraphs, metal particles present interesting plasmonic properties as long as their dimension is below a critical size ($d < 100\text{nm}$).

A step forward can be achieved if it is possible to obtain ordered arrays of metal nanostructures assembled in such a way that coupling phenomena can occur (see previous paragraph). While the first two issues (size and uniformity) can be achieved in a relatively easy way (metal evaporation, colloidal solution etc.), the latter requires a nanolithography approach or a template methodology. If one wants to use SERS spectroscopy as a routine analytical tool, an easy and cheap approach to prepare the substrates is mandatory. As written above, the first requirement for a good SERS

substrate is the particles dimension and their uniform distribution, while enhancement higher up to 4 or 5 order of magnitude can be obtained only by ordered arrays with particular geometries.

The aim of this thesis is the preparation and the engineering of substrates with an easy&cheap approach for routine laboratory analysis.

In chapter 3 a first attempt to prepare a SERS substrate by electrochemical deposition of Ag NPs on a commercial writable DVD, that is a substrate of controlled morphology and composition, will be shown.

In chapter 4 a relatively easy & cheap way to prepare ordered silver nanostructures (Ag NSs) arrays for SERS and LSPR substrates using AAO templates will be described. It will be shown that it is possible to tune the optical properties of these substrates in order to have a good efficiency in SERS spectroscopy and in LSPR sensing.

Finally, in chapter 5, a very simple way for SERS substrates fabrication by electrophoretic deposition (EPD) of Ag NPs on a $\text{SiO}_2/\text{Si}(100)$ wafer will be reported. For this purpose a “green synthesis”, that uses D-glucose as reducing agent, was developed. This preparation allows to obtain an almost monodisperse colloidal solution of silver nanoparticles (Ag NPs) characterized by a negative z-potential and therefore suitable for EPD.

References

- 1 M. Faraday, *Philos. Trans. R. Soc. London* **1857**, 147, 145
 - 2 M. L. Brongersma, V.M. Shalaev, *Science* **2010**, 328, 440
 - 3 W. L. Barnes, A. Dereux, T. Ebbesen, *Nature* **2003**, 424, 824
 - 4 N. Fang, H. Lee, X. Zhang, *Science* **2005**, 308, 534
 - 5 V. M. Shalaev, *Nat. Photonics* **2007**, 1, 41
 - 6 D. E. Chang, A. S. Sorensen, P. R. Hemmer, M. D. Lukin, *Phys. Rev. Lett.* **2006**, 97, 053002
 - 7 D. E. Chang, A. S. Sorensen, E. A. Demler, M. D. Lukin, *Nat. Phys.* **2007**, 3, 807
 - 8 C. Joachim, J.K. Gimzewski, A. Aviram, *Nature* **2000**, 408, 541
 - 9 D. O'Connor, A. V. Zayats, *Nat. Nanotechnol.* **2010**, 5, 482
 - 10 B. Wiley, Y. Sun, Y. Xia, *Acc. Chem. Res.* **2007**, 40, 1067
 - 11 M. Rang, A. C. Jones, F. Zhou, Z. Y. Li, B. J. Wiley, Y. Xia, M. B. Raschke, *Nano Lett.* **2008**, 8, 3357
 - 12 D. K. Gramotnev, S. I. Bozhevolnyi, *Nat. Photonics* **2010**, 4, 83
 - 13 J. A. Schuller, E. S. Barnard, W. Cai, Y.C. Jun, J. S. White, M. L. Brongersma, *Nat. Mater.* **2010**, 9, 193
 - 14 S. Lal, S. Link, N. J. Halas, *Nat. Photonics* **2007**, 1, 641
 - 15 E. Hutter, J. H. Fendler, *Adv. Mater.* **2004**, 16, 1685
 - 16 A. J. Haes, R. P. VanDuyne, *Anal. Bioanal. Chem.* **2004**, 379, 920
 - 17 D. K. Gramotnev, S. I. Bozhevolnyi, *Nat. Photonics* **2010**, 4, 83
 - 18 J. Takahara, S. Yamagishi, H. Taki, A. Morimoto, T. Kobayashi, *Opt. Lett.* **1997**, 22, 475
 - 19 R. Yan, D. Gargas, P. Yang, *Nat. Photonics* **2009**, 3, 569
 - 20 A. W. Sanders, D. A. Routenberg, B. J. Wiley, Y. Xia, E. R. Dufresne, M. A. Reed, *Nano Lett.* **2006**, 6, 1822
 - 21 C. Girard, E. Dujardin, G. Baffou, R. Quidant, *New J. Phys.* **2008**, 10, 105016
 - 22 Z. Nie, A. Petukhova, E. Kumacheva, *Nat. Nanotechnol.* **2010**, 5, 15
-

-
- 23 V. M. Shalaev, *Science* **2008**, 322, 384
- 24 S. Maier, *Plasmonics: Fundamentals and Applications*, Springer: New York, **2007**
- 25 M. L. Brongersma, V. M. Shalaev, *Science* **2010**, 328, 440
- 26 W. L. Barnes, A. Dereux, T. W. Ebbesen *Nature* **2003**, 424, 824
- 27 F. H. Julien, A. Alexandrou, *Science* **1998**, 282, 1429
- 28 J. A. Stroschio, D. M. Eigler, *Science* **1991**, 254, 1319
- 29 A. I. Yanson, G. R. Bollinger, H. E. Van Den Brom, N. Agrait, J. M. Van Ruitenbeek, *Nature* **1998**, 395, 783
- 30 S. B. Darling, S. D. Bader, *J. Mater. Chem.* **2005**, 15, 4189
- 31 E. L. Ru, P. Etchegoin, *Principles of Surface Enhanced Raman Spectroscopy*, Elsevier: Oxford, U.K., **2009**
- 32 S. Lal, S. Link, N. J. Halas, *Nat. Photonics* **2007**, 1, 641
- 33 S. Link, M. A. El-Sayed, *J. Phys. Chem. B* **1999**, 103, 8410
- 34 K. Kelly, E. Coronado, L. Zhao, G. J. Schatz, *J. Phys. Chem. B* **2003**, 107, 668
- 35 E. J. Zeman, G. C. Schatz, *J. Phys. Chem.* **1987**, 91, 634
- 36 M. Rycenga, C. M. Cobley, J. Zeng, W. Li, C. H. Moran, Q. Zhang, D. Qin and Y. Xia, *Chem. Rev. (Washington, DC, U. S.)* **2011**, 111, 3669
- 37 M. Perner, P. Bost, U. Lemmer, G. Von Plessen, J. Feldmann, U. Becker, M. Mennig, M. Schmitt, H. Schmidt, *Phys. Rev. Lett.* **1997**, 78, 2192
- 38 H. Wang, F. Tam, N. K. Grady, N. J. Halas, *J. Phys. Chem. B* **2005**, 109, 18218
- 39 J. Belloni, *Radiat. Phys. Chem.* **2003**, 67, 291
- 40 J. L. Elechiguerra, L. Larios-Lopez, C. Liu, D. Garcia-Gutierrez, A. Camacho-Bragado, M. Yacaman, *Chem. Mater.* **2005**, 17, 6042
- 41 W. Cao, H. E. Elsayed-Ali, *Mater. Lett.* **2009**, 63, 2263
- 42 H. E. Bennett, R. L. Peck, D. K. Burge, J. M. Bennett, *J. Appl. Phys.* **1969**, 40, 3351
- 43 A. Kunzmann, B. Andersson, T. Thurnherr, H. Krug, A. Scheynius, B. Fadeel, *Biochim. Biophys. Acta, Gen. Subj.* **2010**, DOI: 10.1016/j.bbagen.2010.04.007
-

-
- 44 F. Frederix, J. M. Friedt, K. H. Choi, W. Laureyn, A. Campitelli, D. Mondelaers, G. Maes, G. Borghs, *Anal. Chem.* **2003**, 75, 6894
- 45 L. Rivas, S. Sanchez-Cortes, J. V. Garcia-Ramos, G. Morcillo, *Langmuir* **2000**, 16, 9722
- 46 M. Rycenga, K. K. Hou, C. M. Cobley, A. Schwartz, P. H. C. Camargo, Y. Xia, *Phys. Chem. Chem. Phys.* **2009**, 11, 5903
- 47 Y. Xia, Y. Xiong, B. Lim, S. E. Skrabalak, *Angew. Chem., Int. Ed.* **2009**, 48, 60
- 48 S. K. Ghosh, T. Pal, *Chem. Rev.* **2007**, 107, 4797
- 49 N. L. Rosi, C. A. Mirkin, *Chem. Rev.* **2005**, 105, 1547
- 50 M. E. Stewart, C. R. Anderton, L. B. Thompson, J. Maria, S. K. Gray, J. A. Rogers, R. G. Nuzzo, *Chem. Rev.* **2008**, 108, 494
- 51 J. Homola, *Chem. Rev.* **2008**, 108, 462
- 52 R. Jones Matthew, D. Osberg Kyle, J. Macfarlane Robert, R. Langille Mark and A. Mirkin Chad, *Chem Rev* **2011**, 111, 3736
- 53 H. Masuda, K. Fukuda, *Science* **1995**; 268, 1466
- 54 G. L. Che, B. B. Lakshmi, E. R. Fisher, C. R. Martin, *Nature* **1998**, 393, 346
- 55 K. Nielsch, F. Muller, A. P. Li, U. Gosele, *Adv. Mater.* **2000**; 12, 582
- 56 P. Bocchetta, C. Sunseri, G. Chiavarotti and F. Di Quarto, *Electrochim. Acta* **2003**, 48, 3175
- 57 C. Sunseri, C. Spadaro, S. Piazza, M. Volpe and F. Di Quarto, *J. Solid State Electrochem.* **2006**, 10, 416
- 58 J. C. Scully and Editor, *Treatise on Materials Science and Technology, Vol. 23: Corrosion: Aqueous Processes and Passive Films*, **1983**, 464
- 59 A. Despic and V. P. Parkhutik, *Mod. Aspects Electrochem.* **1989**, 20, 401
- 60 C. R. Martin, *Science* **1994**, 266, 1961
- 61 O. Jessensky, F. Muller and U. Gosele, *Appl. Phys. Lett.* **1998**, 72, 1173
- 62 H. Masuda and M. Satoh, *Jpn. J. Appl. Phys., Part 2* **1996**, 35, L126
- 63 H. Masuda, H. Yamada, M. Satoh, H. Asoh, M. Nakao and T. Tamamura, *Appl. Phys. Lett.* **1997**, 71, 2770
- 64 P. Hoyer, K. Nishio and H. Masuda, *Thin Solid Films* **1996**, 286, 88
-

-
- 65 Y. Lei, W. Cai and G. Wilde, *Prog. Mater. Sci.* **2007**, 52, 465
- 66 A. Wei, B. Kim, B. Sadtler, S. L. Tripp, *Chem. Phys. Chem.* **2001**, 2, 743
- 67 A. Wirgin, T. Lopez-Rios, *Optics Commun.* **1984**, 48, 416
- 68 F. J. Garcia-Vidal, J. B. Pendry, *Phys. Rev. Lett.* **1996**, 77, 1163
- 69 T. W. Ebbesen, H. J. Lezec, H.F. Ghaemi, T. Thio, P. A. Wolff, *Nature* **1998**, 391, 667
- 70 J. A. Porto, F. J. Garcia-Vidal, J.B. Pendry, *Phys. Rev. Lett.* **1999**, 83, 2845
- 71 A. K. Sarychev, V. A. Podolskiy, A. M. Dykhne, V. M. Shalaev, *IEEE J. Quantum Elect.* **2002**, 8, 956
- 72 A. Moroz, *Phys. Rev. Lett.* **1999**, 83, 5274
- 73 W. Y. Zhang, X. Y. Lei, Z. L. Wang, D. G. Zheng, W. Y. Tam, C. T. Chan, P. Sheng, *Phys. Rev. Lett.* **2000**, 84, 2853
- 74 V. A. Podolskiy, A. K. Sarychev, V. M. Shalaev, *Opt. Express.* **2003**, 11, 735
- 75 P. K. Aravind, A. Nitzan, H. Metiu, *Surf. Sci.* **1981**, 110, 189
- 76 N. Liver, A. Nitzan, J. I. Gersten, *Chem. Phys. Lett.* **1984**, 111, 449
- 77 T. Jensen, L. Kelly, A. Lazarides, G. C. Schatz, G. C. J. Cluster Sci. **1999**, 10, 295
- 78 D. A. Genov, A. K. Sarychev, V. M. Shalaev and A. Wei, *Nano Lett.* **2004**, 4, 153
- 79 A. K. Sarychev, V. M. Shalaev, *Phys. Rep.* **2000**, 335, 275
- 80 V. M. Shalaev, *Nonlinear Optics of Random Media: Fractal Composites and Metal-Dielectric Films*, Springer: Heidelberg, **2000**
- 81 H. Xu, J. Aizpurua, M. Kaell, P. Apell, *Phys. Rev. E* **2000**, 62, 4318
-

Chapter 2

Nanomaterials characterization techniques

In this chapter some of the techniques that were used to characterize the samples prepared in this thesis will be briefly described. UV-VIS and FT-IR spectroscopies, that are commonly used spectroscopic techniques were not reported.

2.1 X-Ray Photoelectron Spectroscopy

The X-Ray Photoelectron Spectroscopy¹ (XPS) is based on the photoelectric effect: a surface is exposed to an X ray radiation ($10^{-12} \leq \lambda \leq 10^{-8} m$) that causes the emission of photoelectrons. The basic setup for an XPS experiment is reported in **Figure 2.1a**: there are an X ray source, a sample holder and an electron analyser. All these accessories are mounted into a Ultra High Vacuum (UHV) chamber.

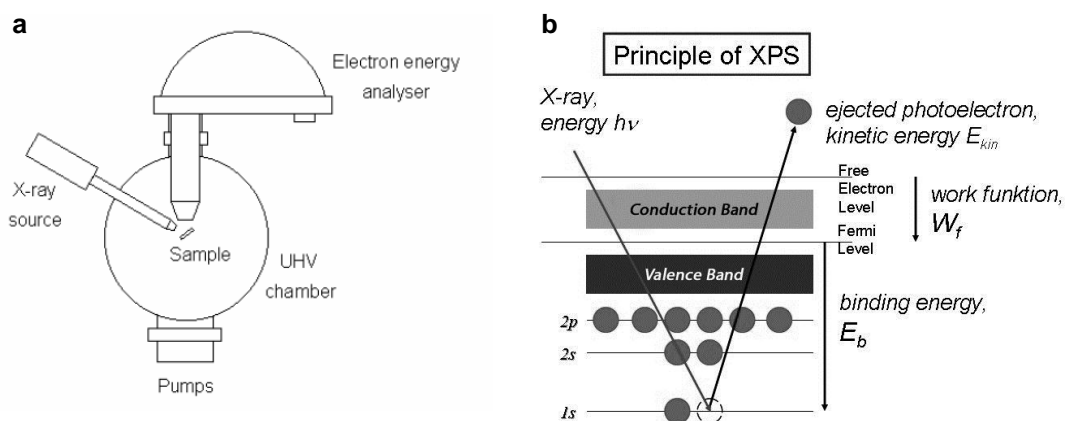


Figure 2.1 (a) Schematic representation of an XPS setup; (b) The photoemission process (in the case of a 1s photoelectron emission)

The X-rays photon flux, generated by the source (usually through electron bombardment of a metal anode, Mg or Al), is directed on the sample and generate a flux of photoelectrons, emitted both from the core and the valence shells (Figure 2.1b). The photoelectrons can either be excited and leave the surface without any energy loss, giving the characteristic elastic peaks, or some of them can undergo inelastic diffusion losing part of their energy as heat and contributing to the spectrum background. The analyzer can discriminate the kinetic energy of the photoelectrons, allowing the acquisition of a spectrum where the signal intensity (counts per second) is reported as function of the kinetic energy. The kinetic energy depends on the photon energy (primary radiation $E = h\nu$) and on the electron binding energy (BE) through the equation:

$$E_k = h\nu - BE - \phi \quad (2.1)$$

where Φ is the sample + analyzer work-function. The BE is strongly influenced by the oxidation state of the analyzed element: it is more difficult to extract a photoelectron from an element in a high oxidation state where the screening effect is low. Therefore, an XPS spectrum can provide important information about the electronic structure of a solid sample, through the analysis of its output core and valence peaks (**Figure 2.2**).

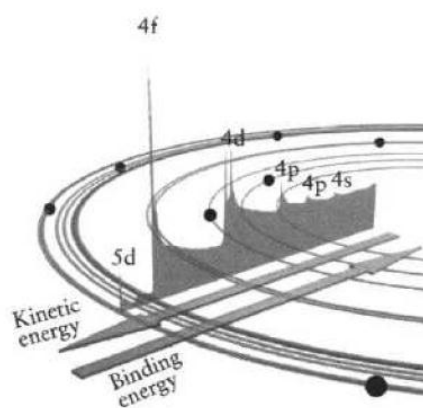


Figure 2.2 Example of an XPS spectrum

Another important parameter in XPS is the sampling depth, that depends on the emitted electrons kinetic energies. In fact, the electrons kinetic energy affects the inelastic attenuation length (Λ_e), that is directly related to the

electron mean free path. Since the variation in the XPS signal intensity is expressed by the following:

$$I = I_0 \cdot \exp\left(\frac{-z}{\Lambda_e \sin\theta}\right) \quad (2.2)$$

where $z/\sin\theta$ is the length through which the electrons are travelling, it is possible to demonstrate that the 95% of the signal comes from a thickness corresponding to $3\Lambda_e$. (where $\theta=90^\circ$) Hence, it is easy to understand why this technique is considered “surface sensitive”, being limited to a sample thickness of few nanometers. As a direct consequence of this, if the angle between the sample surface and the analyzer (θ) is 90° (normal emission with respect to the surface) the sampled thickness is $3\Lambda_e$. When the angle θ is reduced ($\theta < 90^\circ$) then the sampled thickness becomes $3\Lambda_e \sin\theta$, and the analysis results to be more surface sensitive.

The notation used to label the XPS peaks refers to the quantum numbers of the orbital where the photoelectron comes from. It is indicated as nl_j , where n indicates the principal quantum number representing the orbital energy level and l indicates the azimuthal quantum number representing the orbital geometry. When $l \neq 0$ the XPS peaks are doublets because of the spin-orbit coupling. The coupling is represented by the vector j , indicated as a subscript in the notation, whose magnitude is given by $j = l + s$. Therefore a photoelectron emitted from a p orbital can have 2 values of j : $1/2$ (which originates from $l - s$) and $3/2$ (which originates from $l + s$). The peak corresponding to it will be a doublet, whose components will be separated by an energy difference corresponding to the spin-orbit coupling and an intensity ratio given by $(2j + 1)$.

Thus, the p , d and f levels become split upon ionization, leading to vacancies in the $p_{1/2}$, $p_{3/2}$, $d_{3/2}$, $d_{5/2}$, $f_{5/2}$ and $f_{7/2}$. The spin-orbit splitting ratio is 1:2 for p levels, 2:3 for d levels and 3:4 for f levels. The peak areas, after a proper background subtraction depend on the relative probabilities of the various ionization processes.

Because each element has a unique set of binding energies, XPS can be used to identify and determine the concentration of the elements in the surface. Variations in the elemental binding energies (the chemical shifts)

arise from differences in the chemical potential and polarizability of compounds. These chemical shifts can be used to identify the chemical state of the materials being analyzed.

In addition to photoelectrons emitted in the photoelectric process, Auger electrons may be emitted because of relaxation of the excited ions remaining after photoemission. This Auger electron emission occurs roughly 10^{-14} seconds after the photoelectric event. The competing emission of a fluorescent x-ray photon is a minor process in this energy range. In the Auger process, an outer electron falls into the inner orbital vacancy, and a second electron is simultaneously emitted, carrying off the excess energy. The Auger electron possesses kinetic energy equal to the difference between the energy of the initial ion and the doubly charged final ion, and is independent of the mode of the initial ionization. Thus, photoionization normally leads to two emitted electrons - a photoelectron and an Auger electron. The sum of the kinetic energies of the electrons emitted cannot exceed the energy of the ionizing photons.

2.1.1 The Auger parameter

Since the Auger parameter is very often used in the characterization of Ag and AgO the definition and a description of it will be given in the following paragraph.

The Auger parameter concept is based on the following ideas²:

1. There is a fixed difference between two line energies (Auger and photoelectron) of the same element in the same sample.
2. Charge corrections to the individual peak measurements are unnecessary because they simply cancel during the estimation of the Auger parameter.
3. Work function corrections are also unnecessary, and vacuum level data can directly be compared to Fermi level data.

Wagner noted that the difference in two kinetic energies (Auger and photoelectron), which is accurately measurable in the presence of static

charging, can be very useful in the characterization of insulators and semiconductor materials. The position of the Fermi level in these materials is not well defined with respect to the spectrometer Fermi level, making the comparison of absolute core level binding energies doubtful.

The original Auger parameter was defined as the difference in kinetic energies of prominent and conveniently situated Auger and photoelectron peaks from the same elements, recorded in the same spectrum, i.e.

$$\alpha = E_k(C'C''C''') - E_k(C) \quad (2.3)$$

where $E_k(C'C''C''')$ is the kinetic energy of the Auger transition involving electrons from C' , C'' and C''' core levels, and $E_k(C)$ is the kinetic energy of the photoelectron from core level C .

In the original definition, C did not need to be the same as either C' , C'' or C''' , but in fact it often is. Therefore, equation 2.3 could produce negative values of α . Wagner first added 1000 or 2000 eV arbitrarily to the values to make them positive, and then subsequently, following Gaarenstroom and Winograd, redefined the Auger parameter simply adding the photon energy to α , thus defining a “modified” Auger parameter as

$$\alpha' = \alpha + h\nu = E_k(C'C''C''') - E_b(C) \quad (2.4)$$

where $E_b(C)$ is the binding energy of the photoelectron from core level C . We note that nowadays α' denotes the Auger parameter (it is not necessary to add the adjective “modified”) and α denotes the electronic polarizability of a chemical species according to a widely accepted convention.

2.2 Scanning Electron Microscopy

Scanning electron microscope (SEM) images of a sample surface are obtained by scanning it with a high energy electron beam³. Electrons interact with the atoms that compose the sample and produce signals that yield

information about the target surface topography, composition and physical properties such as electrical conductivity. Primary electrons are emitted by thermionic emission from a metallic filament cathode (usually tungsten or lanthanum hexaboride) or by a thermal field emission tip (Schottky emitter) and are accelerated towards an anode. The electron beam, with energy typically from a few hundred eV up to 30 keV, is focused by a system of condenser lenses into a beam with spot dimensions between 0.4 nm to 5 mm. The electron beam passes through pairs of coils or pairs of deflector plates in the electron column which deflect the beam horizontally and vertically so that it scans in a raster fashion over a rectangular area of the sample surface. Both the column and the target chamber are under high vacuum (10^{-6} – 10^{-7} mbar) in order to avoid electron scattering by air molecules. When primary electrons interact with the target, they loss energy by repeated scattering and adsorption events within a teardrop-shape volume (interaction volume), which extends from less than 100 nm up to 1 μ m into the surface. The size of the interaction volume depends on the electron energy, atomic number and density of the target.

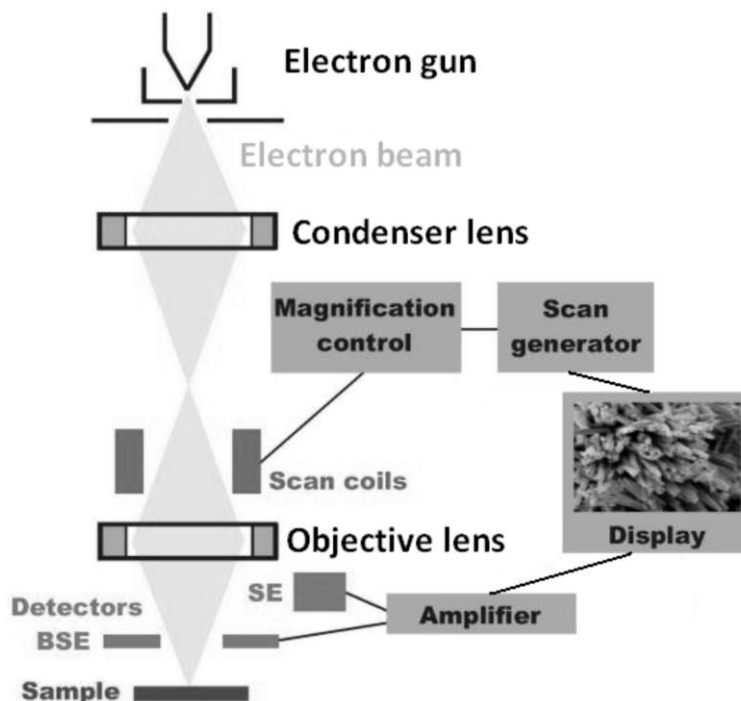


Figure 2.3 Working scheme of the scanning electron microscope (SEM)

The interaction between primary electrons and the sample results in the back-reflection of high-energy electrons by elastic scattering, production of

secondary electrons by inelastic scattering and emission of electromagnetic radiation. The most common imaging technique consists in collecting the low-energy secondary electrons ($E < 50$ eV).

These electrons originate within a few nanometers from the surface and are usually detected by an Everhart-Thornley detector which is a type of scintillator-photomultiplier device. The resulting signal is displayed as a two-dimensional intensity distribution. In **Figure 2.3** the working scheme of a standard SEM is reported. The brightness of the signal depends on the number of secondary electrons reaching the detector: if the beam enters the sample perpendicularly to the surface, the activated region is uniform around the axis of the beam and a certain number of electrons are emitted. As the incidence angle increases, the escape distance of one side of the beam will decrease and more secondary electrons will be emitted. In this way steep surfaces and edges tend to be brighter than flat zones, which results in images with a well defined, three-dimensional appearance. The spatial resolution depends on the size of the electron spot, which is related to the electron energy and the focusing system and it can be also limited by the size of the interaction volume.

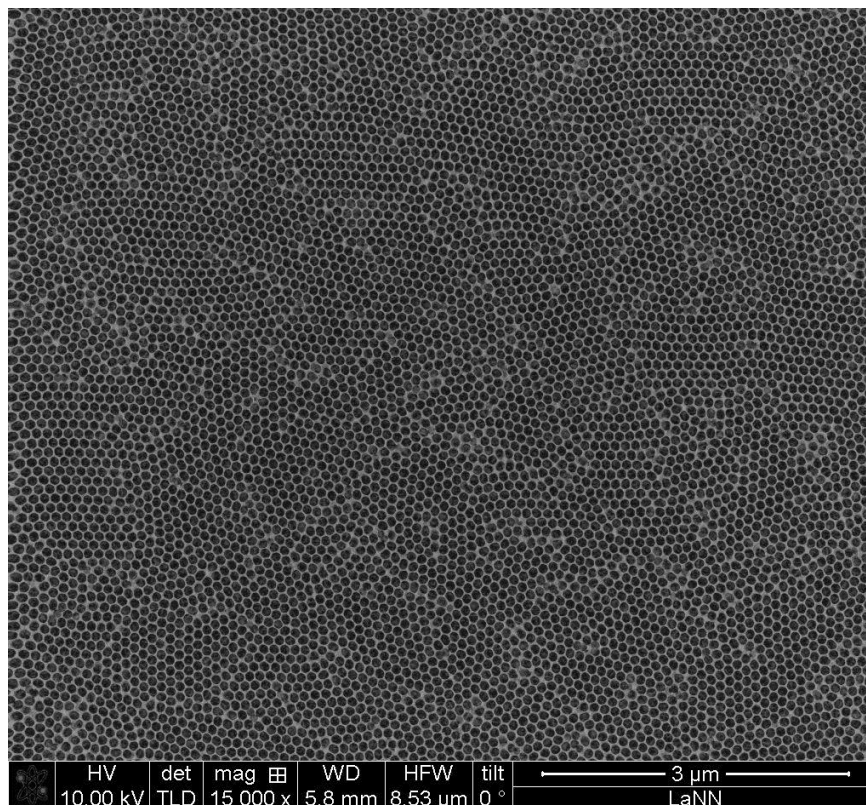


Figure 2.4 SEM image of an Anodic Aluminum Oxide membrane

In our case, resolutions down to few nanometers can be achieved. **Figure 2.4** refer to SEM analysis of an Anodic Aluminum Oxide membrane with the typical honeycomb array and pores of about 75 nm. A considerable homogeneity over μm^2 size is appreciable. Measurements, reported in this thesis, have been performed with the electron column of the dual beam system FEI Nova 600i.

2.3 Transmission Electron Microscopy

Transmission Electron Microscope (TEM) images are obtained by the interaction between an electron beam and the atoms of the sample, that generate a series of signals useful to characterize a material.⁴ We must distinguish between elastic and inelastic scattering. The former is used to construct images (including electron diffraction), while the latter gives rise to the spectroscopic analysis.

From scattered and transmitted electrons, Auger electrons and X-ray, we can obtain information about:

- ✓ morphology and lattice image (bright field BF, dark field DF and high-resolution HRTEM images);
- ✓ crystal structure and symmetry (selected area electron diffraction SAED)
- ✓ composition (Energy Dispersive X-ray Spectroscopy EDS, Electron Energy Loss Spectroscopy EELS).

Generally, a TEM apparatus consists of three basic parts (**Figure 2.5**): the electron source, the objective lens system and the sample-block display with projectors, screens and EELS spectrometers.

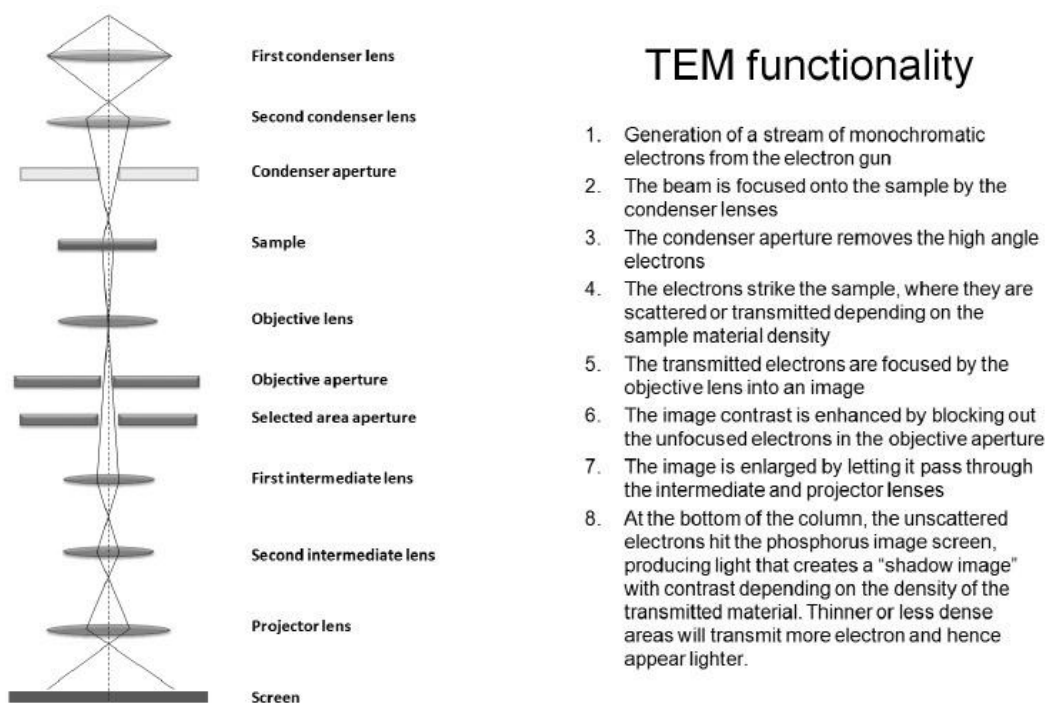


Figure 2.5 Working scheme of a transmission electron microscope (TEM) and a basic description of the workings of a

The source (not reported in the scheme) is an electron gun, based on field emission (FEG), i.e. the electrons are extracted after applying a potential difference on a tungsten filament. This type of source provides a more temporal and spatial coherence of the electron beam. The beam is then homogenized by a condenser placed immediately after the filament. The whole system needs a vacuum that is greater than 10^{-8} Pa for the source, while it is reduced to 10^{-6} Pa along the column (to avoid spread of the beam and contamination of the sample) and 10^{-3} Pa close to the screen that collects the image. The beam is then focused by two condenser lenses which are used to vary the geometry of the beam from parallel to convergent, depending on the type of analysis.

Magnetic lenses are used to focus and deflect the electrons. They consist of toroidal coils with an applied current, generating a magnetic field with a cylindrical symmetry and the axis parallel to the direction of the electron beam. By varying the intensity of current through the toroidal coils, electrons are deflected by the magnetic field. Like all lenses, also the magnetic ones have aberrations that affect the resolution available: spherical aberration, due to non-paraxial ray; chromatic aberration, due to dispersion in the electron

beam energy; astigmatism due to the inhomogeneity of the magnetic field. The objective lens collect the electrons scattered and diffracted by the sample and focus them on the focal plane, where it is possible to collect the diffraction image. Beyond the focal plane, rays are recombined, interfering with each other, to generate the image of the sample on the image plane. The intermediate and projector lenses magnify it on the screen. There is an Energy Dispersive Spectrometer (EDS), directly facing the sample, which analyses the energy of the X-ray produced by the interaction of the electron beam with the sample. Another accessory, that may be present on a TEM, is an Electron Energy Loss Spectrometer with magnetic prism which analyses the energy of the electrons that have passed through the sample.

2.4 Atomic Force Microscopy

Atomic force microscopy (AFM) belongs to the family of the Scanning Probe Microscopy (SPM) techniques.⁵ In SPM, a 3-D scanning of a sample surface is performed, using a special probe which locally interacts with the surface. The probe is placed near the surface ($d < 50$ nm). Depending on the specific type of interaction between the probe and the surface, different kind of microscopies can be performed, such as Atomic Force Microscopy (AFM), and Scanning Kelvin Microscopy (SKM), that are the two techniques used in this thesis. In AFM we measure interatomic force, usually Van der Waals forces, between the atoms on the sample surface and atoms on the tip of the probe made by an elastic cantilever with a sharp tip at the end (**Figure 2.6**). The force applied to the tip by the surface, results in the bending of the cantilever. The cantilever deflection is detected by a laser beam focused on its surface and reflected onto the area of a quad-photodiode. The cantilever deflection causes a displacement of the reflected beam over the four different sections of the quad-photodiode, allowing a precise detection of cantilever movements. The probe (or the sample) is moved on top of the sample (or under the probe) by a piezoelectric transducer (called scanner). Vertical movements are guided by a feedback system which keeps the surface-probe

interaction fixed. These movements are recorded and used to determine the surface height. An electronic system measures the surface-probe interaction at every (x,y) point in the sample. The interaction strength depends on the sample-probe distance. By mapping the strength in the (x,y) points, we can reconstruct an image of the sample surface.

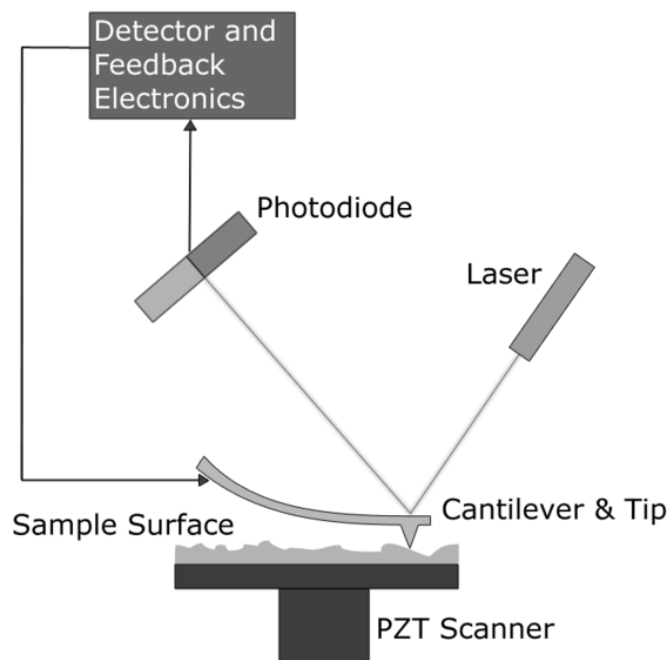


Figure 2.6 AFM scheme of the working system

AFM instruments typically operate in three ways: contact mode (short range forces), non-contact mode (long range forces) and semi-contact (tapping) mode (**Figure 2.7**). In the contact mode, the tip touches the sample surface and the cantilever deflection is caused by the repulsive forces between the tip and the sample. There are two operation modalities for contact mode:

- ✓ constant force, the feedback system drives the piezoelectric actuator to keep the cantilever bending fixed;
- ✓ constant height, the tip height is kept constant and the different force strengths between tip and surface are recorded.

In non-contact mode, the cantilever, vibrating with a small amplitude, experiences the influence of a non-uniform force field near the sample surface. This interaction modifies the resonance frequency of the cantilever and physical information about the surface is obtained from these variations.

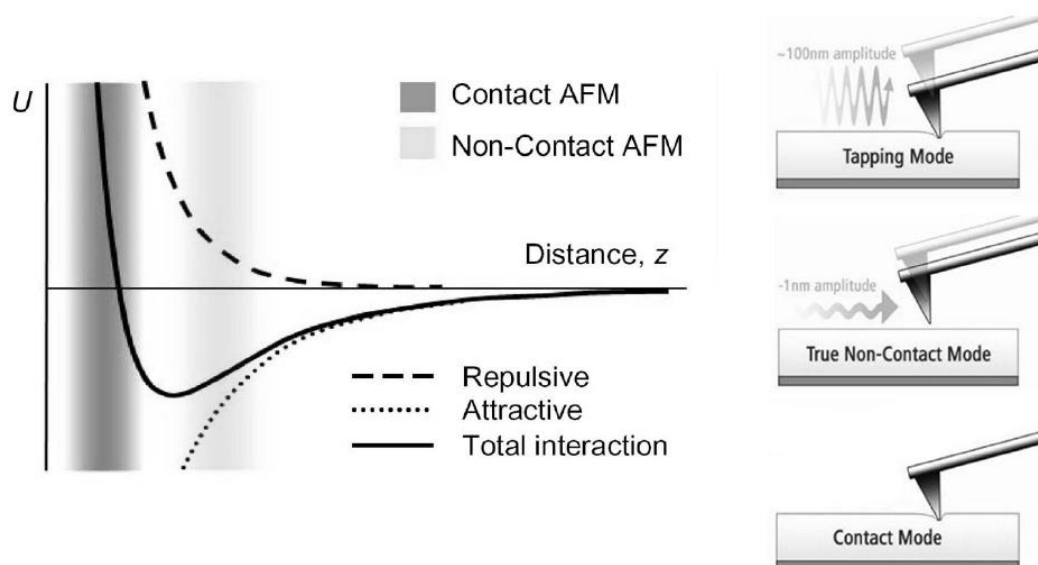


Figure 2.7 The interaction between the tip and the sample depends on the separation distance, and is utilized differently for contact- and non-contact AFM

This mode of operation is less detrimental to the sample but has worse lateral resolution. In the semi-contact or tapping-mode, the cantilever oscillates at its resonance frequency, like in non-contact mode, but the tip touches the surface in an intermittent way. The tip moves in a field of both attraction and repulsion forces. Away from the surface the lever makes free oscillations, while, when there is an interaction with the surface, the oscillations amplitude is reduced until a set value (set-point) is reached. In this case, the piezoelectric actuator moves the cantilever in order to keep the oscillation amplitude fixed, reflecting the differences in the surface morphology. The surface morphology can be reproduced through the actuator movements. The advantages of this procedure are low sample damaging and good lateral resolution.

2.5 Surface Enhancement Raman Spectroscopy

Molecular vibrations and therefore molecular structure can be probed by the Raman scattering process.⁶ Raman spectroscopy, because of its ability to provide molecule fingerprints, allows a unique approach for solving analytical

problems. However, Raman scattering has an extremely small cross section, typically 10^{-30} to 10^{-25} cm^2 per molecule, with the larger values occurring only under favorable resonance Raman conditions. The small Raman cross sections require a large number of analyte molecules to achieve adequate conversion rates from excitation laser photons to Raman photons. Therefore, usually, Raman spectroscopy has been considered a technique for structural analysis, rather than a method for ultrasensitive trace detection or even as tool at the level of single molecules. However, Raman scattering literally appears in a new light when it takes place in the local electro-magnetic fields of metal nanostructures. The favorable optical properties of these metal nanostructures, based on their surface plasmon polaritons, provide the key effect for the observation of enhanced Raman signals from molecules adsorbed on their surface. This effect is called *surface-enhanced Raman scattering* (SERS). Large enhancement factors up to 14 orders of magnitude transform Raman spectroscopy from a structural analytical tool to a structurally sensitive single-molecule and nanoscale probe. At present, SERS is the only way to detect a single molecule and simultaneously probe its chemical structure.

2.5.1 Technique and fundamental relations of SERS

It is generally agreed that two effects contribute to the observed total enhancement: the “electromagnetic” field and the “chemical first layer” contribution.⁷

Figure 2.8 presents a schematic of normal and surface enhanced Raman scattering. In normal Raman scattering, the total Stokes Raman signal I_{NRS} is given by:

$$I_{NRS}(\nu_S) = NI(\nu_L)\sigma_{free}^R \quad (2.5)$$

where σ_{free}^R is the Raman cross section of free molecules, $I(\nu_L)$ is the excitation laser intensity and N the number of molecules in the probed

volume (Figure 2.8a). Because of the extremely small Raman cross sections, at least 10^8 molecules are necessary to generate a measurable Raman scattering signal. In a SERS experiment (Figure 2.8b), the molecules are adsorbed on a metallic nanostructure (single nanoparticles, nanorods, aggregates, nanoshells, etc).

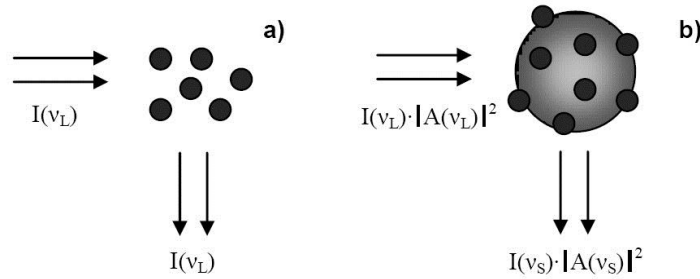


Figure 2.8 Comparison of a) normal and b) surface enhanced Raman scattering

The surface enhanced Stokes Raman signal I_{SERS} is given by:

$$I_{SERS}(v_S) = N' I(v_L) |A(v_L)|^2 |A(v_S)|^2 \sigma_{ads}^R \quad (2.6)$$

and it is proportional to the Raman cross section of the adsorbed molecule σ_{ads}^R , the excitation laser intensity $I(v_L)$, and the number of molecules which are involved in the SERS process N' . $|A(v_L)|^2$ and $|A(v_S)|^2$ represent the field enhancement factors of the laser and Stokes fields, respectively.

The “Chemical first-layer” effects include enhancement mechanisms of the Raman signal, which are related to specific interactions, i.e., electronic coupling between the molecule and metal, resulting in an “electronic” enhancement.⁸ Chemical SERS enhancement is expressed as an increased Raman cross section of the adsorbed molecule compared to the cross section in a normal Raman experiment. Possible electronic SERS mechanisms involve a resonance Raman effect due to a metal molecule charge-transfer electronic transition or a dynamic charge transfer between the metal and molecule, which can be described by the following steps:

- ✓ photon annihilation, excitation of an electron into a hot electron state,
- ✓ transfer of the hot electron into the LUMO of the molecule,
- ✓ transfer of the hot electron from the LUMO back to the metal,

✓ return of the electron to its initial state and Stokes photon creation.

The magnitude of chemical enhancement factor has been estimated to be not higher than 10 - 100. The electromagnetic or field enhancement factors ($|A(\nu_L)|^2$ and $|A(\nu_S)|^2$) arise from enhanced local optical fields, near the metal surface, due to excitation of surface plasmon resonances. In fact, the light from the laser beam excites the surface plasmons that radiate a dipolar field. The coherent interaction of the incoming electric field with the dipolar field leads to a redistribution of the electric field intensities near the nanostructure surface and a molecule adsorbed on the metal feels an enhanced excitation. In the same way, the Raman scattered field is enhanced. SERS enhancement is particularly strong when both laser and scattered field are in resonance with the surface plasmons and this is quite common because the width of the surface resonance is larger than the frequency shift between the laser and the scattered lights. Therefore, the laser and Raman scattered fields increase by about the same amount and the signal power scales with the fourth power of the local optical field enhancement.⁹ The enhancement depends on the type of metal and on the nanostructures. Electromagnetic field enhancement has been calculated for isolated single colloidal silver and gold spheroids and for coupled nanoparticles.¹⁰ Closely spaced interacting particles seem to provide extra field enhancement, particularly near the gap sites between two particles in proximity, resulting in electromagnetic SERS enhancement factors up to 10^8 . Theory also predicts strong enhancement of electromagnetic fields for sharp features and large curvature regions¹¹ and on nanoshells structures.^{12,13}

2.5.2 Experimental set up for SERS

The Surface Enhanced Raman Spectroscopy¹⁴ (SERS) measurements were performed with a homemade micro-Raman instrument where an optical microscope (Olimpus BX 40) equipped with three objectives, 20X/0.35, 50X/0.75 and 100X/0.90, was coupled to the spectrograph and used to record the Raman spectra in micro configuration.

The instrument uses low-power laser sources and a computer management tool. Laser sources available are a single line Argon ion laser (Spectra Physics Stabilite 2017) operating at 514.5 nm and 488 nm with output power of 100 mW, a Helium-Neon laser (Melles Griot) at 632.8 nm with output power 35 mW and a diode laser (XTRA) at 785 nm with output power of 500 mW. The key characteristics of this system are: high stability and optical efficiency (> 30%), possibility of continuous scanning for extended spectral ranges, high spatial resolution and a completely integrated software with Windows XP. In **Figure 2.9**, a schematic image of a micro-Raman is shown. The laser beam covers a path defined by mirrors driven by stepper motors whose position has been stored for each laser line used. The laser beam is attenuated through a series of filters with different optical density, interchangeable via software. After the input mirrors, Beam Expander lenses are mounted to expand the nearly point source into a parallel beam of about 6mm in diameter (equal to the back microscope aperture). By varying the distance of the two components of the Beam Expander, the spot size changes and it is possible to control the focus position of the microscope.

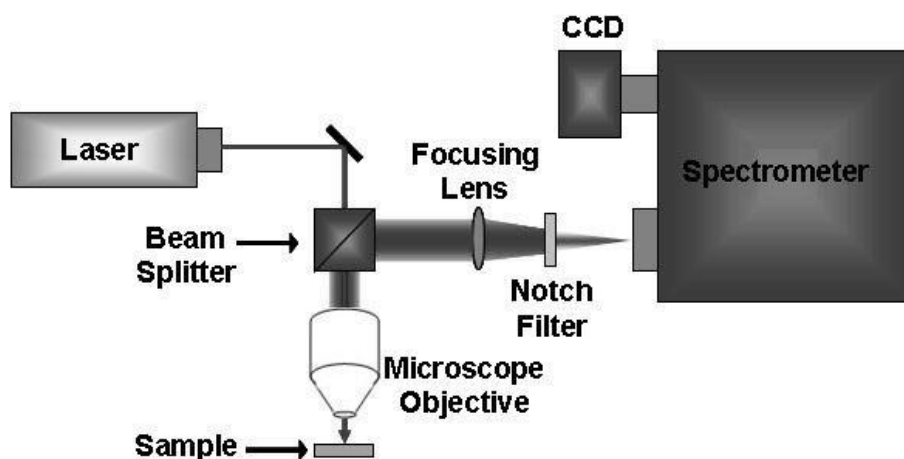


Figure 2.9 Schematic of a micro-Raman spectrometer where illumination and collection are performed through microscope objective.

The radiation scattered and collected by the objective of the microscope, is filtered by a notch or edge filter (depending on the wavelength), and finally collected into an imaging spectrograph (TRIAx-320 ISA) equipped with a Charge-Coupled Device (CCD). The detector is made of a liquid nitrogen

cooled CCD camera (Spectrum One, Jobin Yvon). Each pixel consists of a silicon diode that generates a current when hit by electromagnetic radiation. Columns of pixels are the channels within which electrons, in a given range of energy, are collected. The sensor can analyze a range of wavelengths, or alternatively should be centered around a given value of Raman shift.

2.6 Diffuse Reflectance Spectroscopy

The measurement of diffused radiation reflected from a surface is usually known as diffuse reflectance spectroscopy. Diffuse reflectance spectroscopy (DRS) concerns one of the two components of reflected radiation from an irradiated sample, namely specular reflected radiation, R_s and diffusely reflected radiation, R_d . The former component is due to the reflection at the surface of single crystallites while the latter arises from the radiation penetrating into the interior of the solid and re-emerging to the surface after being scattered several times. These spectra can exhibit both absorbance and reflectance features due to contributions from transmission, internal and specular reflectance components as well as scattering phenomena in the collected radiation. Based on the optical properties of the sample, several models have been proposed to describe the diffuse reflectance phenomena. Diffuse Reflectance Spectroscopy (DRS) measurements were performed with a standard integrating sphere (see **Figure 2.10**).

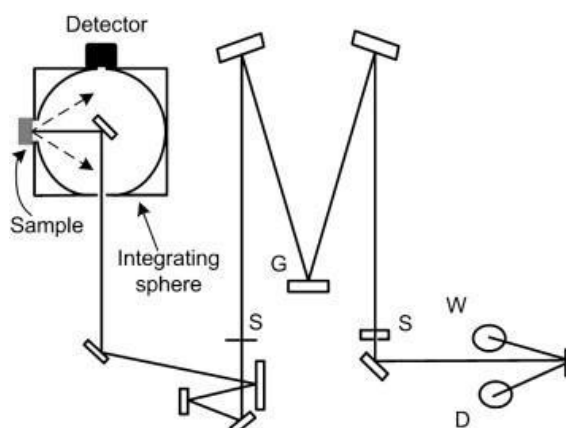


Figure 10 Schematic of a standard DRS instrumentation with integrating sphere

DRS measurements are fundamental in order to perform an optical characterization of powders and opaque samples. The model developed by Kubelka-Munk in 1931 is widely used and accepted in diffuse reflectance IR and UV-VIS spectrometry. The intensity of the reflected light depends on the scattering coefficient s and the absorption coefficient k . The reflectance data can be converted to absorbance by Kubelka-Munk equation^{15,16}:

$$\log \left[\frac{(1-r)^2}{2r} \right] = \log k - \log s \quad r = \frac{R_{(sample)}}{R_{(standard)}} \quad (2.7)$$

The standard used in DRS measurements is a BaSO₄. $R_{(standard)}$ is taken as unity. $R_{(sample)}$ is the diffuse reflectance of the sample and

$$R = \frac{I_{sample}}{I_{reference}} = \frac{(1-R)^2}{2R} = \frac{k}{s} \quad (2.8)$$

From DRS measurements the band gap can be estimated from the plot of $((k/s)hv)^2$ vs hv , that represents the photon energy, by extrapolating the graph to the x-axis.

References

- 1 C. S. Fadley, *Basic Concepts of X-Ray photoelectron Spectroscopy, in Electron Spectroscopy, Theory, Techniques and Applications*, Ed C. R. Brundle, A. D. Baker, Pergamon Press, **1978**
 - 2 G. Moretti, *J. Electron Spectrosc. Relat. Phenom.* **1998**, 95, 95
 - 3 N. Yao, Z. L. Wang, *Handbook of Microscopy for Nanotechnology*, Springer, **2005**
 - 4 L. C. Feldmann, J. W. Mayer, *Fundamentals of Surface and Thin Films Analysis*, New York: North Holland-Elsevier, **1986**
 - 5 R. Howland, L. Benatar, *A practical guide to scanning probe microscopy*; **2000**
 - 6 K. Kneipp, H. Kneipp, J. Kneipp, *Acc. Chem. Res.* **2006**, 39, 443
 - 7 K. Kneipp, H. Kneipp, I. Itzkan, R. Dasari, M.S. Feld, *Chem. Rev.* **1999**, 99, 2957
 - 8 K. Kneipp, H. Kneipp, R. Manoharan, I. Itzkan, R. R. Dasari, M. S. Feld, *Bioimaging* **1998**, 6, 104
 - 9 K. Kneipp, *Physics Today* **2007**, 40
 - 10 F. J. Javier Garcìa de Abajo, *Phys. Chem. C* **2008**, 112, 17983
 - 11 K. L. Kelly, E. Coronado, L. L. Zhao, G. C. Schatz, *J. Phys. Chem. B* **2003**, 107, 668
 - 12 K. Tanabe, *J. Phys. Chem. C* **2008**, 112, 15721
 - 13 J. B. Jackson, N. J. Halas, *PNAS* **2004**, 101, 17930
 - 14 D. A. Skoog, F. J. Holler, S. R. Crouch, *Principles of Instrumental Analysis 6th Ed*, Brooks Cole, **2006**
 - 15 P. Kubelka, *J. Opt. Soc. Am.* **1948**, 38, 448
 - 16 P. Kubelka, F. Munk, *Zh. Tekh. Fiz* **1931**, 12, 593
-

Chapter 3

Silver nanoparticle arrays on a DVD derived template: an easy&cheap SERS substrate*

3.1 Introduction

In this chapter a first attempt to obtain easy&cheap substrates for surface-enhanced Raman scattering (SERS) will be described. SERS is a powerful analysis technique, but for its widespread use it needs a large scalability that can be reached using only simple fabrication method and cheap processes and instruments. As it is well-known, since the first report by Fleischmann and co-workers in 1974 on SERS effect,¹ many efforts have been devoted to put on a firm basis both the underlying theoretical aspects and the application procedures, as demonstrated by the impressive publication rate up to ~1000 papers/year.² Such a great interest is motivated by the many potential applications in analytical chemistry areas, such as forensics, environmental monitoring, biomedical diagnostics,³ and single-molecule detection.

From the physico-chemical basic point of view, the emerging picture is that nanoscale features on a metallic surface can support strong near fields that are significantly enhanced with respect to the incident field illuminating the surface. Such enhanced field is often mediated by the surface plasmon resonance (SPR)⁴ of the substrate and is responsible for the huge Raman signals (quantified by an enhancement factor, EF⁵) observed from molecules (analyte) located within the enhanced near field. In particular, the region

* G. Giallongo, R. Pilot, C. Durante, G. A. Rizzi, R. Signorini, R. Bozio, A. Gennaro and G. Granozzi, *Plasmonics* **2011**, 6, 725

between nanoparticle (NP) pairs has been associated to “hot spots”, i.e. areas of intense electromagnetic fields that give rise to remarkable EF values.⁶ Besides such electromagnetic interpretation of the SERS effect, also a chemical mechanism has been proposed to concur to the experimental scenery.³ Thence, much attention has been often focused on obtaining the largest values of EF to enter the field of single-molecule detection.

However, in order to make feasible the application of SERS as a detection technique in a real sensor, some important issues associated to the preparation of reproducible substrates must be tackled. While substrates with random nanostructured surfaces have been largely explored, there is still large irreproducibility associated with such systems since minor changes in surface morphology can lead to dramatic changes in enhancement. Thus, in recent years, many techniques have been developed to fabricate SERS substrates that present purposely designed periodic nanostructures at the surface: their performances have been recently reviewed and the important concept of finding a compromise between reproducibility and enhancement has been clearly pointed out.⁷ SERS-optimized nanostructured surfaces have been tailored by a wide variety of techniques, including nanosphere lithography⁸, on-wire lithography,⁹ e-beam lithography,¹⁰ and nanoimprint lithography.¹¹ However, the explored methods often requires specialist expertise and/or expensive tools, so searching for easy and cheap SERS substrates represents an important goal. Among the metals, Ag is generally preferred over Au as SERS active element because of its up to 2 orders of magnitude larger EF in the visible spectral region. Ag is, however, prone to oxidation, and the stability of the Ag-based SERS substrates is still an open issue,¹² so that disposable cheap Ag-based SERS substrates might represent a viable answer to such a question.

In the present part of the thesis the structure and the SERS performance of ensembles of Ag NPs electrochemically deposited on inexpensive grating substrates obtained from commercially available Digital Versatile Disc (DVD) will be discussed. Compact Disc (CD) derived surfaces have been already proposed as effective electrodes (named CDtrodes) for electroanalytical chemistry and as biomedical sensors,¹³ while recently DVD derived

corrugated templates have been used to grow self-organized colloidal crystals.¹⁴ In addition, after an easily obtainable modification of the DVD grating shape, they have been recently used as a device for plasmonic applications.¹⁵

The present study represents the first example of application of DVD derived templates to prepare cheap and reproducible disposable SERS substrates. The performances of such substrates will be compared with the literature ones adopting the criteria discussed above, i.e. ease and cost of preparation, ease of use, spot-to-spot reproducibility, substrate-to-substrate repeatability and EF value⁷

3.2 Experimental Section

3.2.1 Substrates preparation

The SERS substrates are obtained by electrochemically depositing a silver NPs array on a corrugated electrode obtained from commercial recordable DVDs (AgNPs@AgDVD). DVDs are composed by two polycarbonate plates having a spiral distribution of rectangular-shaped grooves which complementarily match to form a sandwich where a photosensitive dye is included. One of the two plates is coated by a mirror-like Ag film, which is thus an effectively corrugated Ag-based template that can be used as an electrode to electrodeposit Ag NPs. Hereafter the notations AgDVD for the silver surface of the commercial DVD and AgNPs@AgDVD for a sample where Ag NPs have been deposited on AgDVD will be adopted. The cathode electrodes were obtained by cutting a DVD in square shaped pieces by means of a glass disk saw. This procedure prevents to damage the AgDVD surface and facilitates the process of mechanical separation of the two plates forming the DVD. The sample electrodes were washed with ethanol to remove the photosensible dye and rinsed with bidistilled water. The electrodeposition of Ag NPs on the AgDVD electrode was performed

galvanostatically in a Pyrex cell of 100 mL volume containing 20 mL of an aqueous solution of KNO_3 0.1 M and AgNO_3 0.01 M. A PAR 273A potentiostat/galvanostat was employed for the galvanostatic deposition. The AgDVD electrode was dipped in the solution exposing an active area of $\approx 1 \text{ cm}^2$ whereas the electrical contact was assured by means of flat nose pliers out of the solution surface. The electrodeposition was carried out by applying a constant current of 1 mA for 60 seconds without stirring the solution and by employing an Ag wire as counter electrode. During electrodeposition, the potential/time behaviour was registered by computer control.

Before recording Surface Enhanced Raman Scattering (SERS) measurements, AgDVD and AgNPs@AgDVD were functionalized by immersion for 1 hour in a 10 mM methanol solution of benzenethiol (BT). All samples were rinsed with a copious amount of methanol and dried with nitrogen before performing the measurement. BT (purum, 98% GC) was purchased from Fluka.

3.2.2 Morphological and chemical characterization

SEM measurements were carried out by a Zeiss SUPRA 40VP field-emission instrument, using primary beam voltages of 10–20 kV. AFM characterization of the surface morphology was realized with a Park Scientific Instrument-Model CP by using silicon cantilever tips with nominal curvature radius of 10 nm in contact mode.

The chemical characterization of the sample surface was obtained by XPS, using a VG ESCALAB MK II (Vacuum generators, Hastings, England) system (base pressure of 1×10^{-7} Pa) equipped with a twin anode (Mg/Al) X-ray source with hemispherical electrostatic analyzer and a five channeltrons detector. All the spectra reported were collected using Al K_α excitation energy. The peak intensities were determined after a linear background subtraction. The binding energy (BE) scale was calibrated with respect to Ag $3d_{5/2}$ (368.0 eV) measured on an Ar-sputtered AgDVD sample.

3.2.3 Optical measurements

Diffuse reflectance measurements were recorded on a Jasco V-570 spectrophotometer equipped with a Jasco ISN-470 integrating-sphere apparatus. The studied wavelength range was 200-800 nm.

SERS measurements were recorded by using a micro-Raman setup. A single line Argon ion laser (Spectra Physics Stabilite 2017) operated at 514.5 nm and 488 nm and a Helium-Neon laser (Melles Griot) at 632.8 nm were used as excitation light sources. The laser beam was coupled into a microscope (Olympus BX 40) and focused on the sample by a 20x objective (Olympus SLMPL, NA=0.35). Back-scattered Raman signal was separated from the Rayleigh scattering by a holographic Notch Filter (Kaiser Optical Systems) and analyzed with a 320 mm focal length imaging spectrograph (TRIAx-320 ISA) and a liquid nitrogen cooled CCD camera (Spectrum One, Jobin Yvon). A polarization scrambler was placed in front of the entrance slit of the spectrograph. Typical spot diameter at the focus was about 3 μm .

SERS enhancement factors (EFs) were evaluated following the procedure outlined by Le Ru,⁵ adopting the following expression

$$EF = \frac{I^{BT}}{I^{Tol}} \frac{C_V^{Tol}}{C_S^{BT}} \frac{\sigma_{Tol}}{\sigma_{BT}} \frac{H_{eff}}{A} \quad (3.1)$$

where I^{BT} is the area of the 999 cm^{-1} band of BT (β_{CCC}) absorbed on the metal surface, I^{Tol} the area of the nearby 1002 cm^{-1} band of liquid toluene (β_{CCC}).^{16,17} In parenthesis it is shown the band assignment: β indicates the in-plane bending and consequently β_{CCC} corresponds to the so called *benzene ring breathing mode*. C_S^{BT} is the surface packing density of BT on a flat silver surface, C_V^{Tol} the number of molecules per unit volume of toluene, σ ($\sigma_{Tol}, \sigma_{BT}$) is the Raman differential cross section and H_{eff} is the axial collection efficiency of the experimental set-up. The reference (I^{Tol}) was measured

putting a drop of toluene in between a concavity slide and a cover slip 150 μm thick. BT was used as a reference instead of toluene because it is easier to handle. The ratio $\frac{\sigma_{\text{Tol}}}{\sigma_{\text{BT}}}$ was experimentally estimated at 632.8 nm excitation for the 999 cm^{-1} band of BT and the 1002 cm^{-1} band of toluene, with the following expression: ¹⁸

$$\frac{\sigma_{\text{Tol}}}{\sigma_{\text{BT}}} = \frac{C_{\text{V}}^{\text{BT}} I^{\text{Tol}}}{C_{\text{V}}^{\text{Tol}} I^{\text{BT}}} \quad (3.2)$$

C_{V}^{BT} is the number of molecules per unit volume of BT. The ratio was found to be 0.56. The same value was used for the evaluation of the EFs at the other two excitation wavelengths. H_{eff} was measured by the procedure in Ref. 5 and turned out to be around 50 μm . The remaining parameters in equation (3.1) can be retrieved from the literature: $C_{\text{S}}^{\text{BT}} = 6.8 * 10^{14}$ molecules cm^{-2} ,¹⁹ (this value represents the highest packing density in the literature and therefore provides a conservative estimation of the EF) and $C_{\text{V}}^{\text{Tol}} = 5.7 * 10^{21}$ molecules cm^{-3} .

The parameter A corresponds to the ratio between the number of molecules illuminated on the sample and on a flat surface within the same laser spot, assuming equal packing densities on both surfaces. Its value depends on the sample morphology and will be evaluated in the next section.

3.3 Results and discussion

3.3.1 Preparation and characterization of the substrate

An XPS survey scan (not reported) obtained from the freshly cleaned (ethanol, water, ethanol; see experimental section) AgDVD support shows

only the presence of Ag signal and a moderate contamination from carbon. Such a substrate has been directly used for the electrochemical preparation of the AgNPs@AgDVD sample according to the very easy galvanostatic procedure described in the experimental section.

In the present thesis it was decided to avoid additives in the electrodeposition process for three main reasons:

- reducing any unnecessary chemical burden;
- preventing any inclusion of additives in the Ag NPs;
- reducing any surface roughness smoothing which could lower the SERS EF value.

Actually, there are experimental evidences suggesting that polar additives tend to form complexes with the metal cations leading to surface smoothing.²⁰

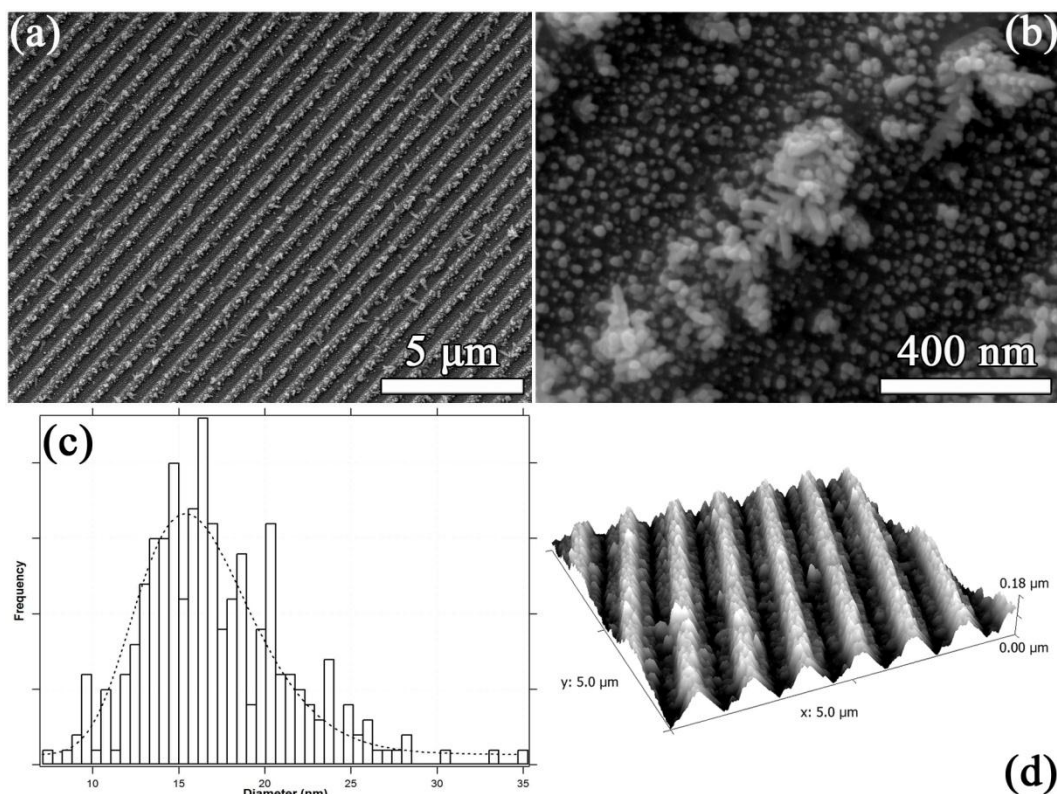


Figure 3.1 Large scale (a) and close-up (b) SEM images from AgNPs@AgDVD sample. (c) Ag NPs diameter distribution within the grooves. (d) AFM image from AgNPs@AgDVD

Likewise any other deposition process, nucleation is a prerequisite for the electrochemical deposition of Ag NPs onto the AgDVD substrate, and the nucleation density is influenced by both Ag^+ ion concentration and the cathodic overpotential value. In this case the relatively high Ag^+ ion

concentration (10 mM) and the high overvoltage are conditions that produce formation of a large number of small Ag nuclei.²¹ However, a non uniform distribution of the Ag NPs over the AgDVD electrode can be anticipated as a consequence of the nanostructured corrugated substrate. In fact, the NP nucleation and growth depend on the current distribution over the cathode, which determines the local current density on the surface. On the other hand, the current distribution is determined by the geometrical features of the electrode and the cell, the polarization at the electrode surface, and the mass transfer in the electrolyte. When grooves are present on the surface of the electrode, as in this case, the current density is unevenly distributed leading to a faster deposition on the ridges of the corrugated support, because they are closer to the counter electrode. Dendrites nucleation and growth can be expected on the basis of the higher current density present over the DVD ridges.²²

As a matter of fact, the morphological characterization of the AgNPs@AgDVD samples is well in tune with the expected non uniform distribution of the Ag NPs. While a large scale SEM image shows a homogeneous coverage of the patterned DVD surface (**Figure 3.1a**), smaller scale images clearly show that small Ag NPs are present within the valleys of the corrugated electrode, whereas over the ridges the Ag NPs are bigger, more densely packed and in some cases are present as dendrites (Figure 3.1b). This behaviour is completely in agreement with the discussion anticipated above. The analysis of the size distribution of the Ag NPs within the valleys is reported in Figure 3.1c: they present a rather regular round shape with dimension (diameter) peaked at ca 16 nm and a broad distribution ranging from 10 to 25 nm.

The surface area of the AgNPs@AgDVD and AgDVD substrates are determined by AFM (Figure 3.1d) and they are normalized with respect to the scanned area, $25 \mu\text{m}^2$, so resulting in dimensionless numbers equal to 1.23 and 1.10, respectively. As it will be shown later, the AgDVD substrate is not SERS active under the used experimental conditions and therefore in the evaluation of the parameter A of equation 3.1 only the active area (i.e. AgNPs) is accounted for.

In particular it was estimated as:

$$A = \frac{\text{Surface}(\text{AgNPs@AgDVD}) - \text{Surface}(\text{AgDVD})}{\text{Scanned Area}} = 0.13$$

Thus, AFM measurements show that after AgNP deposition the surface area increases by about 13%; nevertheless, a simple visual inspection of the SEM pictures in Figure 3.1 indicates that this value is probably somewhat underestimated.

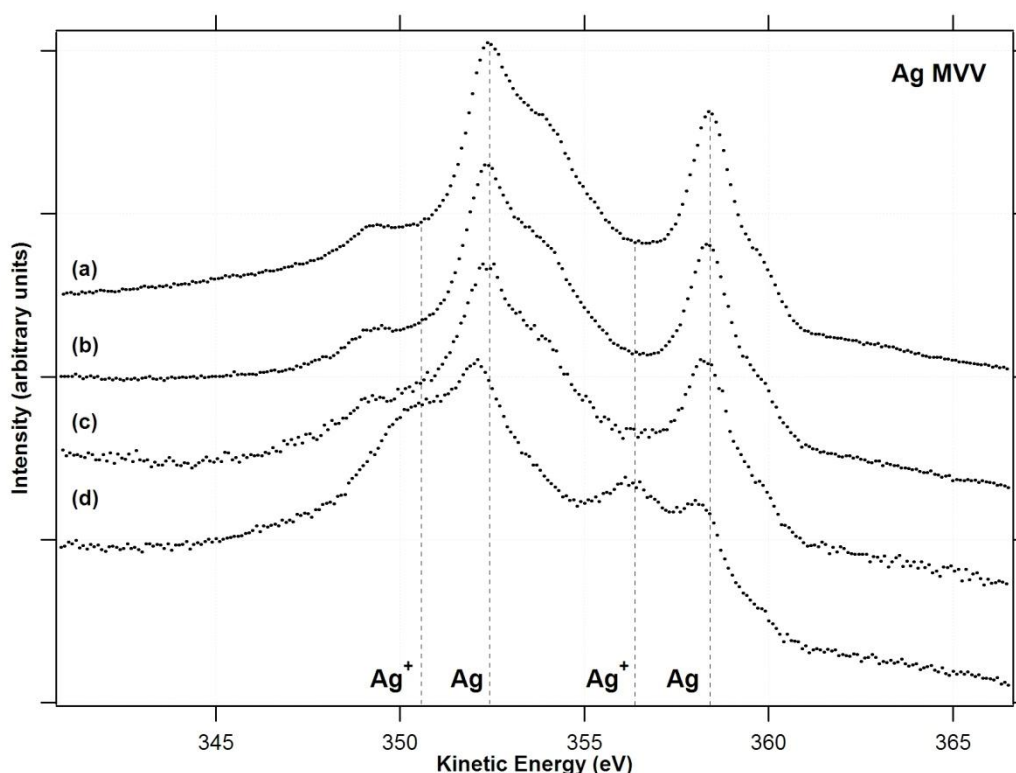


Figure 3.2 Ag MVV X-ray excited spectra obtained from: (a) a clean AgDVD substrate, (b) a freshly deposited AgNPs@AgDVD substrate, (c) the same sample after a 3 month ageing period, (d) the AgNPs@AgDVD substrate after BT

In order to chemically characterize the AgDVD and AgNPs@AgDVD surfaces and to verify their stability, the Auger Ag MVV x-ray excited peaks were recorded. In **Figure 3.2**, the Ag MVV peaks obtained respectively from (a) a clean AgDVD substrate, (b) a freshly deposited AgNPs@AgDVD substrate, (c) the same sample after a 3 month ageing period and (d) the AgNPs@AgDVD substrates after BT functionalization were compared. It is immediately evident that spectra (a) and (b) are almost identical, indicating that the electrochemical preparation of the AgNPs@AgDVD substrate

produces a clean Ag surface. However, by comparing the width of the M_4VV component of the two curves (b) and (c) it turns out that the aged sample, as expected, shows the presence of moderate amounts of Ag^+ . In any case, such an oxidation is very mild. On the contrary, after the BT functionalization the Ag MVV peak is strongly modified by the appearance of a component at a KE of about 350.5 eV (M_5VV) and 356.0 eV (M_4VV) corresponding to the presence of Ag^+ .²³ This evidence suggests that such substrate, once functionalized with the targeted analyte, should be quickly used in order to have reliable SERS measurements.

3.4 Optical measurements

3.4.1 Diffuse Reflectance Measurements

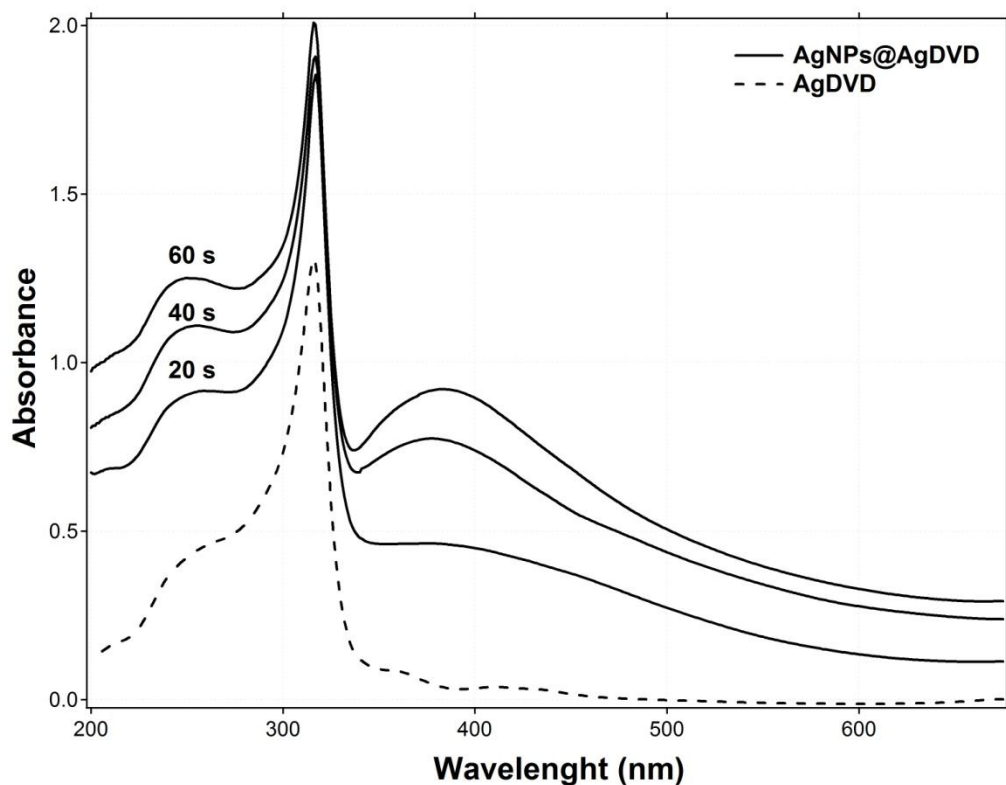


Figure 3.3 UV-Vis Diffuse Reflectance measurements in the 200-800 nm range for the AgDVD and AgNPs@AgDVD samples at increasing deposition times (20, 40 and 60s).

In **Figure 3.3** the UV-Vis Diffuse reflectance measurements in the 200-800 nm range for the AgDVD and AgNPs@AgDVD samples at increasing electrodeposition times (20, 40 and 60s) were reported. The growth of Ag NPs on DVD is inferred from the appearance of the plasmonic band at about 390 nm. Its intensity rises in time due to the increasing NP size²⁴ and/or to the appearance of new nucleation sites and their subsequent growth during the process of electrochemical deposition.

The peak at 320 nm is attributed to Ag inter-band transitions.^{25,26} The broad tail of the absorbance in the lower energy spectral region indicates the presence of NP aggregates and/or NPs of different shapes and sizes:^{27,28}

3.4.2 Surface Enhanced Raman Scattering Measurements

SERS spectra were first carried out on AgDVD functionalized with BT at 488, 514.5 and 632.8 nm for three laser polarizations (TE - Transverse Electric, TM - Transverse Magnetic and 45E, where the electric field vector lies perpendicular, parallel and at 45° with respect to the grating vector, respectively). The absence of Raman signal on AgDVD at all wavelengths and polarization configurations indicates that the grating does not provide any appreciable local field enhancement under the used experimental conditions. In this respect, it is worth reminding that plasmonic properties of optical disks have been recently investigated by Kaplan:²⁹ reflection spectra recorded by ellipsometry on the Ag surface of DVD show unclear and broad resonances throughout the visible region due to the rectangular shape of the DVD pattern. Such broad resonances are normally associated to low field enhancement: this is therefore in agreement with the absence of SERS activity under the used experimental conditions. Nevertheless it can not be excluded that surface plasmons could be more efficiently excited by using a different geometry for the excitation source (i.e. incident angle far from surface normal).

On the contrary, BT functionalized AgNPs@AgDVD samples show a remarkable SERS effect. In order to derive an extensive characterization of

such substrates, several sets of measurements were carried out. Nine samples (all obtained with the same preparation procedure and indicated with numbers from 1 to 9) have been characterized at different excitation wavelengths: sample 1-3 at 488 nm, sample 2-6 at 514.5 nm and sample 7-9 at 632.8 nm. Measurements have been collected from 10 different (random) positions of the sample at three different laser polarizations with respect to the groove (TE, TM, 45E). This set of measurements allows to evaluate the reproducibility and repeatability of the samples, where reproducibility refers to the point-to-point variation and repeatability to the sample to sample one.³⁰

λ [nm]	Sample	Polarization	EF*10 ⁻⁵
488	1	TE	1.3 ± 0.2
	1	45E	1.4 ± 0.3
	1	TM	1.3 ± 0.2
514.5	4	TE	1.2 ± 0.2
	4	45E	1.2 ± 0.1
	4	TM	1.2 ± 0.1
632.8	7	TE	6.5 ± 0.7
	7	45E	7 ± 1
	7	TM	7 ± 1

Table 3.1 EF values and Standard Deviations (SDs) for different polarizations (see text) calculated from Raman spectra collected at 10 different (random) points on the same sample.

First of all the effect of the polarization was evaluated. In **Table 3.1** the EFs and the corresponding Standard Deviation (SD) of measurements with different polarizations on the same sample, calculated from the analysis of 10 points were reported: clearly, there is no polarization dependence in the measured EF values. This is consistent with a random-like distribution of the NP in the few micrometer spatial region (i.e. laser spot) despite a long range order on the NP arrangement induced by the templating effect of the DVD surface. In **Table 3.2** the EFs and corresponding SD measured for each sample (column 3) were reported. Since no polarization dependence can be inferred from the experimental data, the EFs and SDs values reported in Table 3.2 are worked out from the analysis of 30 points (10 points per polarization averaged together).

λ [nm]	Sample	$EF \cdot 10^5$	RSD Reprod. [%]	$EF \cdot 10^5$	RSD Repeat. [%]
488	1	1.3 ± 0.2	15 %	1.36 ± 0.09	6 %
	2	1.3 ± 0.2	16 %		
	3	1.5 ± 0.2	14 %		
514.5	4	1.2 ± 0.2	13 %	1.18 ± 0.09	8 %
	5	1.1 ± 0.1	12 %		
	6	1.2 ± 0.2	12 %		
632.8	7	7 ± 1	17 %	6.4 ± 0.5	8 %
	8	7 ± 1	15 %		
	9	6 ± 1	17 %		

Table 3.2 EF values (with corresponding standard deviations), and relative standard deviation (RSD) providing an estimate of reproducibility and repeatability, (see text for definitions) obtained from the different samples (1-9) analysed in this study.

In column 5 the EFs of the three samples measured at the same excitation wavelength are averaged together. In conclusion the Relative Standard Deviation (RSD) in column 4 and 6 provides an estimation of reproducibility and repeatability, respectively.

The trend of the EF as a function of the excitation wavelength does not follow the shape of the AgNPs@AgDVD absorbance spectrum reported in Figure 3.3. This is not surprising since, although in the case of a single NP a qualitative correspondence between SERS enhancement and extinction spectrum may exist, this behaviour is not expected when collective plasmon resonances are present.²⁸ Actually, the presence of NP aggregates and NPs of different shape and size is evident both from the reflectance measurements and from the SEM images. The EFs have comparable values throughout the explored spectral region. This behaviour is of course very useful for the amplification of large Raman shifts; moreover, the fact that the highest EF occurs at 632.8 nm comes in handy for the measurement of fluorescent compounds and for the compensation of the relatively low Raman signals at that wavelength due to the ω^4 dependence.

	<i>Type of substrate</i>	<i>Ref.</i>	<i>Reprod.</i> <i>[%]</i>	<i>Repeat.</i> <i>[%]</i>	λ <i>[nm]</i>	<i>EF</i>
1	Vapor deposited Ag film	31	14	27	514.5	n.d.
2	Vapor deposited Ag film (annealed)	31	14	14	514.5	n.d.
3	Roughned Ag electrode	31	14	40	514.5	n.d.
4	Acid-etched Ag foil	31	7	17	514.5	n.d.
5	Tollens-produced Ag film	31	14	Very poor	514.5	n.d.
6	Photoreduced Ag film on Titania *	31	8	50	514.5	n.d.
7	Three-layer substrate	32	13	12	632.8	Low
8	Silver Nano-rod array	33	10	15	785	Very High
9	Silver elliptical disks *	34	12-28	n.d.	632.8	High
10	Ag in polyelectrolyte multilayers	35	6	10	514.5	Very High
11	Nanogap DUV Ag substrates	30	3-5	n.d.	632.8	Very High
12	Silver film over nanosphere	30	11-14	n.d.	632.8	Very High
13	Fs-laser nanostructured substrates	36	12.5	12.9	632.8	Very High
14	Closely packed nanoembossed arrays	37	<10	<10	632.8	High
15	Dendritic Silver *	38	19.6	n.d.	785	Low
16	Tapered pillar arrays	39	15	n.d.	785	Very High
17	Sub-wavelength nanohole array	40	10	n.d.	632.8	Low
18	CD platform *	41	10	25	785	n.d.
19	Electrochemical growth on DVD	this thesis	15	6	488	High
			12	8	514.5	High
			16	8	632.8	High

Table 3.3 Comparison of reproducibility, repeatability and EF values (see text for definitions) for several Ag based SERS substrates taken from literature data (n.d.= not determined, EF grade: Low < 10^5 , 10^5 < High < 10^7 , Very High > 10^7). (* Due to the nature of the specimen it is not univocally defined the point-to-point reproducibility and the sample-to-sample repeatability. Therefore, for a precise evaluation, the reader is invited to refer to the original paper).

As a whole, the data of Table 3.2 shows EFs in between 1 and $\sim 7 \cdot 10^5$, which are consistent with values reported for electrochemical roughened surfaces by other authors.^{7,42}

Finally, it is important to remark the reproducibility and repeatability of these SERS substrates. The reproducibility exhibited by the AgNPs@AgDVD samples is about 15%, while repeatability turned out to be around 8% (see Table 3.2). These values lie well within the criteria that Natan proposed as benchmarks for SERS substrates,⁴³ that is less than 20% for the spot to spot and for the substrate to substrate variations.

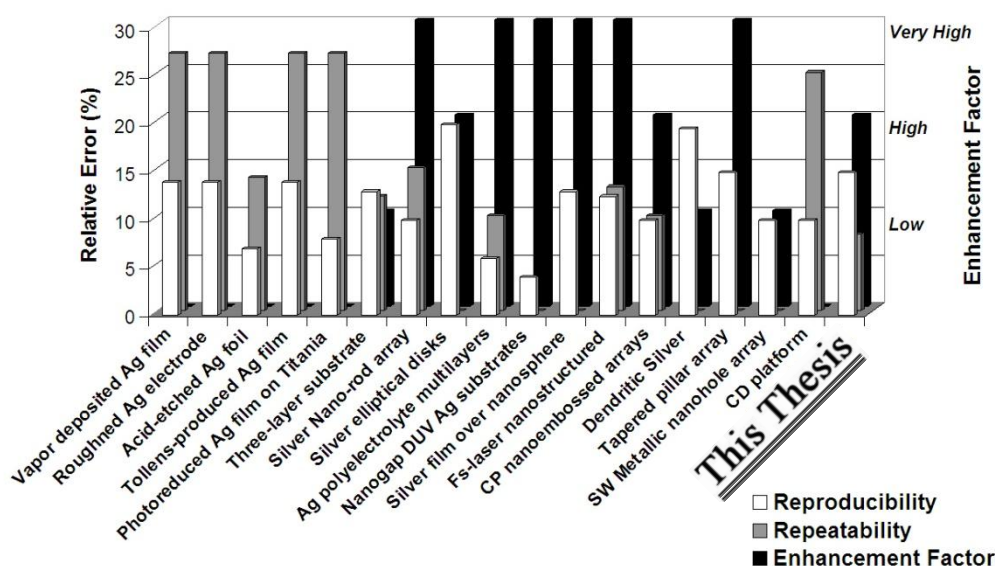


Figure 3.4 Comparison between literature data of several Ag based SERS substrates and the results of this study (EF values, reproducibility and repeatability) values (see Table 3.3 for the pertinent references).

For the sake of comparison, in **Table 3.3** and **Figure 3.4** the obtained results were collected along with literature data from several papers that quantitatively evaluate the EFs, the reproducibility and the repeatability for Ag based SERS substrate. EF values in Table 3.3 are expressed as VERY HIGH, HIGH and LOW accordingly to Ref. 44 (see caption of Table 3.3). A VERY HIGH EF value potentially allows single molecule detection.⁴⁴ According to such classification, AgNPs@AgDVD SERS substrates provide a HIGH EF value. In addition, from the data in Table 3.3 it can be pointed out how the reproducibility of these samples compares very well with the other

data; as for the repeatability, AgNPs@AgDVD performs significantly better than the other substrates. Moreover, it is remarkable that these results are achieved on quite large area substrates (about 1 cm²) compared to samples prepared with methods like Nanosphere Lithography where ordered areas in the order of 10-100 μm² can only be achieved.⁴⁵

Taking for granted the so called *SERS uncertainty principle*⁷ which states that:

$$(\text{Substrate reproducibility}) \times (EF) = \text{Constant}$$

a trade off between the two factors at the left hand side has to be fulfilled: depending on the type of application of course reproducibility/repeatability (quantitative bioassays of relatively abundant species) or EF (qualitative detection of chemical agents) may be required to dominate. With this respect, on the basis of the previous considerations, such substrates match both ends and therefore can be considered very good and convenient SERS substrates.

3.5 Conclusions

The novelty of this study relies on the exploitation of a very cheap and widely available Ag surface (i.e. inner surface of a commercial DVD) to fabricate a SERS substrate. The electrochemical growth used to deposit Ag NPs is an easy and relatively inexpensive process, which ultimately provide an *easy&cheap* SERS substrate.

Such peculiarities, together with the good SERS properties obtained (reproducibility and repeatability around 15% and 8% respectively, EF up to 7*10⁵), make this procedure a practical alternative for the fabrication of cost-effective and disposable SERS substrates possibly enabling mass production. Further improvement of the substrate could be achieved by making also AgDVD SERS active, in order to combine the substrate and the AgNP plasmonic properties. In the literature Kaplan²⁹ has already shown how to tune in an easy way the AgDVD morphology to strengthen its plasmonic

response, even though the substrate SERS properties have not been investigated yet.

References

- 1 M. Fleischmann, P. J. Hendra and A. J. McQuillan, *Chem. Phys. Lett.* **1974**, **26**, 163
 - 2 D. Graham and R. Goodacre, *Chem. Soc. Rev.* **2008**, **37**, 883
 - 3 G. A. Baker and D. S. Moore, *Anal. Bioanal. Chem.* **2005**, **382**, 1751
 - 4 S. Maier, *Plasmonics: Fundamentals and Applications*, Springer, New York **2007**
 - 5 E. C. Le Ru, E. Blackie, M. Meyer and P. G. Etchegoin, *J. Phys. Chem. C* **2007**, **111**, 13794
 - 6 S. Lal, N. K. Grady, J. Kundu, C. S. Levin, J. B. Lassiter and N. J. Halas, *Chem. Soc. Rev.* **2008**, **37**, 898
 - 7 R. J. C. Brown and M. J. Milton, *J. Raman. Spectrosc.* **2008**, **39**, 1313
 - 8 X. Zhang, J. Zhao, A. V. Whitney, J. W. Elam and R. P. Van Duyne, *J. Am. Chem. Soc.* **2006**, **128**, 10304
 - 9 L. Qin, M. J. Banholzer, J. E. Millstone and C. A. Mirkin, *Nano Lett.* **2007**, **7**, 3839
 - 10 D. P. Fromm, A. Sundaramurthy, A. Kinkhabwala, P. J. Schuck, F. S. Kino and W. E. Moerner, *J. Chem. Phys.* **2006**, **124**, 061101
 - 11 R. Alvarez-Puebla, B. Cui, J.-P. Bravo-Vasquez, T. Veres and H. Fenniri, *J. Phys. Chem. C* **2007**, **111**, 6720
 - 12 M. Erol, Y. Han, S. K. Stanley, C. M. Stafford, H. Du and S. Sukhishvili, *J. Am. Chem. Soc.* **2009**, **131**, 7480
 - 13 H. Z. Yu, *Chem. Commun.* **2004**, 2633
 - 14 F. Ramiro-Manzano, E. Bonet, I. Rodriguez and F. Meseguer, *Langmuir* **2010**, **26**, 4559
 - 15 B. Kaplan, H. Guner, O. Senlik, K. Gurel, M. Bayindir and A. Dana, *Plasmonics* **2009**, **4**, 237
 - 16 D. Lin-Vien, N. B. Colthup, W. G. Fateley and J. G. Grasselli, *The handbook of Infrared and Raman characteristic frequencies of organic molecules*, Academic Press:New York **1991**.
-

- 17 G. Varsanyi, *Vibrational spectra of benzene derivatives*, Academic press:New York **1969**.
- 18 K. B. Biggs, J. P. Camden, J. N. Anker and R. P. Van Duyne, *J. Phys. Chem. A* **2009**, 113, 4581.
- 19 C. L. Haynes and R. P. Van Duyne, *J. Phys. Chem. B* **2003**, 107, 7426
- 20 M. Haataja, D. J. Srolovitz and A. B. Bocarslyb, *J. Electrochem. Soc.* **2003**, 150, 10, C708
- 21 A. T. Dimitrov, S. Hadzi Jordanov, K. I. Popov, M. G. Pavlovic and V. Radmilovic, *J. Appl. Electrochem.* **1998**, 28, 791
- 22 K. I. Popov, P. M. Zivković, S. B. Krstic and N. D. Nikolic, *Electrochim. Acta* **2009**, 54, 2924
- 23 G. I. N. Waterhouse, G. A. Bowmaker and J. B. Metson, *Surf. And Interface Anal.* **2002**, 33, 401
- 24 S. Link and M. A. El-Sayed, *J. Phys. Chem. B*, **1999**, 103, 8410
- 25 F. Wooten, *Optical properties of solids*, Academic Press, **1972**
- 26 A. Henglein, *J. Phys. Chem.* **1993**, 97, 5457
- 27 K. Kneipp, H. Kneipp, I. Itzkan, R. R. Dasari and M. S. Feld, *J. Phys.: Condens. Matter* **2002**, 14, R597
- ²⁸ E. C. Le Ru, C. Galloway and P. G. Etchegoin, *Phys. Chem. Chem. Phys.* **2006**, 8, 3083
- 29 B. Kaplan, H. Guner, O. Senlik, K. Gruel, M. Bayindir and A. Dana, *Plasmonics* **2009**, 4, 237
- 30 U. S. Dinis, F. C. Yaw, A. Agarwal and M. Olivo, *Biosens. and Bioelectron.* **2010**, doi:10.1016/j.bios.2010.08.069.
- 31 K. L. Norrod, L. M. Sudnik, D. Rousell and K. L. Rowlen, *Appl. Spectrosc.* **1997**, 51, 994
- 32 S. P. Mulvaney, L. He, M. J. Natan and C. D. Keating, *J. Raman Spectrosc.* **2003**, 34, 163
- 33 J. D. Driskell, S. Shanmukh, Y. Liu, S. B. Chaney, X. J. Tang, Y. P. Zhao and R. A. Dluhy, *J. Phys. Chem. C* **2008**, 112, 895
- 34 J. M. Oran, R. J. Hinde, N. A. Hatab, S. T. Retter and M. J. Sepaniak, *J. Raman Spectrosc.* **2008**, 39, 1811
-

-
- 35 J. Zhou, S. Xu, W. Xu, B. Zhao and Y. Ozaki, *J. Raman Spectrosc.* **2009**, 40, 31
- 36 E. D. Diebold, N. H. Mack, S. K. Doorn and E. Mazur, *Langmuir* **2009**, 25, 1790
- 37 D. Jung, Y. M. Lee, Y. Lee, N. H. Kim, K. Kim and J. K. Lee, *J. Mater. Chem.* **2006**, 16, 3145
- 38 L. He, M. Lin, H. Li and N.J. Kim, *J. Raman Spectrosc.* **2010**, 41, 739
- 39 M. R. Gartia, Z. Xu, E. Behymer, H. Nguyen, J. A. Britten, C. Larson, R. Miles, M. Bora, A. S. P. Chang, T. C. Bond and G. L. Liu, *Nanotechnology* **2010**, 21, 395701
- 40 V. Canpean and S. Astilean, *Lab on a Chip* **2009**, 9, 3574
- 41 D. Choi, T. Kang, H. Cho, Y. Choi and L. P. Lee, *Lab On a Chip* **2008**, 9, 239
- 42 X. M. Lin, Y. Cui, Y. H. Xu, B. Ren and Z.Q. Tian, *Anal. Bioanal. Chem.* **2009**, 394, 1729
- 43 M. J. Natan, *Faraday Discussion* **2006**, 132, 321
- 44 E. Le Ru and P. Etchegoing, *Principles of Surface Enhanced Raman Spectroscopy and related Plasmonic effects*, Elsevier, Amsterdam **2009**.
- 45 X. M. Lin, Y. Cui, Y. H. Xu, B. Ren and Z. Q. Tian, *Anal. Bioanal. Chem.* **2009**, 394, 1729
-

Chapter 4

Growth and optical properties of Silver Nanostructures obtained on Connected Anodic Aluminum Oxide Templates^{*}

4.1 Introduction

In this chapter a template based approach that uses Anodic Aluminum Oxide (AAO) membranes to obtain ordered arrays of AgNSs to be used as SERS substrate or as LSPR sensor will be described. As it is well known, 2D ordered metal arrays can provide an ideal platform for sensing and imaging of surface binding events¹. Because of their novel properties and their wide-range potential applications², one-dimensional (1D) nanomaterials (e.g. nanowires, NWs, nanorods, NRs and nanotubes, NTs, especially when arranged in 2D arrays) have attracted extensive interest in physics and chemistry. Generally, surface plasmon resonance (SPR) and surface-enhanced Raman scattering (SERS) are two alternative sensing techniques based on plasmonic materials. SPR is at the basis of real-time sensors which monitor the changes in the dielectric environment at the surface exploiting the properties of surface plasmons polaritons (SPPs).³ Alternatively, sensors based on nanoparticles (NPs) arrays of plasmonic materials give rise to localized surface plasmon resonances (LSPRs) which can be tuned by controlling the size, shape and spacing of the nanostructures (NSs). Very recently, bimodal sensors, based both on SERS and SPR, have been proposed with the advantage that a *chemical* information can be extracted

^{*} G. Giallongo, C. Durante, R. Pilot, D. Garoli, R. Bozio, F. Romanato, A. Gennaro, G. A. Rizzi and G. Granozzi, *Nanotechnology* **2012**, 23, 325604

from the Raman signal in tandem with a nonspecific SPR detection in reflectivity mode.⁴

Among the several methods available to prepare 2D arrays of metallic NSs, template assisted synthesis represents an important methodological route with a large variety of alternatives:⁵ in this area, electrochemical (EC) methods exploiting various templating masks represent a much valid tool to prepare 2D arrays of 1D NSs with different diameters and lengths. To this end, AAO membranes have been intensively exploited:^{6, 7} the AAO pores are hexagonally regularly spaced in an area of several mm², with a very low defectivity level (i.e. intersections between adjacent pores). By simply changing the anodization time or the solution used in the anodizing bath, it is possible to vary the thickness of the AAO film or the pore diameter (ranging from ca 10 to 400 nm), which allows one to control the aspect ratio of the grown NSs. Also the pitch between the pores can be tailored, so enabling the study of coupling or ensemble effect in the 2D array.⁸

An important example of ensemble effect on SERS, obtained with the use of AAO membranes, has been reported in 1995.⁹ At that time the obtained results did not attract much attention, as the achieved SERS Enhancement Factor (EF) was lower than the one obtained from Ag colloids. However, since then it was realized that to make a step forward in the application of SERS as a reliable detection technique in real sensors, the preparation of ordered nanostructured substrates is most beneficial to increase the reproducibility of the SERS measurements and to fine tune the plasmonic response of the SERS substrate. Actually, local fluctuations in surface morphology can lead to dramatic drop of the reproducibility. Thence, in recent years, SERS-optimized nanostructured surfaces have been tailored by a wide variety of techniques, including nanosphere lithography,¹⁰ on-wire lithography,¹¹ e-beam lithography,¹² and nanoimprint lithography.¹³ Their performances have been recently reviewed and the important concept of finding a compromise between reproducibility and EF value has been clearly pointed out.¹⁴

For these reasons, AAO templates as a tool to obtain SERS sensors have been recently further explored.^{15, 16} The AAO membrane is usually grown on an pure Al sheet and is electrically isolated from the metal substrate, due to

the formation of a barrier layer during the anodization process. The EC deposition of metal NRs inside the pores can be performed by (i) either detaching the AAO membrane from the Al substrate (often called as *attached membrane*) and using the free standing membrane as a template to be transferred on the working electrode (only applicable for free-standing membranes that are thick $>20\ \mu\text{m}$) or (ii) by maintaining the AAO layer on the Al substrate (often called as *connected membrane*) and performing the EC deposition by Alternating Current (AC) with a sufficiently high frequency. For many applications where an aspect ratio for the grown NR close to 8 – 10 is targeted, the (i) procedure becomes difficult and tedious.¹⁷ In these cases, the route (ii) is preferred. Moreover, focusing again on SERS substrates, it has been demonstrated that the best SERS AAO based substrates are obtained by partially etching the AAO membrane after the metal deposition, so that the metal NRs are still partially immersed in the Al_2O_3 matrix, but their head protrudes out of the honeycomb oxide structure:^{18, 19} if the AAO membrane is etched for a long enough time, the metal NRs eventually collapse, touching each other by the edges and thus forming an ordered array of effective SERS hot-spots.

Very interestingly, densely packed and optically coupled plasmonic NPs arrays composed of gold spheroids have been recently obtained by Extreme UV Interference Lithography and used as a LSPR biomolecular sensors.²⁰ A similar system could be virtually obtained in a much easier way by filling the AAO pores with metal NRs characterized by an aspect ratio of about 2-3 and keeping the length of the AAO pores sufficiently short (about 200 nm). With this idea in mind, that is, obtaining substrates that can be used, both as a SERS or as a LSPR sensor, in this chapter an *easy&cheap* procedure to obtain sensors substrates, based on ordered arrays of Ag NSs by using ultrathin AAO *connected* membranes (easy to obtain and handle) where the pores can be used to electrodeposit Ag NSs by AC was described and discussed. By carefully optimizing the deposition procedure, it is possible to tailor different Ag NSs, with different optical properties, i.e. Ag NRs, NTs or NWs, keeping, at the same time, a control on their length. It is possible to easily avoid, by using AC electrodeposition, the overflow outside the pores and experimental evidences of the partial filling of the AAO pores have been

obtained for the first time by the use of Angle Resolved X-ray Photoemission Spectroscopy (AR-XPS) measurements. At the same time, the AR-XPS method allows to accurately monitor the etching process in a dilute NaOH solution, i.e. controlling the partial removal of the AAO membrane so that the final metal NSs can protrude out of the AAO membrane. It was demonstrated here, by preliminary optical measurements, that by tailoring the preparation procedure, either a SERS or a LSPR sensor can be obtained.

4.2 Experimental Section

The AAO samples were fabricated by anodization of high purity aluminum foils (Puratronic 99.998%, Alfa Aesar), in a home-made EC cell. The anodized area was about 200 mm². Prior to the anodization process the samples were sonicated in ethanol for 5 minutes in an ultra-sound bath and electropolished in a HClO₄/C₂H₅OH mixture (ratio 1/3) at 1°C, with a 20 V potential applied for 5 minute (Hameg, HMP 4030). The aluminum electrode was set as the anode against a platinum ring counter electrode and was electropolished to a mirror-like finish and then rinsed in distilled water. In order to obtain better organized structures, a two step anodization method was employed, improving the method of Masuda,²² who first proposed a double anodization step. First and second anodization were carried out in 0.3 M oxalic acid with a constant potential of 40 V, at 15°C. A set of 5 aluminum-working electrodes were connected in parallel and set at a distance of 0.7 mm around a platinum ring counter electrode. Between the two anodizing step, the alumina layer was removed, etching the samples in a 0.4 M H₃PO₄/0.2 M H₂CrO₄ solution, at 60°C. After the anodizing process, the samples were treated in 0.4 M H₃PO₄ for reducing the oxide layer thickness and for widening the pores. The times of anodizing, etching and pore widening were optimized for a better control of the pore lengths and additional details are reported within the main text.

The Ag electrodeposition was carried out in an EC reactor where the AAO electrode and a silver bar electrode were set as working and counter

electrode, respectively. The AC signal, applied across the AAO layer electrode was generated using a TTI-TG230 arbitrary function generator and was amplified with an InterM-A120 amplifier to the desired voltage. The electrolyte was 10 mM AgNO₃ + 0.5 M H₃BO₃ for all depositions. Current density transients during the anodization and electrodeposition processes were monitored using a home-made LabView program that controls the EC set up, enabling current measurements while applying electrodeposition.

The chemical characterization of the sample surface was obtained by XPS using a VG ESCALAB MK II (Vacuum Generators, Hastings, England) system (base pressure of 1×10^{-7} Pa) equipped with a twin anode (Mg/Al) X-ray source with a hemispherical electrostatic analyzer and a five-channeltron detector. The sample is mounted on a two-axis goniometer capable of sample rotations in polar angle θ (defined with respect to the sample surface) and in azimuthal angle Φ thereby allowing to collect AR-XPS data. The angular accuracy is always better than $\pm 1^\circ$ in both directions. The angular acceptance of the analyzer is 8° . All the spectra reported were collected using Al K $_{\alpha}$ excitation energy. The peak intensities were determined after a linear background subtraction. The binding energy (BE) scale was calibrated with respect to Pt 4f_{7/2} (71.0 eV) measured on an Pt(111) single crystal.

SEM investigations were performed with a dual beam FEI Nova 600i instrument, with a semi-in-lens cold cathode field emission scanning electron microscope source. The micrographs were taken at 5 kV accelerating voltage, using in-lens detector in pure secondary electron signal mode. FIB cross section was performed by means of the ion source of the dual beam system using 30KeV of accelerating voltage.

SERS measurements were recorded by using a micro-Raman setup. A diode laser working at 785 nm (XTRA, Toptica Photonics AG) was used as excitation light source. The laser beam was coupled to a microscope (Olympus BX 40) and focused on the sample by a 20x objective (Olympus SLMPL, NA=0.35). Back-scattered Raman signal was separated from the Rayleigh scattering by an edge filter, analyzed with a 320 mm focal length imaging spectrograph (TRIAX-320 ISA) and a liquid nitrogen cooled CCD

camera (Spectrum One, Jobin Yvon). The typical spot diameter at the focus was about 3 μm .

Diffuse reflectance measurements were recorded on a Jasco V-570 spectrophotometer equipped with a Jasco ISN-470 integrating-sphere apparatus. The studied wavelength range was 200–800 nm.

4.3 Results and Discussion

4.3.1 AAO preparation by anodization and AC electrodeposition of Ag

In general, the anodization of an ultrapure aluminum foil can result in two different types of oxide film: either a barrier-type anodic film, or a porous oxide film depending on the nature of the electrolyte used for anodizing aluminum. In fact, a strongly adherent, non-porous and non-conducting

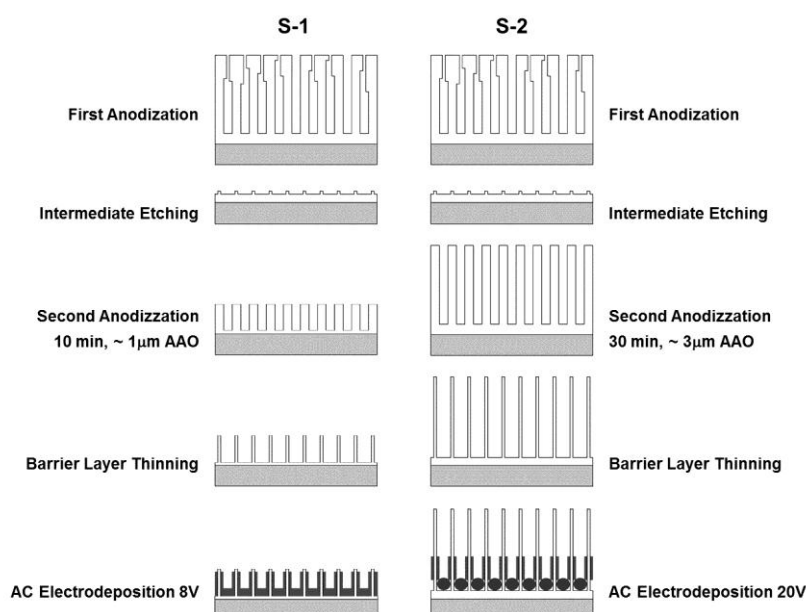


Figure 4.1 Representation of anodization, etching and electrodeposition procedures used to prepare the different samples S-1 and S-2 studied in the present study.

barrier-type anodic film on aluminum can be formed by anodizing in almost neutral solutions, such as boric acid, ($\text{pH} = 5\text{--}7$) where the anodic oxide layer

is not chemically affected and remains practically insoluble. In contrast, porous oxide films can be formed by anodizing in strongly acidic solutions, such as sulfuric and oxalic acid, where the resulting oxide film is only sparingly soluble:²¹ the film growth is associated with localized dissolution of the oxide, as a result of which pores are formed in the oxide film. It is well established that hexagonally ordered porous alumina membranes can be prepared via a two-step anodization process following the so-called Masuda methods.²² The method involves a first anodization, which causes the formation of channel-arrays with a high aspect ratio and regular pore arrangements via self-organization. The dissolution of the porous layer by an etching solution of H_3PO_4 and H_2CrO_4 exposes regular hexagonal texture, which acts as a self-assembled mask for a second anodization process.²³ After a second anodization an ordered nanopore array is obtained with straight pores from top to bottom and a thickness that depends upon the duration of the second anodization step. Concerning the synthesis of the AAO used in the present study, the most favorable conditions was found to be: first anodization 120 min, second anodization 10-30 min, chemical etching between the two anodizing steps 90 min, barrier thinning in H_3PO_4 30 min. In particular, the time of the second anodization has been varied from 10 to 30 min and all the other parameters have been maintained identical: this resulted in an AAO layer with a thickness between $\sim 1 \mu\text{m}$ (10 min) and $\sim 3 \mu\text{m}$ (30 min) (see **Figure 4.1**).

The possibility to use AAO as a templating mask for the production of 1D NSs (e.g. NRs, NTs or NWs) relies on the fact that metal ions are preferentially electrodeposited within the pores, since pores offer the least impedance path between working and counter electrode. Therefore, the electrodeposition starts at the bottom of the pore where the applied potential results less attenuated and the force lines are more packed.²⁴ With the progress of the electrodeposition, the deposited metal offers a preferential channel for the current to flow and therefore favors the growing of the rods instead of the nucleation of new metal sites on the pore walls. The commonly employed DC electrodeposition on AAO is problematic due to the insulating character of the barrier layer oxide, which blocks the direct current and, since the intrinsic resistance is high, the ohmic heating results in the final

breakdown of the oxide layer. In agreement with what already reported in literature,²⁵ it was observed that a thinning procedure, which allows one to reduce the barrier layer, helps to overcome the resistivity of the AAO. Nevertheless the DC electrodeposition results in a non-uniform pore filling and in a general tendency to produce dendrites. For this reason AC or pulsed current deposition methods appear the best choice to obtain a more uniform deposition inside the pores. AC deposition has been adopted for this work also because it is preferable for industrial scale processes or applications where a rapid and simple method of template production is required, and because it does not require extremely sophisticated instrumentation and produces appreciable results at moderate costs.

In the AC electrodeposition, the metal is deposited inside the pores during the cathodic half-cycles and is dissolved again during the anodic half-cycles; however since the barrier layer under the AAO films functions as a rectifier, that preferentially conducts the cathodic current, it results in a low re-oxidation of the deposited metal during the anodic polarization.²⁶ AC electrodeposition carried out on samples prepared increasing the anodization time of the second step (10, 20, 30 min), gives identical response in term of current density values, in the range of the fixed applied tensions of 5 to 20 V. Therefore, it appears that, the second anodization step does not affect the thickness of the barrier layer and therefore the ohmic drop at the interphase. On the contrary, the chemical etching between the two anodizing steps reduces significantly the barrier layer since it has been observed that a prolonged chemical etching allows the EC filling of the pores with Ag at a lower voltage. The final thinning process improves the quality and the homogeneity of the AC electrodeposition since it reduces the thickness of the barrier layer and widens the pores. The result is to lower the voltage necessary to perform the electrodeposition and to improve the mass ions transfer to the electrode.

In the present thesis two types of samples will be discussed, i.e. S-1 and S-2: in Figure 4.1 the scheme of the sequence of operations and parameters used to obtain them is shown. In both cases the electrodeposition process was carried out in a AgNO_3 10 mM solution (borate buffered), but S-1 was obtained by a constant tension of 8 V on an AAO layer a thickness of $\approx 1 \mu\text{m}$,

whereas S-2 was prepared using a voltage of 20 V on a thicker AAO substrate ($\approx 3 \mu\text{m}$). The optimal deposition frequency was found ranging within 150-180 Hz, whereas at higher frequencies (300 Hz) any deposition was not observed, while at lower frequencies (80 and 40 Hz) there was the formation of dendrites and a non-uniform deposition over the alumina membrane.

Finally, it is important to point out that the AC electrodeposition allows a strictly control of the NSs lengths by tuning the operational conditions. In particular, it was observed that prolonging the deposition time results in a better filling of the pore, but it does not affect the NSs length indicating a self-limited growth. This effect must be referred to an electrodeposition rate higher than that of the metal ion transport through the pores. When this is the case, the metal ion concentration decreases at the interphase and a concentration gradient is established along each pore.²⁷ Thus, since during AC electrodepositions there are not delay times, which would allow to re-establish the initial concentration, a state of ion depletion persists in the pores at all times. Consequently, hydrogen evolution becomes the dominant process and the rods growth results limited (see the following paragraph).²⁸ In the present case, the length of the NSs was established to be about 650 nm (see below), however, different lengths till complete filling of the pore may be obtained changing the applied potential or the concentration of Ag in solution.

4.3.2 SEM and AR-XPS characterization of the Ag nanostructures

SEM images of the *connected* AAO films acquired after barrier layer thinning by etching in H_3PO_4 reveal a very uniform honeycomb structure, having in the case of the thinner AAO membrane (ca $1 \mu\text{m}$) an average pore diameter of ≈ 75 nm and an average wall thickness of about 17 nm, and in the thicker one (ca $3 \mu\text{m}$) an average pore diameter of 65 nm and an average wall thickness of 30 nm. In **Figure 4.2a** and **c** SEM images of the two membranes after the silver AC electrodeposition are reported: it is easy to see in S-1 that

the pores are partially filled (the image is tilted by a few degrees). It is interesting to note the presence of discontinuous Ag NSs grown inside nanopores of S-1. The nature of these NSs will be elucidated in the following. On the other hand, the pores of the thicker S-2 sample appear empty. Also the SEM image is somewhat fuzzy due the partial charging of the sample. As explained in the previous paragraph, the AC Ag electrodeposition is effective only up to a limit height, measured from the bottom of the pores, so that it is not unexpected that for an almost 3 μm thick AAO membrane the pores appear empty.

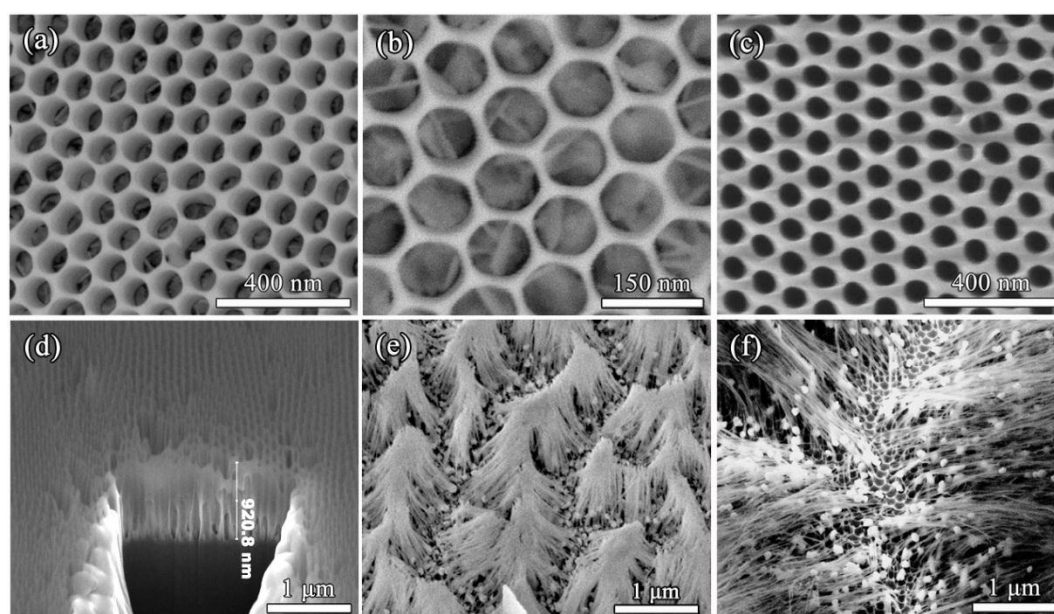


Figure 4.2 SEM images: (a) S-1 as prepared, (b) detail of S-1 pores, (c) S-2 as prepared, (d) S-1 FIB cross section, (e) S-1 etched for 60 s in 50 mM NaOH solution and (f) S-2 etched for 240 s in 50 mM NaOH solution.

A direct evidence of the self-limited growth of the Ag NSs inside the pores has been obtained for the first time by carrying out AR-XPS experiments. In **Figure 4.3** a series of AR-XPS Ag 3d spectra of the thinnest (S-1) AAO substrates after Ag electrodeposition are reported, as function of the emission polar angle θ (from 75° to 90° with respect to the surface). Due to the insulating nature of the Al_2O_3 film that uniformly covers the Al sheet, in all cases the peaks are rigidly shifted to a higher BE by about 2.0 eV. The data reported in the figure have been recalibrated by taking the Al 2p peak as reference. The Ag 3d peak position and the corresponding Auger parameter (not reported) confirm the presence of only metallic Ag. Apart from the charging effect, it is immediately evident that the Ag 3d peak is characterized

by a very strong intensity variation as function of the emission θ angle. In particular, it is possible to observe that, as soon as the emission angle value is below 80° , the Ag 3d peak is strongly attenuated (Figure 4.3a).

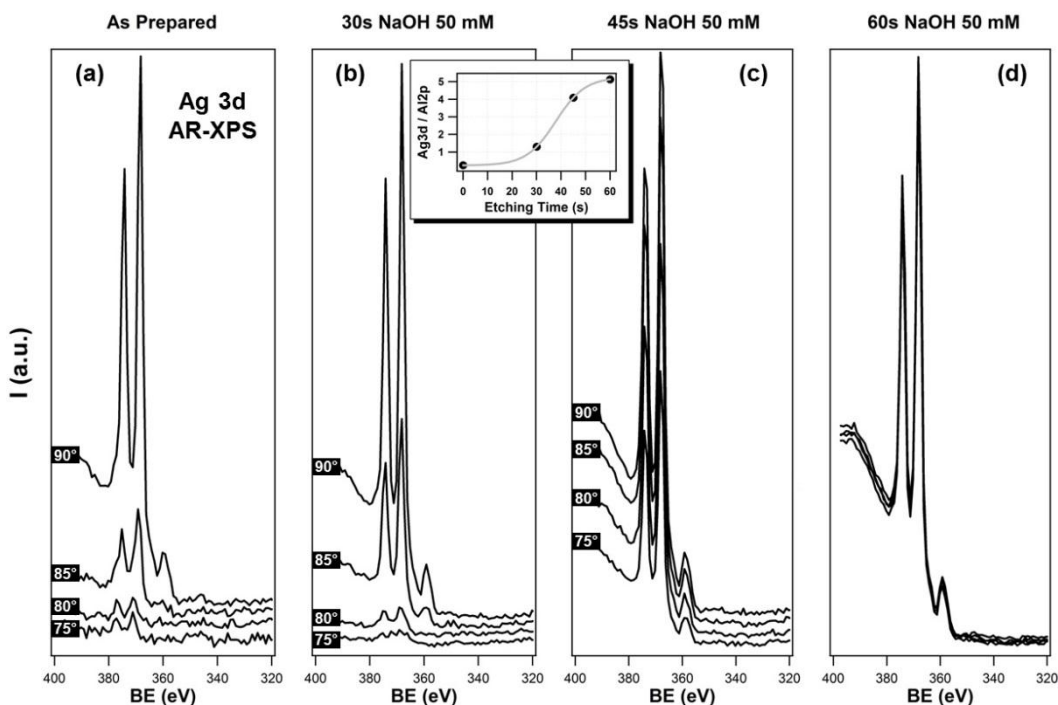


Figure 4.3 Ag 3d AR-XPS spectra of S-1: (a) as prepared and after treatment in 50 mM NaOH solution for (b) 30, (c) 45 and (d) 60 s.

This happens because of the *shadowing* effect of the AAO membrane (see **Figure 4.4**). In fact, if we consider the photoelectrons emitted from the Ag 3d levels, and if we assume that the AAO pores are not completely filled by the Ag NSs (see Scanning Electron Microscopy (SEM) images in the following) it is clear that the photoelectron signal is masked when the emission angle goes below a critical emission limit (θ_L), as depicted in Figure 4.4.

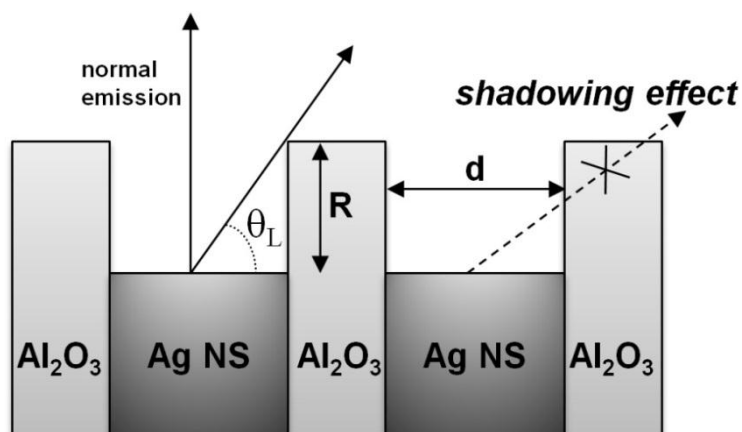


Figure 4.4 Graphical representation of the *shadowing* effect described in the text.

If we assume a simplified model where the emitted electrons come from the topmost Ag layer (i.e. disregarding the attenuation length) and reach an electron analyzer having small acceptance angle, it is straightforward to calculate the height (R) of the empty part of the AAO channel having a diameter d by $R=d/2*\tan(\theta_L)$. We know from SEM measurements (see above) that the average diameter of the pores is ≈ 75 nm for S-1 and from the XPS data of Figure 4.3a we take an estimate of $\theta_L \approx 75^\circ$, so that a rough estimate of R is ≈ 140 nm. A part from the error intrinsic in the absolute value (roughly around 20%), it is interesting to note that this value does not depend on the amount of charge passed during the electrodeposition process since, practically identical ARXPS data have been obtained for samples obtained with 2, 4 and 9 Coulombs. So, apparently, the electrodeposition process is self-limited and it stops as soon as the pores are filled up to $R \approx 140$ nm, regardless of the amount of charge passed through the circuit.

The same AR-XPS methodology can be also applied to follow the AAO etching process when sample is immersed in a dilute NaOH solution. In Figure 4.3 the Ag 3d peak acquired as function of the θ angle after immersion in 50 mM NaOH solution for different etching times (30, 45 and 60 s) is shown. In the Figure 4.3 inset the Ag 3d/Al 2p intensity ratio for an angle $\theta = 85^\circ$ as function of the etching time is reported. It is easy to see how the *shadowing* effect and θ_L decrease as the etching time increases. In other words, the Ag NSs are progressively emerging from the pores as the alumina is etched. After etching the sample for 60 s the intensity variation of the Ag 3d signal with polar angle disappears and the XPS spectra at different angles completely overlap. This means that the Ag NSs are protruding out of the AAO matrix for a length higher than $3\Lambda_e$ where Λ_e represents the inelastic mean free paths of Ag 3d photoelectrons (≈ 1.35 nm). Similar results, were obtained in the case of the thicker AAO layers (S-2), although the etching time necessary to have the Ag NSs exposed out of the AAO membrane was ≈ 240 s.

In order to have an idea of the nature of the Ag NSs grown within the pores, a SEM analysis after a partial etching of the membrane was performed. In Figure 4.2e and f SEM images of S-1 and S-2 etched in NaOH 50 mM

solution for 60 seconds and 240 seconds, respectively, are reported. In Figure 4.2e (S-1) one can observe an over-structure formed by Ag NWs/NTs bunches on a honeycomb nanostructure of Ag NRs. In Figure 4.2f (S-2) the over-structure is still formed by Ag NWs, but, at the base of the Ag NWs it is possible to observe Ag particles characterized by a spheroidal shape and randomly distributed within the NWs bunches with an average diameter of 60 nm (to be reminded that the pores are ≈ 65 nm wide). Thus, it is clear that the AC deposition allows the filling, with compact Ag NRs/spheroids, only of the bottom of the pores. This dual structure (NRs/spheroids + NWs/NTs) is probably due to the nucleation and growth process of Ag crystallites deposited on the AAO pore bottom. The fact that the silver nucleates as roots anchored onto the AAO bottom layer may suggest that the barrier layer is active or conductive enough so that the Gibbs free energy for silver nucleation on the AAO pore bottom is smaller than that of the silver growth.²⁹ Furthermore, the formation of NWs or NTs is driven by the different overpotential that silver ions experience in the two types of AAO. In fact, the potential at AAO surface would decrease as the thickness of AAO layer and pore walls are increased. This means that the overpotential that Ag^+ effectively experiences is small and therefore the nucleation density of Ag NPs is low as a result of a kinetically controlled process. Therefore, it is reasonable to assume that in the case of S-1, in which the AAO layer is thinner than S-2, the applied voltage (8 V) induces a fast nucleation of silver particles, controlled by diffusion, onto the AAO pore surface, shaping a tube-like nanostructure. On the contrary, in the case of S-2 although the applied voltage is 20 V, the overvoltage effectively experienced by Ag^+ results to be lower than in the case of S-1 because of thicker walls of AAO pore layer. Therefore, the nucleation onto the AAO pore wall of S-2 is reduced because it is controlled by the kinetics of silver reduction. Thus, silver preferentially grows over the existing nuclei, rather than forming new sites on the pore wall and this drives nanostructure to grow preferentially with a wire shape. From SEM images we can have a rough estimate of these collapsed Ag NWs/NTs: the average diameter is 20 - 30 nm, while their average length is 600 nm. A corroboration to these data comes from a Focused Ion Beam (FIB) cross-section (Figure 4.2d) of S-1 which actually shows that the AAO thickness is

$\approx 1 \mu\text{m}$. This means that since the length of the empty part of the pore is $\approx 140 \text{ nm}$ (see AR-XPS data), and the average length of the NWs/NTs is about 600 nm , the length of the Ag NRs (bottom part of the pores) would result $\approx 180 \text{ nm}$. In order to have a more precise estimation of the dimensions of the NWs/NTs and of the NRs, further experiments were accomplished. A fresh sample was functionalized with benzenethiol (BT) to prevent their aggregation in solution, etched in a NaOH 50 mM solution for 60 seconds and finally treated in an ultrasonic bath with pure ethanol for 30 minutes .

The UV-VIS spectrum of the Ag suspension in ethanol (**Figure 4.5a**) presents the typical absorption of Ag NSs with a large ($\approx 1:10$) aspect ratio.^{30,31} In Figure 4.5b the SEM image of the Ag NSs suspension deposited by drop-casting on $\text{SiO}_2/\text{Si}(100)$ is reported. The image clearly shows that the Ag NSs that form the bunches shown in Figure 4.2e, are actually Ag NTs with an average length of 730 nm .^{32, 33}

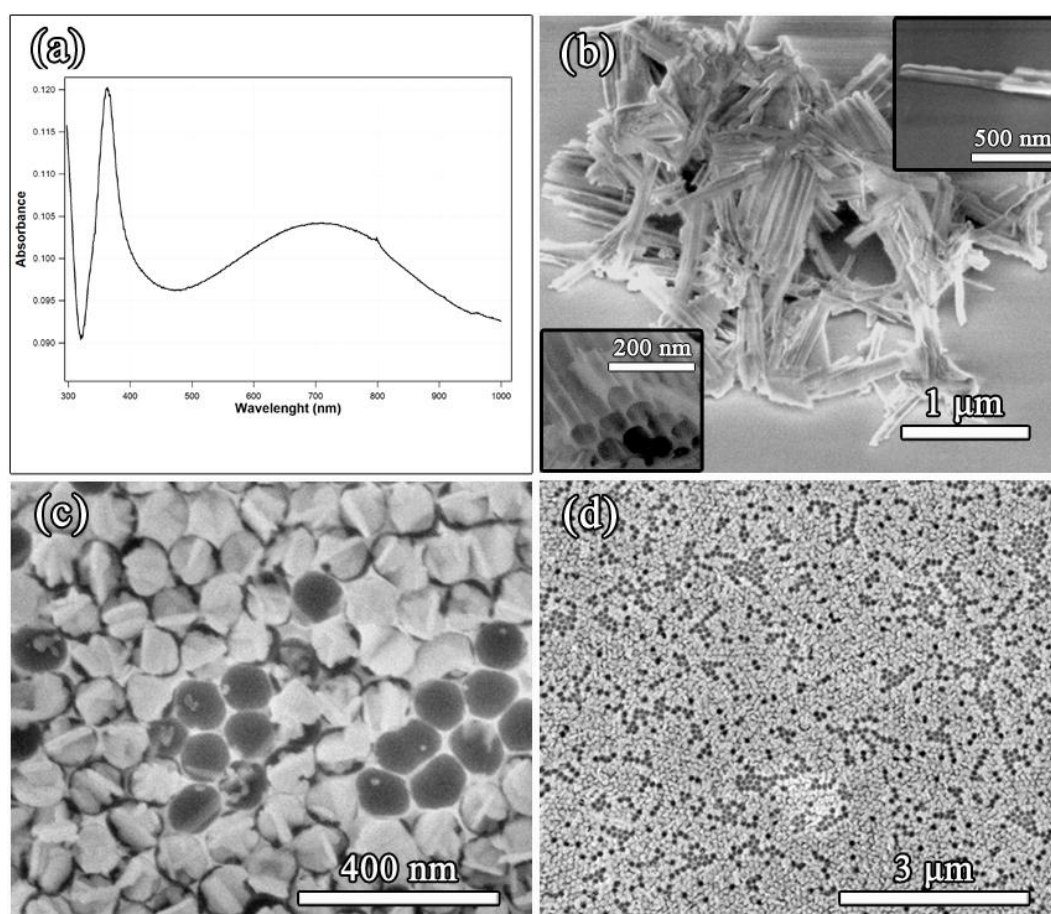


Figure 4.5 (a) UV-VIS spectrum of Ag NTs suspension in ethanol. (b) SEM image of Ag NTs obtained from drops of ethanol suspension and evaporation of the solvent on $\text{SiO}_2/\text{Si}(100)$. (c) small area and (d) large area SEM images of Ag NRs array after etching of S-1 in 50 mM NaOH solution for 60 s and sonication in ethanol for 30 min .

It is important to note that their length does not depend on the amount of charge used during the AC deposition and on the thickness of the AAO film. The inset on the top right corner of Figure 4.5b shows a single Ag NT, while in the bottom left corner the image shows an aggregate with several NTs. It is important to outline herein that by adopting the procedures based on the template approach described in this paper it is also possible to obtain a suspension of Ag NTs in alcohol in a very simple and reproducible way (NaOH etching + sonication) and this is particularly interesting also considering the fact that several samples can be etched in order to obtain more concentrated suspensions. These suspensions can eventually find application as indicator displacement assays (IDAs).³⁴

Figures 4.5c and d show two different magnifications of the Ag NRs that remain in the residue of the AAO matrix after NaOH etching and ultrasonic bath treatment of S-1. These Ag NRs with an irregularly shaped top form a perfectly ordered honeycomb structure with some vacancies (where the structures were washed away). The average height of these structures, as measured from the tilted image of the sample, is about 160 nm, a value that is not that far from the previous multi-technique (SEM/AR-XPS) evaluation.

4.3.3 Optical characterization of the Ag NSs arrays

In order to test the SERS properties of the array of NRs only, without any contribution from NWs/NTs, S-1 was first functionalized with BT and subsequently etched with NaOH and sonicated in ethanol. Notice that in this way only the NR tips are functionalized with BT and contribute to the SERS signal. The enhancement factor was measured at 10 different points on the sample providing an average value of $1.4 \cdot 10^4$. **Figure 4.6** gives an example of BT SERS spectrum. SERS enhancement factors (EFs) were evaluated following the procedure outlined by Le Ru,³⁵ adopting the following expression

$$EF = \frac{I_{SERS}^{BT}}{I_{liquid}^{BT}} \frac{C_{Vol}^{BT}}{C_{Surf}^{BT}} \frac{H_{eff}}{A} \quad (4.1)$$

where I_{SERS}^{BT} is the integrated intensity of the 999 cm^{-1} band of BT (β_{CCC}) absorbed on the metal surface and I_{liquid}^{BT} is the integrated intensity of the 1002 cm^{-1} band of liquid BT (β_{CCC}). The band assignment is shown in parenthesis: β indicates the in-plane bending and the Raman modes correspond to the so called *benzene ring breathing mode*.³⁶

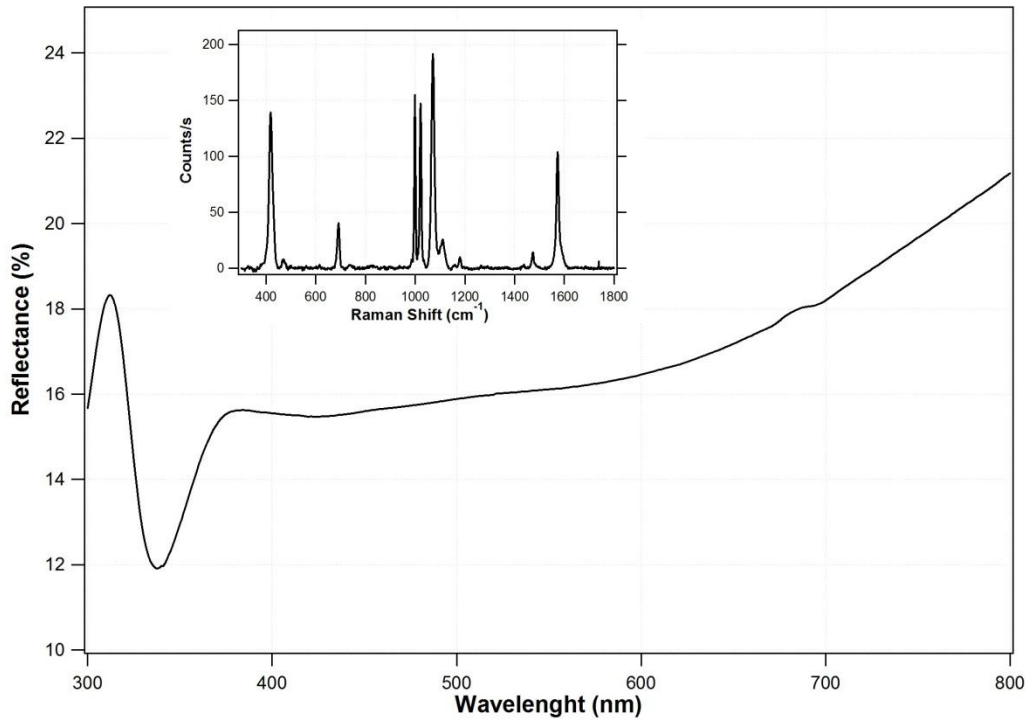


Figure 4.6 UV-VIS reflectance spectrum of Ag NRs array after sample (S-1) etching in 50 mM NaOH solution for 60 s and sonication in ethanol for 30 min; SERS spectrum reported in the inset.

C_{Surf}^{BT} is the surface packing density of BT on a flat silver surface, C_{Vol}^{BT} is the number of molecules per unit volume of liquid BT and H_{eff} is related to the axial collection efficiency of the experimental set-up. Finally the parameter “A” corresponds to the ratio between the number of molecules illuminated on the sample and on a flat surface within the same laser spot, assuming equal packing densities on both surfaces. Since the rod tips cover most of the area on top of the sample (see SEM images) we can approximately assume $A=1$ in equation 4.1. The reference (I_{liquid}^{BT}) was measured from BT sealed in a glass vial. H_{eff} was measured by the procedure in Ref. 35 and turned out to be around $74\text{ }\mu\text{m}$. The remaining parameters in equation 4.1 can be retrieved from the literature: $C_{Surf}^{BT} = 6.8 * 10^{14}\text{ molecules cm}^{-2}$,³⁷ (this value represents

the highest packing density in the literature and therefore provides a conservative estimation of the EF) and $C_{Vol}^{BT} = 5.88 \cdot 10^{21}$ molecules cm^{-3} .

In Figure 4.6 the UV-Vis spectrum acquired in diffuse reflectance mode of the sample used for the SERS measurements is reported. It shows very low reflectivity (the sample is black) and is rather flat in the 400-800 nm region. The dip in reflectance at about 340 nm is likely to be principally due to the plasma resonance of silver.³⁸

The possibility of using Silver nanostructures in AAO as a SPR sensor, has been tested on S-2. Diffuse reflectance spectra were monitored as a function of the variations in the surrounding refractive index: such variations were achieved by immersion of the samples in glycerol/water solutions (at several concentrations) for 5 minutes, followed by blowing with nitrogen.³⁹ Two different studies were carried out:

- one on S-2 etched in a 50 mM NaOH solution for 180 s
- one on S-2 as prepared

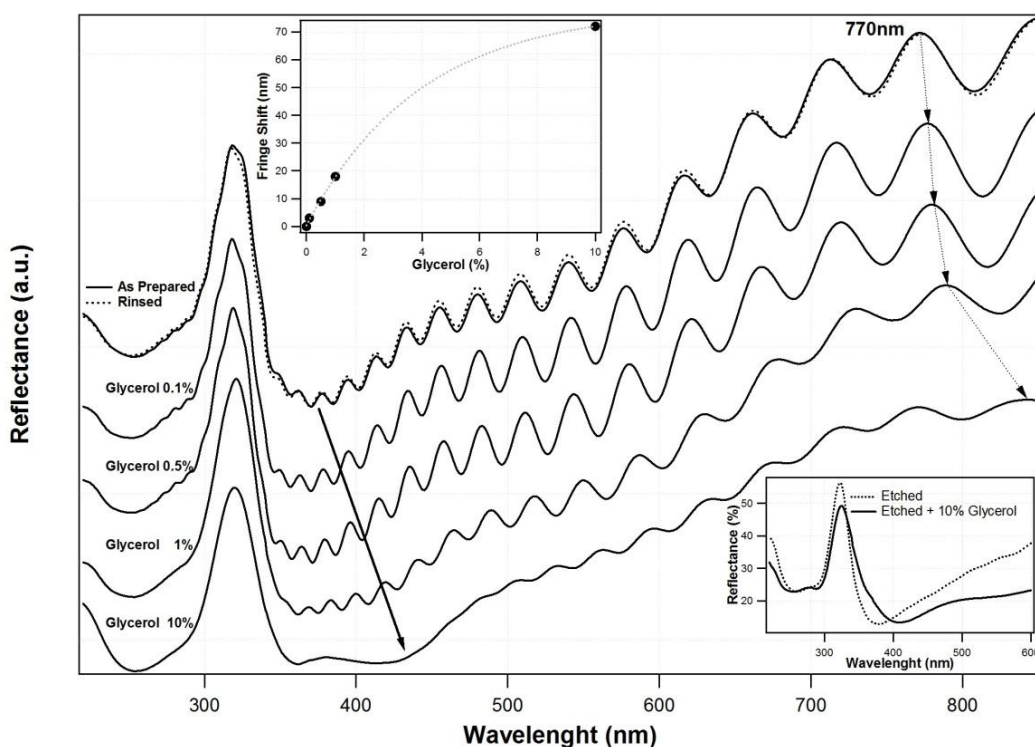


Figure 4.7 Reflectance spectra of S-2 after immersion in glycerol solutions of increasing concentration; for clarity an offset has been applied to the curves. The position of the fringe at 770 nm as function of glycerol concentration is reported in the upper-left inset. The inset in the bottom-right shows the shift of the Ag plasmon after immersion of an etched sample (50 mM NaOH solution for 180 s) in a 10% glycerol solution.

In the former case, the reflectance spectrum of the bare sample was compared to the spectrum obtained after treatment with a 10% solution of glycerol. In the latter, the spectrum of the bare sample was compared to the spectra achieved after treatment in glycerol solutions at 0.1, 0.5, 1, and 10% concentration. **Figure 4.7** recaps the results.

Concerning the experiment a) it is clear how the refractive index change induces a shift in the reflectance minimum from 380 nm to 410 nm. As for the experiment b), the reflectance spectra feature interference fringes due to the presence of the AAO layer. The shift of the reflectance minimum around 380 nm is harder to spot in this case due to the superposition with the fringes; on the other hand, a progressive shift in the maxima of the fringes is clearly evident. In Figure 4.7 it is reported the variation of the position of the interference fringe at 770 nm as function of the glycerol concentration. Both in experiment a) and b), the sensor behavior is highly reversible: after a simple rinse in water a spectrum identical to the one of the as prepared sample is recovered.

4.4 Discrete Dipole Approximation Study on Ag NRs

4.4.1 Discrete Dipole Approximation Model

In order to better understand the optical properties of the prepared Ag NRs arrays and to confirm the presence of “hot spots” due to the coupling effect of Ag NRs packed in a hexagonal array (see chapter 1, paragraph 1.8) a theoretical study based on Discrete Dipole Approximation (DDA) model was carried out[†]. It is important to point out that this theoretical approach is more accurate than that described in the Genov’s work.⁴⁰ In this paragraph it will be briefly reported how the model works and the obtained results.

[†] DDA calculations were performed by Assistant Professor Vincenzo Amendola of University of Padua

In the case of noble metal spherical nanoparticles, the extinction cross-section σ_{EXT} in the visible range can be accurately calculated by analytical expressions, using the Mie model.^{41,42} Even in case of spheroidal nanoparticles with size lower than about 15 nm, acceptable precision is achieved by other simple analytical expressions like the Gans model^{41,42}. Differently than in the case of the Mie model for spheres, however, the Gans model is not an exact solution of the electromagnetic problem of light interacting with spheroidal particles but is an approximated result valid in the quasistatic regime only^{41,42,43}. An explicit expression for the extinction cross-section is available also in case of cubic nanoparticles in the quasistatic regime, but it does not agree well with experimental results^{41,42}. No analytical expressions exist for the calculation of the σ_{EXT} of metal nanoparticles of lower symmetry. However, finite element methods are available that allow the calculation of the optical response of arbitrary geometries, with a precision dependent on the number of elements. The DDA is one of the most frequently used method to calculate the σ_{EXT} of metal particles of arbitrary shape and nanometric size⁴¹⁻⁵⁵. In DDA, one can account for the structure of interest, usually called “target,” by a cubic array of N polarizable points (i.e. N cubic dipoles). There are no restrictions about the complexity or the shape of the target. Basically, the polarization P_j induced on each point j of position r_j and polarizability α_j is given by:

$$\bar{P}_j = \alpha_j \bar{E}_{Loc}(\bar{r}_j) \quad (4.2)$$

where E_{Loc} is the electric field originated by the incident radiation that includes the contribution of all other dipoles:

$$\bar{E}_{Loc}(\bar{r}_j) = \bar{E}_0 \exp(i\bar{k} \cdot \bar{r}_j + i\omega t) - \sum_{l \neq j} \bar{\bar{A}}_{jl} \bar{P}_l \quad (4.3)$$

where $\bar{\bar{A}}_{jl}$ is the interaction matrix. The full expression of $\bar{\bar{A}}_{jl} \bar{P}_l$ is:

$$\bar{\bar{A}}_{jl} \bar{P}_l = \frac{\exp(ik\bar{r}_{jl})}{\bar{r}_{jl}^3} \times \left\{ k^2 \bar{r}_{jl} \times (\bar{r}_{jl} \times \bar{P}_l) + \frac{(1-ik\bar{r}_{jl})}{\bar{r}_{jl}^2} [\bar{r}_{jl}^2 \bar{P}_l - 3\bar{r}_{jl}(\bar{r}_{jl} \cdot \bar{P}_l)] \right\} \quad (4.4)$$

An important part of DDA is the use of an appropriate expression for α_i . The most applied expression was developed by Draine and Goodman as a correction of the Clausius–Mossotti polarizability by a series expansion of kd and ϵ_m , where d is the interdipole spacing. It allows the calculation of targets extinction spectra within $\sim 10\%$ of the exact result, independently of size, shape, and particle composition, provided that the number of dipoles N is large enough. In order to minimize the errors, the interdipole spacing d should be small compared to the distinctive structural features of the target. For instance, a sharp curvature cannot be well represented by a coarse cubic mesh; hence, a large number of dipoles are required for modeling rounded nanostructures as well as for nanoparticles having sharp edges, corners, or steps. For metal particles in the 2–200-nm-size range, an error smaller than 10% is usually achieved using N at least of the order of 10^4 and using interdipole spacing much smaller than the wavelengths of interest. For these calculations a free code named DDSCAT 6.0 was used. The code was developed by Draine and Flatau and adopts fast Fourier transform methods and complex conjugate gradient techniques to reduce the calculation time. Depending on the complexity of the target, N is set between 2×10^3 and 2×10^5 . These figures are comparable to or larger than the threshold of 10^4 dipoles, which is usually required to obtain an error of the order of 10% or less. If larger N is used for each nanoparticle, the computational time is increased as $N \log N$ but with negligible increases in the precision of the calculation.

4.4.2 Results of DDA calculation on Ag NRs Arrays

The target for DDA calculation (dipoles array) has been based on SEM morphological information. The Ag NRs array is the one reported in Figure 4.5c and d. A 6x6 Ag NRs Hexagonal array has been built by Matlab considering Ag NRs of 142 nm of height (27 dipoles), 75 nm of diameter (14 dipoles) embedded in 63 nm Al_2O_3 (12 dipoles), a Al_2O_3 barrier layer of 44 nm (8 dipoles) and a separation of 11 nm (2 dipoles) between each rod (see

Figure 4.8). All the calculation have been done using this target and polarized light.

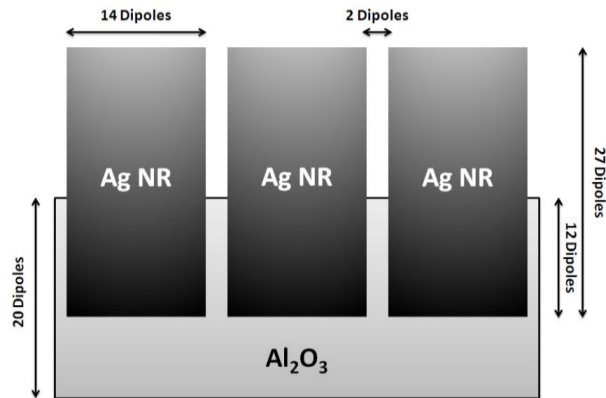


Figure 4.8 Sketch of a portion of the 6x6 Ag NRs target used for the DDA calculation

Preliminary DDA calculations (not reported) have shown that the largest local field enhancement (LFE) is obtained with a 633 nm laser source. The calculated LFE for the 6x6 target are reported in **Figure 4.9**.

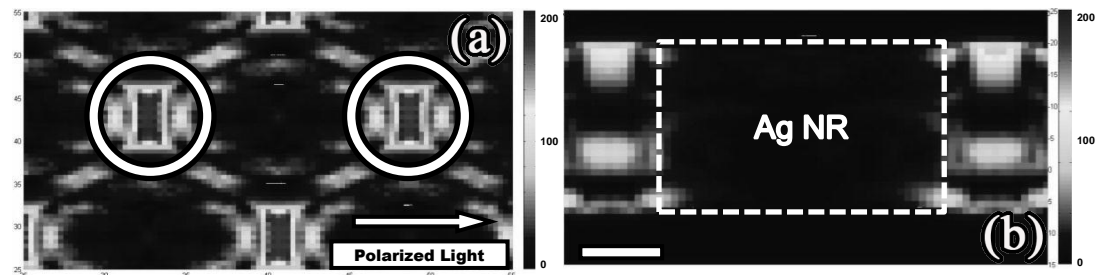


Figure 4.9 (a) Front view of the 6x6 Ag NRs array LFE. (b) Cross section of the 6x6 Ag NRs array LFE. Light polarization parallel with respect the Ag NRs array.

Figure 4.9 shows that the hot spots, with light polarization parallel to the Ag NRs array, are localized between the rods at 90° from each other.

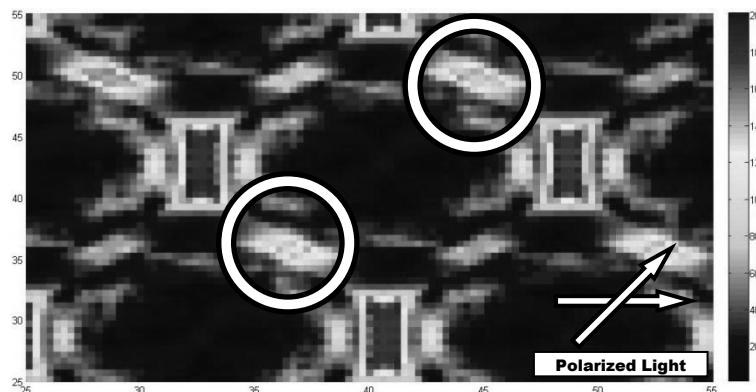


Figure 4.10 Front view of the 6x6 Ag NRs array LFE. Light polarization parallel and at 45° with respect the Ag NRs array.

The obtained results by considering also the contribution of polarized light at 45° with respect the parallel polarization are even more interesting. **Figure 4.10** clearly shows that with the double polarization two more hot spots per rod appear. When polarized light at 45° in the opposite direction is also added in the calculations, as shown in **Figure 4.11**, there is the appearance of two extra hot spots per rod.

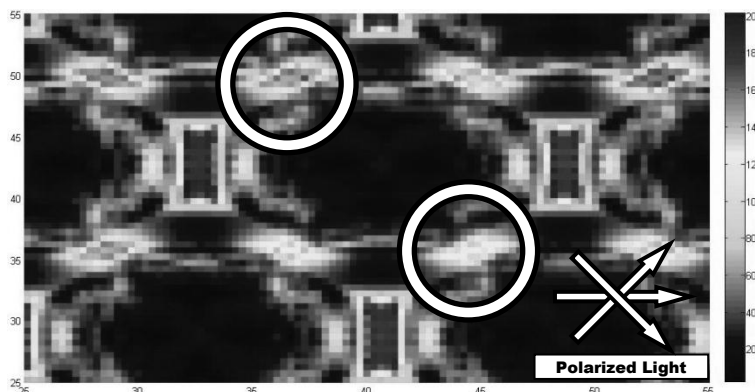


Figure 4.11 Front view of the 6x6 Ag NRs array LFE. Light polarization parallel and at 45° clockwise, and at 45° anticlockwise with respect the Ag NRs array.

The SERS EF from DDA calculations is in agreement with the experimental results reported in paragraph 4.3.3. In fact from DDA calculation, E^2 is $2 \cdot 10^2$ and since the EF is proportional to E^4 , the EF calculated is in the order of 10^4 which is in agreement with that measured from SERS spectra. This behavior indicates that the use of non-polarized radiation should lead to the formation of hot spots that surround the Ag NRs.

4.5 Ag@Cu Nanostructures grown into AAO

4.5.1 Experimental section

The AAO templates and the used AC electrodeposition procedure described in paragraph 4.2 can be easily used and adapted to deposit also other noble metals like Cu, Au etc. The attention was focused on Cu AC electrodeposition in order to have ordered Cu nanostructures (Cu NSs)

within the AAO. The idea is to use the Cu NSs as a sacrificial template to grow Ag in the pores by a simple redox reaction ($E^0_{\text{Cu}^{2+}/\text{Cu}} = 0.34 \text{ V}$, $E^0_{\text{Ag}^+/\text{Ag}} = 0.80 \text{ V}$). One might expect to simply “fill” the pores depositing Ag on the surface of the Cu NSs. This method can represent an easy way to grow noble metal nanostructures using Cu NSs as a building scaffold.

As for the Ag, the Cu electrodeposition was carried out in an EC reactor where the AAO electrode and a copper bar electrode were set as working and counter electrode, respectively. The AC signal, applied across the AAO layer electrode was generated using a TTI-TG230 arbitrary function generator and was amplified with an InterM-A120 amplifier to the desired voltage. The electrolyte was 10 mM $\text{Cu}(\text{NO}_3)_2$ + 0.5 M H_3BO_3 . Current density transients during the anodization and electrodeposition processes were monitored using a home-made LabView program that controls the EC set up, enabling current measurements while applying electrodeposition. After the deposition all samples were characterized by an intense yellow-green colour.

The sample, that will be called for simplicity “S-3”, was AC electrodeposited at 10 V, 170 Hz and with a total charge of 9 C. Also in this case the charge did not influence the pores filling. Then, the sample was dipped in a 50 mM NaOH solution for 10 seconds in order to etch part of the AAO template and to remove the CuO passivation layer that forms during the exposure to air. After NaOH etching the sample was rinsed with distilled water, dried in a stream of nitrogen and immediately dipped in a 0.1 M AgNO_3 solution for 30 minutes. After this step the sample was characterized by an intense deep violet colour.

The sample was finally rinsed with distilled water, blow dried with nitrogen and immediately functionalized in a 1 μM BT solution overnight for the SERS characterization.

4.5.2 Results and discussion

SEM images of the as-grown sample are reported in **Figure 4.12**. As in the case of silver AC electrodeposition it is easy to see that the pores are partially filled, although the pores appear to be filled with more compact Cu NSs. Also in this case, SEM images are slightly fuzzy due to the partial charging of the sample.

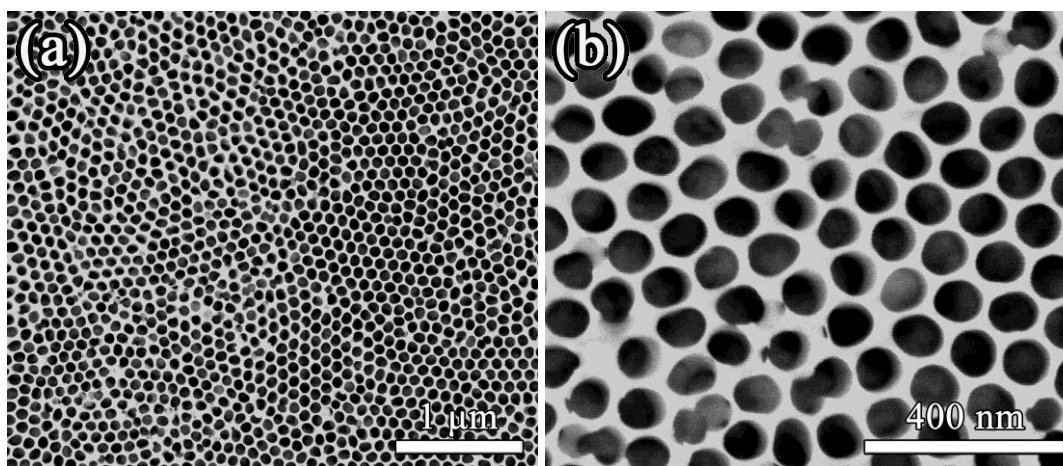


Figure 4.12 SEM images: (a) as prepared S-3, (b) detail of pores

The self-limited growth of the metal nanostructures inside the pores has been confirmed also in this case. The images show the formation of more compact structures (no NTs) and a higher pore filling. In some cases the formation of Cu dendritic structures on the surface depending on the parameters used during the AC growth was observed. Those samples have not been considered in the following discussion and the growth parameters have been optimized in order to avoid as much as possible the dendrites formation.

In **Figure 4.13** the Cu $2p_{3/2}$ XPS peak of the as-prepared S-3 is reported. Due to the insulating nature of the Al_2O_3 film that uniformly covers the Al sheet, in this case the peaks are rigidly shifted to a higher BE by 4.2 eV. The data reported in the figure have been recalibrated by taking the Al 2p peak as reference.

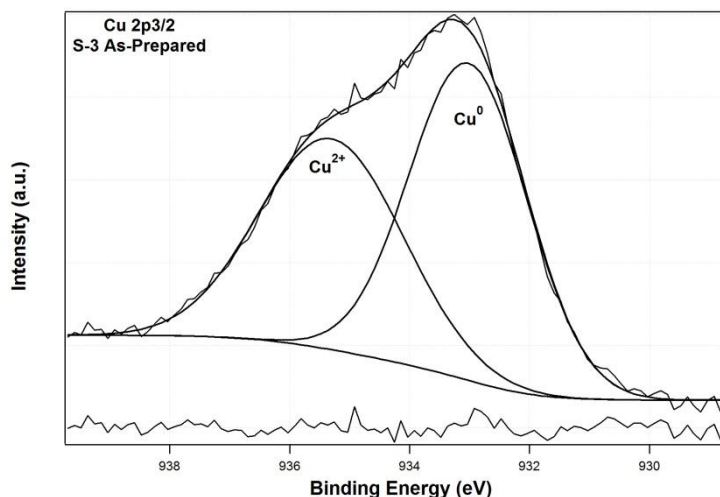


Figure 4.13 Cu 2p_{3/2} XPS spectrum of the as-prepared S-3

The two components of Cu XPS signal can be assigned (932.5 eV) to Metallic Cu, while the component at 934 eV can be assigned to the passivation layer of CuO that forms on the Cu NSs surface when the sample is air exposed. After NaOH treatment and the further treatment in the AgNO₃ solution (Ag@Cu S-3), in **Figure 4.14** it is possible to observe some brighter areas over the samples, due to the formation of “Ag caps”, over the Cu NSs, that occlude the pores.

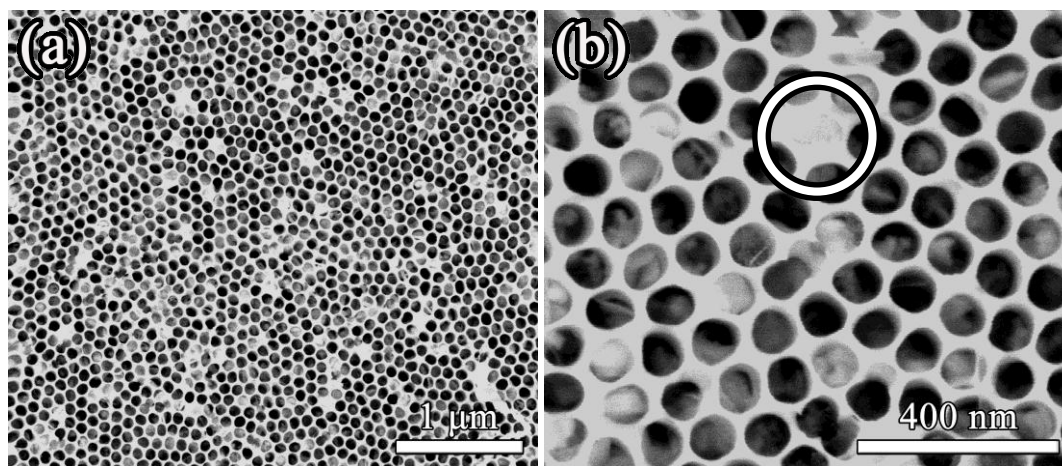


Figure 4.14 SEM images: (a) Ag@Cu S-3 NSs, (b) detail of pores and of an Ag caps

The Cu 2p_{3/2} XPS spectrum of S-3 after etching in NaOH and deeping in AgNO₃ solution (Ag@Cu S-3) is reported in **Figure 4.15** As one can see in Ag@Cu S-3 the component at 932.5 eV due to metallic Cu is less intense with respect the as-prepared S-3 (dotted line) because of Cu oxidation at the interface with Ag⁺ solution.

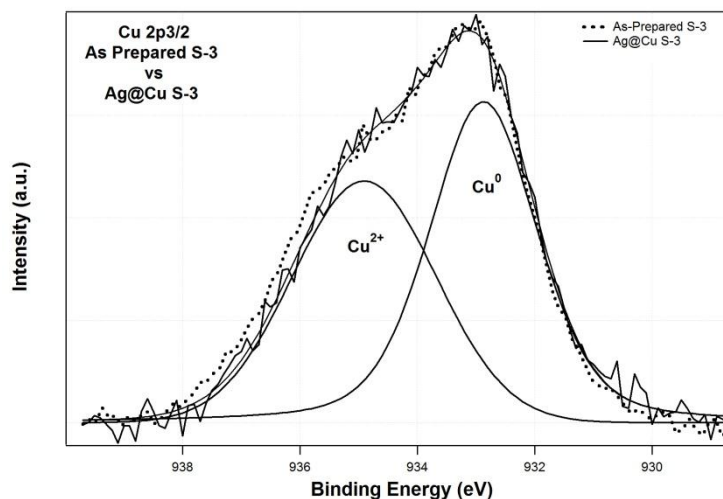


Figure 4.15 Cu 2p_{3/2} XPS spectrum of Ag@Cu S-3 vs as-prepared S-3

In the as-prepared S-3, in fact, the $\text{Cu}^0/\text{Cu}^{2+}$ peak area ratio, calculated on the normalized spectrum, is 1.23, while in the Ag@Cu S-3 it decreases to 1.15. The little decrease in the $\text{Cu}^0/\text{Cu}^{2+}$ ratio indicates that a very thin Ag layer forms on the Cu NSs. Thus, immediately after the formation of this “surface Ag layer” the reduction of Ag by Cu stops. It is important to remind that we do not expect the formation of AgCu alloy since it is known that the solubility of Cu in Ag is less than 1% at room temperature.⁵⁶ It is also reported that the effect of O_2 on an Ag monolayer, deposited on Cu, is the oxidation of Cu that slowly diffuses on the surface.⁵⁷ So in this case we expect an “anodic” protection of the Ag layer from oxidation.

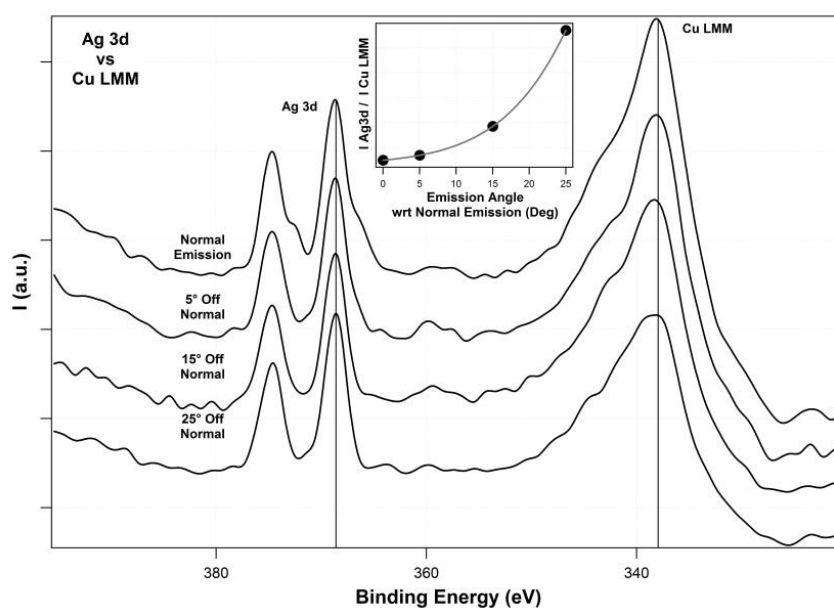


Figure 4.16 Ag 3d Ar-XPS spectrum of Ag@Cu S-3

In **Figure 4.16**, as in the case of Cu 2p signal, no shadowing effect in the Ag 3d AR-XPS spectra is observed, and this feature is in agreement with SEM images that show the Ag caps on top of the sample. The inset in Figure 4.16 shows how the ratio between the intensity of Ag 3d peak and that of Cu LMM of signal increases when one moves away from the normal emission, thus indicating a segregation of Ag on top of the Cu NSs

Finally, after functionalization with BT, the SERS properties of the sample were tested following the standard procedures and the EF, evaluated by the Le Ru procedure, is about $1 \cdot 10^4$ with a good homogeneity.

4.6 Conclusions

It was demonstrated that by using *connected* AAO membranes, easy to prepare and to handle, and a cheap AC electrodeposition procedure (not requiring neither specialistic equipments nor expertise) it is possible to obtain a large variety of Ag NSs, either in suspension (after a sonication of the samples) or attached to a substrate. In particular, the different NSs obtained depend on the AAO thickness and on the actual parameters adopted in the AC electrodeposition.

In the case of lower thickness sample S-1, the Ag NSs contained at the bottom of the AAO pores are compact Ag NRs with an average height of about 160 nm and a diameter of 75-80 nm. The upper part of the pores is filled with Ag NTs characterized by an average length of 730 nm. The AAO pores are not completely filled by the Ag NSs as clearly shown by the AR-XPS measurements and the average height of the NSs does not depend on the amount of charge passed during the AC deposition, but only on the AC deposition parameters. This is the first time that a direct evidence of a self-limited growth is put forward. A simple NaOH etching treatment of S-1 allows to obtain a partially ordered surface of Ag NSs where bunches of collapsed Ag nanotubes cover Ag NRs that fill the bottom part of the AAO channels. It is possible to obtain a perfectly ordered array of Ag NRs, eliminating the Ag NTs, by a simple ultrasonic bath treatment in ethanol of the etched sample.

The ethanol suspension containing the Ag NTs can be concentrated and used for other applications.

In the case of S-2 the bottom of the pores is filled with spheroidal Ag particle with an average diameter of about 60 nm, while the upper part of the pores is filled with Ag NWs. The same NaOH treatment leads to the obtainment of a hank of Ag NWs where Ag spheroidal particles are held within the NWs, probably by electrostatic interaction.

Moreover, the optical properties of S-1 and S-2 are very different: It was demonstrated that S-1 can be effectively used as SERS substrate, while S-2 can be used in LSPR sensing.

The preliminary DDA simulations have shown that the theoretical EF value is in agreement with the experimental one. Furthermore it has been demonstrated that with a non-polarized light it is possible to have a bigger enhancement because of the formation of a greater number of hot spots in the gap zones of the Ag NRs array.

Finally the versatility of the prepared *connected* AAO membranes and of the used AC electrodeposition procedure by growing Cu NSs into the AAO nanopores was shown. These structures could be used as prepared, but in this case, they were used as a scaffold (sacrificial anode) for the Ag growth in order to obtain a substrate suitable for SERS measurements.

References

- 1 H. Gao, W. Zhou, T.W. Odom, *Adv. Funct. Mater.*, **2010**, 20 , 529
 - 2 J. Weber, R. Singhal, S. Zekri and A. Kumar, *International Materials Reviews*, **2008**, 53, 235
 - 3 M. E. Stewart , C. R. Anderton , L. B. Thompson , J. Maria , S. K. Gray , J. A. Rogers , R. G. Nuzzo , *Chem. Rev.*, **2008** , 108 , 494
 - 4 G. Hong, C. Li, and L. Qi, *Adv. Funct. Mater.*, **2010**, 20, 3774
 - 5 M.R. Jones, K.D. Osberg, R.J. Macfarlane, M.R. Langille, C. A. Mirkin, *Chem. Rev.*, **2011**, 111, 3736 and references therein
 - 6 Y. Lei, W. Cai, G. Wilde, *Prog. In Mat. Sci.*, **2007**, **52**, 465
 - 7 A. Huczko, *Appl. Phys. A*, **2000**, 70, 365
 - 8 M. Rycenga, C.M. Cobley, J. Zeng, W. Li, C.H. Moran, Q. Zhang, D. Qin, Y. Xia, *Chem. Rev.*, **2011**, 111 3669
 - 9 Y. Joo, J. S. Suh, *Bull. Korean Chem. Soc.*, **1995**, 16, 808
 - 10 X. Zhang, J. Zhao, A. V. Whitney, J. W. Elam and R. P. Van Duyne, *J. Am. Chem. Soc.*, **2006**, 128, 10304
 - 11 L. Qin, M. J. Banholzer, J. E. Millstone and C. A. Mirkin, *Nano Lett.*, **2007**, 7, 3839
 - 12 D. P. Fromm, A. Sundaramurthy, A. Kinkhabwala, P. J. Schuck, F. S. Kino and W. E. Moerner, *J. Chem. Phys.*, **2006**, 124, 061101
 - 13 R. Alvarez-Puebla, B. Cui, J.-P. Bravo-Vasquez, T. Veres and H. Fenniri, *J. Phys. Chem. C*, **2007**, 111, 6720
 - 14 R. J. C. Brown and M. J. Milton, *J. Raman. Spectrosc.*, **2008**, 39, 1313
 - 15 See for example: G.H. Gu, J.S. Suh, *J. Raman Spectrosc.*, **2010**, 41, 624
 - 16 N. Ji, W. Ruan, C. Wang, Z. Lu, B. Zhao, *Langmuir*, **2009**, 25, 11869
 - 17 H.F. Liu, E.S. Lim, P.K.H. Tung, N. Xiang, *Thin Solid Films*, **2011**, 519, 3050
 - 18 S.J. Lee, A.R. Morril, M. Moskovits, *J. Am. Chem. Soc.*, **2006**, 128, 2200
 - 19 G. H. Gu, J.S. Suh, *Langmuir*, **2008**, 24, 8934
-

-
- 20 T. Sannomya, P.K. Sahoo, D.I. Mahcicek, H.H. Solak, C. Hafner, D. Grieshaber, and J. Vörös, *Small*, **2009**, 5 1889
- 21 A. Eftekhari in *Nanostructured Materials in Electrochemistry.*, WILEY-VCH, Weinheim, Germany, **2008**
- 22 H. Masuda and M. Satoh, *Jpn. J. Appl. Phys., Part 2* **1996**, 35, L126
- 23 A. Rauf, M. Mehmood, M.A. Rasheed, M. Aslam, *J Solid State Electrochem*, **2009**, 13, 321
- 24 A. Zaban, A. Meier, B.A. Gregg, *J. Phys. Chem. B*, **1997**, 101, 7985
- 25 D. Routkevitch, J. Chan, J.M. Xu, M. Moskovits, *Electrochem. Soc. Proc. Ser.*, **1997**, 97
- 26 S.J. Kawai, *Electrochem. Soc.*, **1975**, 122, 1026
- 27 N.J. Gerein, J.A. Haber, *J. Phys. Chem. B*, **2005**, 109, 17372
- 28 K. Nielsch, F. Müller, A.P. Li, U. Gösele, *Adv. Mater.*, **2000**, 12, 582
- 29 E. Budevski, G. Staikov, W. J Lorenz, *Electrochim. Acta*, **2000**, 45, 2559
- 30 A.L. Schmucker, N. Harris, M.J. Banholzer, M.G. Blaber, K. D. Osberg, G.C. Schatz, C.A. Mirkin *ACS Nano*, **2010**, 4, 5453
- 31 P. Sarkar, D.K. Bhui, H. Bar, G.P. Sahoo, S. Samanta, S. Pyne, A. Misra, *Nanoscal. Res. Lett.*, **2010**, 5, 1611
- 32 S-H. Zhang, Z-X. Xie, Z-Y. Jiang, X. Xu, J. Xiang, R-B. Huang, L-S. Zheng, *Chem. Commun.*, **2004**, 1106
- 33 W. Lee, R. Scholz, K. Nielsch, U. Gösele, *Angew. Chem. Int. Ed.*, **2005**, 44, 6050
- 34 U. H. F. Bunz and V. M. Rotello, *Angew. Chem. Int. Ed.*, **2010**, 49, 3268
- 35 E.C. Le Ru, C. Galloway and P.G. Etchegoin, *Phys. Chem. Chem. Phys.*, **2006**, 8, 3083
- 36 R. L. Aggarwal, L. W. Farrar, E. D. Diebold and D. L. Pollac, *J. Raman Spectrosc.*, **2009**, 40, 1331
- 37 C.L. Haynes and R.P. Van Duyne, *J. Phys. Chem. B*, **2003**, 107, 7426
- 38 H. Ehrenreich and H.R. Philipp, *Phys. Rev.*, **1962**, 128 (4), 1622
- 39 S-H. Yeom, O-G. Kim, B-H. Kang, K-J. Kim, H. Yuang, D-H. Kwon, H-R Kim, S-W. Kang, *Opt. Express*, **2011**, 19, 22882
-

-
- 40 D. A. Genov, A. K. Sarychev, V. M. Shalaev and A. Wei, *Nano Lett.* **2004**, 4, 153
- 41 C. Noguez, *J. Phys. Chem. C*, **2007**, 111, 3806
- 42 U. Kreibig, M. Vollmer, *Optical properties of metal clusters*, Springer, Berlin, **1995**
- 43 A. L. Gonzalez and C. Noguez, *J. Comput. Theor. Nanosci.* **2007**, 4, 231
- 44 J. Ren, R.D. Tilley, *J Am Chem Soc*, **2007**, 129, 3287
- 45 B. J. Wiley, S. H. Im, Z.Y. Li, J. McLellan, A. Siekkinen, Y. Xia, *J. Phys. Chem. B*, **2006**, 110, 15666
- 46 C. Noguez, *Opt Mater*, **2005**, 27, 1204
- 47 A. L. Gonzalez, C. Noguez, G. P. Ortiz, G. Rodriguez-Gattorno, *J. Phys. Chem. B*, **2005**, 109, 17512
- 48 K.L. Kelly, E. Coronado, L.L. Zhao, G. C. Schatz, *J. Phys. Chem. B*, **2003**, 107, 668
- 49 A. L. Gonzalez, J. A. Reyes-Esqueda, C. Noguez, *J. Phys. Chem. C*, **2008**, 112, 7356
- 50 M. A. Gracia-Pinilla, E. Perez-Tijerina, J. A. Garcia, C. Fernandez-Navarro, A. Tlahuice-Flores, S. Mejia-Rosales, J. M. Montejano-Carrizales, M. Jose-Yacaman, *J. Phys. Chem. C*, **2008**, 112, 13492
- 51 H. Portales, N. Pinna, M. P. Pileni, *J. Phys. Chem. A*, **2009**, 113, 4094
- 52 C. E. Roman-Velazquez, C. Noguez, J. Z. Zhang, *J. Phys. Chem. A*, **2009**, 113, 4068
- 53 I. Sosa, C. Noguez, R. G. Barrera, *J. Phys. Chem. B*, **2003**, 107, 6269
- 54 J.Z. Zhang, C. Noguez, *Plasmonics*, **2008**, 3, 127
- 55 D. T. Draine, P. J. Flatau, *J. Opt. Soc. Am. A*, **1994**, 11, 1491
- 56 P. Lejcek, J. Kovac, J. Vanickova, J. Ded, Z. Samardzija and A. Zalar, *Surf. Interface Anal.* **2010**, 42, 662
- 57 M. Lampimaki, K. Lahtonen, M. Hirsimaki and M. Valden, *Surf. Interface Anal.* **2007**, 39, 359
-

Chapter 5

“Green Synthesis” and electrophoretic deposition of Ag nanoparticle on SiO₂/Si(100)*

5.1 Introduction

Over the past decades there has been an increasing emphasis on the topic of “green” chemistry and chemical processes. The goal is the total elimination or at least minimization of generated waste. The preparation of nanoparticles generally involves the reduction of metal ions in solution or in high temperature gaseous environment. The reducing agents commonly used in the synthesis are dimethyl formamide¹, hydrazine², and formaldehyde³. Alternatively, one can consider as “green” methods every procedure that does not require the use of solvents and generally chemicals. In this case, metal nanoparticles can be prepared through physical methods like sputtering, evaporation, laser ablation etc. The disadvantage is the obvious need to use expensive instrumentation, to operate, in some cases, in high vacuum environment and therefore an intrinsic difficulty to transfer the process to industrial applications. In many cases physical methods allow to produce metal nanoparticles and to easily support them on proper substrates, something that cannot be always easily obtained by a classic chemical approach. The goal of this thesis is the preparation of Ag nanoparticles to be used in SERS substrates or LSPR sensing in a cheap and easy way. In this case, the reduction of Ag⁺ by D-glucose satisfies both aspects: the “green chemistry” approach and the cheap and easy

* Manuscript under preparation

requirements. It is also clear that the possibility to support these nanoparticle on suitable substrates, maintaining at the same time their dimensions, by using a “green” chemical approach is not immediately obvious. The electrophoretic deposition⁴ (EPD) should in this case be an easy and cheap way to support the prepared metal NPs on a substrate and at the same time it is also compatible with “green” requirements. In fact, the EPD as a material processing technique has attracted some attention because of its low cost, versatile property and simple equipment.

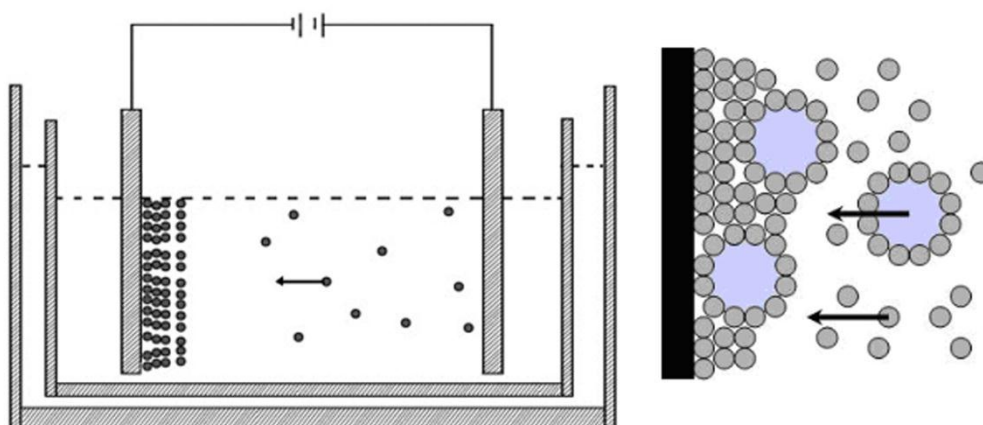


Figure 5.1 Schematic illustration of Electrophoretic Deposition

EPD is usually carried out in a two-electrode cell with colloidal solution as schematically shown in **Figure 5.1**. We can divide the process in two steps: first, charged colloidal particles suspended in a suitable solution move towards the oppositely charged electrodes under an applied electric field; afterwards, the colloidal particles accumulate on the electrode and produce a compact and homogeneous film. The method was initially used for processing oxide nanoparticles and depositing various coatings (TiO_2 , ZnO etc.) on substrate with various shapes and porous structures. However, EPD is seldom used for the fabrication of noble metal film structures. It also known that particles, in films prepared by EPD, are usually similar in size and shape to those in the colloidal solution. Therefore, it is reasonable to expect that similar optical properties, to the ones shown in solution, be maintained once the particles are supported on a substrate.

5.2 Experimental Section

The silver nanoparticles (Ag NPs) colloidal solution are synthesized by a modified “Tollens’ test method”. Tollens’ reactant is prepared adding concentrated ammonium hydroxide dropwise to 10 mL of 0.1 M silver nitrate solution until the initial precipitate is dissolved. Then 5 mL of 0.8 M NaOH solution are added; until a dark precipitate (AgOH) is formed. Finally, more ammonium hydroxide is added dropwise until a clear solution is obtained.

150 μ L of Tollens’ reactant solution are added to 80 mL of a 0.25 M glucose solution in a 100 mL pirex beaker. Then, the solution is rapidly heated, under vigorous stirring, on a hotplate until a bright yellow solution is obtained (Ag NPs formation at ~ 40 °C). The reaction goes to completion very quickly. When the temperature reaches 45°C the solution is quickly cooled in a water bath to room temperature.

The zeta potential of the Ag NPs was measured by a Zetasizer (Nano-ZS) from Malvern Instruments.

UV–VIS spectra were recorded with a Varian Cary 5 spectrometer in 1 cm optical path polystyrene cells.

Transmission Electron Microscopy (TEM) images were carried out with a JEOL 200CX microscope, working at 200 kV. The sample for TEM analysis was drop casted onto a copper grid, allowed to dry overnight in a ventilated oven.

The Ag NPs electrophoretic deposition (EPD) was carried out at a constant current density of 1 mA/cm² in a 10 mL pirex beaker under gentle stirring. Two cleaned 1cm x1.5 cm Si(100) wafer were set as working and counter electrode (see Figure 5.1). The distance between the two electrodes was set at 50 mm. After EPD, the deposited samples were rinsed gently with deionized water and then dried by nitrogen.

The chemical characterization of the deposited samples surface was obtained by XPS using a VG ESCALAB MK II (Vacuum Generators, Hastings, England) system (base pressure of 1×10^{-7} Pa) equipped with a

twin anode (Mg/Al) X-ray source with a hemispherical electrostatic analyzer and a five-channeltron detector. All the spectra reported were collected using Mg K_{α} excitation energy. The peak intensities were determined after a linear background subtraction. The binding energy (BE) scale was calibrated with respect to Pt 4f $_{7/2}$ (71.0 eV) measured on an Pt(111) single crystal.

SEM investigations were performed with a dual beam FEI Nova 600i instrument, with a semi-in-lens cold cathode field emission scanning electron microscope source. The micrographs were taken at 5 kV accelerating voltage, using in-lens detector in pure secondary electron signal mode. FIB cross section was performed by means of the ion source of the dual beam system using 30KeV of accelerating voltage.

SERS measurements were recorded by using a micro-Raman setup. A diode laser working at 785 nm (XTRA, Toptica Photonics AG) was used as excitation light source. The laser beam was coupled to a microscope (Olympus BX 40) and focused on the sample by a 20x objective (Olympus SLMPL, NA=0.35). Back-scattered Raman signal was separated from the Rayleigh scattering by an edge filter, analyzed with a 320 mm focal length imaging spectrograph (TRIAX-320 ISA) and a liquid nitrogen cooled CCD camera (Spectrum One, Jobin Yvon). The typical spot diameter at the focus was about 3 μm .

Diffuse reflectance measurements were recorded on a Jasco V-570 spectrophotometer equipped with a Jasco ISN-470 integrating-sphere apparatus. The studied wavelength range was 200–800 nm.

All spectra were measured with a FT-IR JASCO 4100 spectrometer and recorded at 4 cm^{-1} resolution and 32 scans in the infrared region from 4000 to 400 cm^{-1} .

5.3 Results and Discussion

5.3.1 Optical and Morphological characterization of as-prepared Ag NPs colloidal suspension

There are many examples of colloidal synthesis of Ag NPs obtained by reduction of a silver precursor with reducing agents (sodium borohydride, formaldehyde, etc) and stabilized using chemical agents⁵ that prevent the aggregation (organic acids, polar polymers, etc). In all cases, stabilizers are added, during or after the reaction, in order to maintain the Ag NPs in suspension and to avoid aggregation and precipitation phenomena.

In this synthesis the Ag NPs are obtained using $[\text{Ag}(\text{NH}_3)_2]^+$ as silver precursor and glucose as reducing agent. No stabilizer is added because, the gluconic acid that is formed after the oxidation of glucose, possibly acts as a stabilizer as shown in the following paragraph.

Khan described one of the most recent examples of “green synthesis”⁶. In his work the preparation of single-crystalline Ag NPs was performed by the reduction of $[\text{Ag}(\text{NH}_3)_2]^+$ with glucose at room temperature in the presence of cetyltrimethylammonium bromide (CTAB). CTAB plays different roles during the redox process, solubilizing the reactants, controlling the nucleation and/or growth of nanoparticles, thus stabilizing the Ag NPs. On the other hand, totally “green synthesis” are possible. CTAB or other chemical stabilizers can be replaced by natural ones. In his communication Raveendran⁷ describes a completely "green" synthetic method to produce silver nanoparticles. The suggested process is simple, environmentally benign, and quite efficient. Gentle heating an aqueous starch solution containing silver nitrate and glucose, relatively mono-disperse, leads to a Ag NPs suspension. In this case Beta-d-Glucose serves as the green reducing agent, while starch serves as the stabilization agent.

The reaction parameters of the synthesis were optimized by changing the glucose concentration, and maintaining constant the amount of $[\text{Ag}(\text{NH}_3)_2]^+$ ($\sim 10^{-4}$ M), in order to have a sharp plasmonic absorption (≈ 400 nm) and a stable Ag NPs suspension. In **Figure 5.2** the UV-VIS spectra of the as-prepared Ag NPs suspensions at various glucose concentration are reported. As it is possible to observe, the solution with the sharpest plasmonic peak, at 400 nm, was obtained from a of 0.25 M D-Glucose solution. The full width at half maximum (FWHM) of the 0.25 M solution is the lowest of the four analyzed samples and this is an indication of a good monodispersion of the Ag NPs. When a higher glucose concentration is used, one can observe a larger peak that can be fitted with two plasmonic components at 400 nm (compatible with 25 nm Ag NPs) and 450 nm (compatible with about 80 nm Ag NPs) probably due to a bimodal dispersion of Ag NPs.

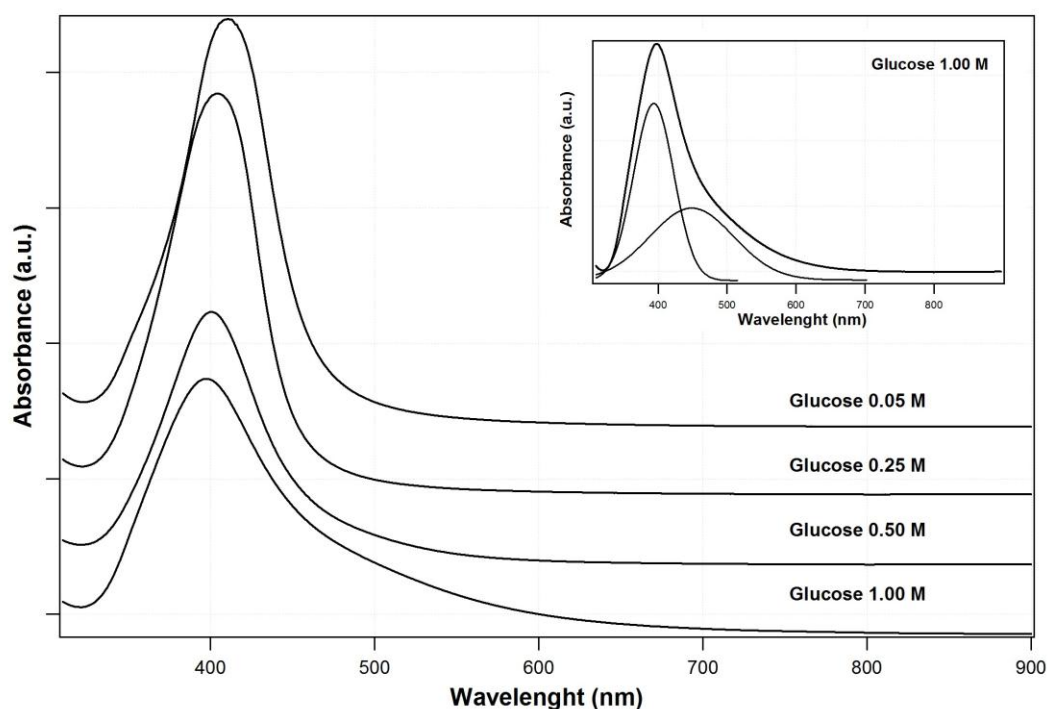


Figure 5.2 UV-VIS spectra at variable glucose concentration

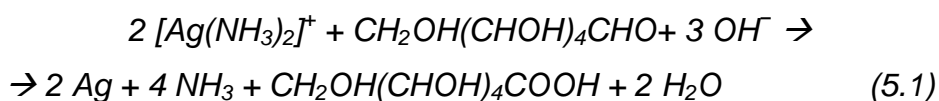
The four samples were allowed to age for a week. After this aging time, aggregation phenomena occurred in all suspensions, excluding the 0.25 molar one.

I have also explored the effect of $[\text{Ag}(\text{NH}_3)_2]^+$ concentration with the aim of increasing the Ag NPs concentration by using 4 different $[\text{Ag}(\text{NH}_3)_2]^+$ concentration: $2 \cdot 10^{-4}$, $4 \cdot 10^{-4}$, $8 \cdot 10^{-4}$ and $1 \cdot 10^{-3}$ M. Also in this case the

solutions were aged, but after just one day, aggregation phenomena occurred. It is clear that $1 \cdot 10^{-4}$ M is the critical $[\text{Ag}(\text{NH}_3)_2]^+$ concentration, beyond which the particles are no longer stable.

An $[\text{Ag}(\text{NH}_3)_2]^+$ concentration of $1 \cdot 10^{-4}$ M and a glucose concentration of 0.25 M lead to the best results, therefore these parameters have been used also to perform the EPD experiments.

The stability of the Ag NPs, obtained in this simple way, is probably due to the formation of gluconic acid micelles forming on the Ag NPs surface⁸. Gluconic acid forms during the reduction of $[\text{Ag}(\text{NH}_3)_2]^+$:



It is thus clear that the right ratio between the amount of the silver precursor and glucose is fundamental to keep the colloidal suspension stable. Glucose in this case is, at the same time, the reducing agent and leads to the formation of gluconic acid (see reaction 5.1), that stabilizes the AgNPs. The formation of gluconic acid is also indicated by a lower value of pH after the reaction has occurred.

Kvítek et. al.⁹ give a very detailed description of the reduction process of $[\text{Ag}(\text{NH}_3)_2]^+$ solutions with several reducing sugars like xylose, glucose, fructose and maltose. In his experiments the initial concentrations of the reaction mixture components were 10^{-3} M for AgNO_3 and 0.01 M for the reducing sugar. The reduction proceeds via an autocatalytic mechanism as manifested by the characteristic sigmoid shape of the corresponding kinetic curves (see **Figure 5.3**). They also found that the reaction rate is strongly dependent on the ammonia concentration. Higher reaction rates are measured with lower ammonia concentrations. They obtained spherical particles with their average size (diameter) dependent on the ammonia concentration and on the reducing sugar. In particular, when glucose was used, the Ag NPs were characterized by an average diameter of 57 nm by using an ammonia concentration of 0.005 M/L, while higher diameters were obtained with higher ammonia concentrations. The UV-Vis spectra were characterized by a sharp maximum at 420 nm, while flat maxima in the range

400-500 nm were observed with higher ammonia concentrations.

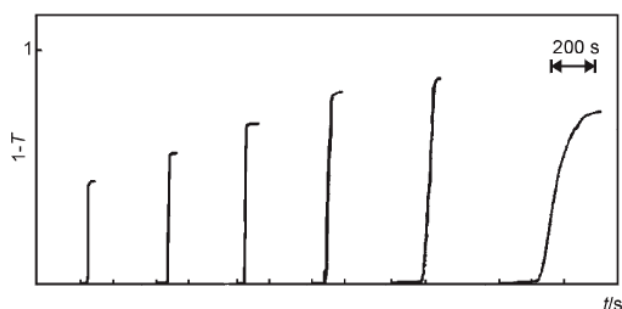


Figure 5.3 Kinetic curves of silver colloid formation recorded as change of transparency T during the $[\text{Ag}(\text{NH}_3)_2]^+$ reduction by glucose for the ammonia concentrations in the reaction system: 0.005, 0.01, 0.02, 0.05, 0.1 and 0.2 M (from the left).⁹

The classical theory of new phase formation and growth is applicable in order to explain the lower particles dimensions, obtained in this case, characterized by a rather sharp distribution. This model is applicable if a weak reducing agent is used rather than an aggregation mechanism, more appropriate for the reduction of Ag ions by strong reducing agents (NaBH_4). Following the theory of formation and growth of a new phase, a nucleus can be formed only under suitable thermodynamic conditions, characterized by an over-saturation quantity, on which the frequency of new phase nuclei formation is dependent. Those nuclei reaching the critical dimensions can grow in further reaction stages to give final stable particles. In this stage, the silver formed by the reduction is preferentially deposited on already-existing nuclei, since a heterogeneous mechanism of nucleation is energetically more favourable than a homogeneous one. Regarding the easier deposition of silver onto the already formed silver particles, the abrupt decrease occurs in over-saturation conditions. The formation of further nuclei by the homogeneous mechanism is then suppressed. At a higher reduction rate, given mainly by the high difference in the redox potentials of Ag^+/Ag and the reducing agent, a higher degree of over-saturation and a higher frequency of nuclei formation are achieved at the beginning of the reduction process. Therefore, more critical nuclei are formed in the reaction system. The more nuclei that are formed in the initial stage, the smaller the resulting particles are. This is because a given amount of silver is consumed by a larger number of nuclei.

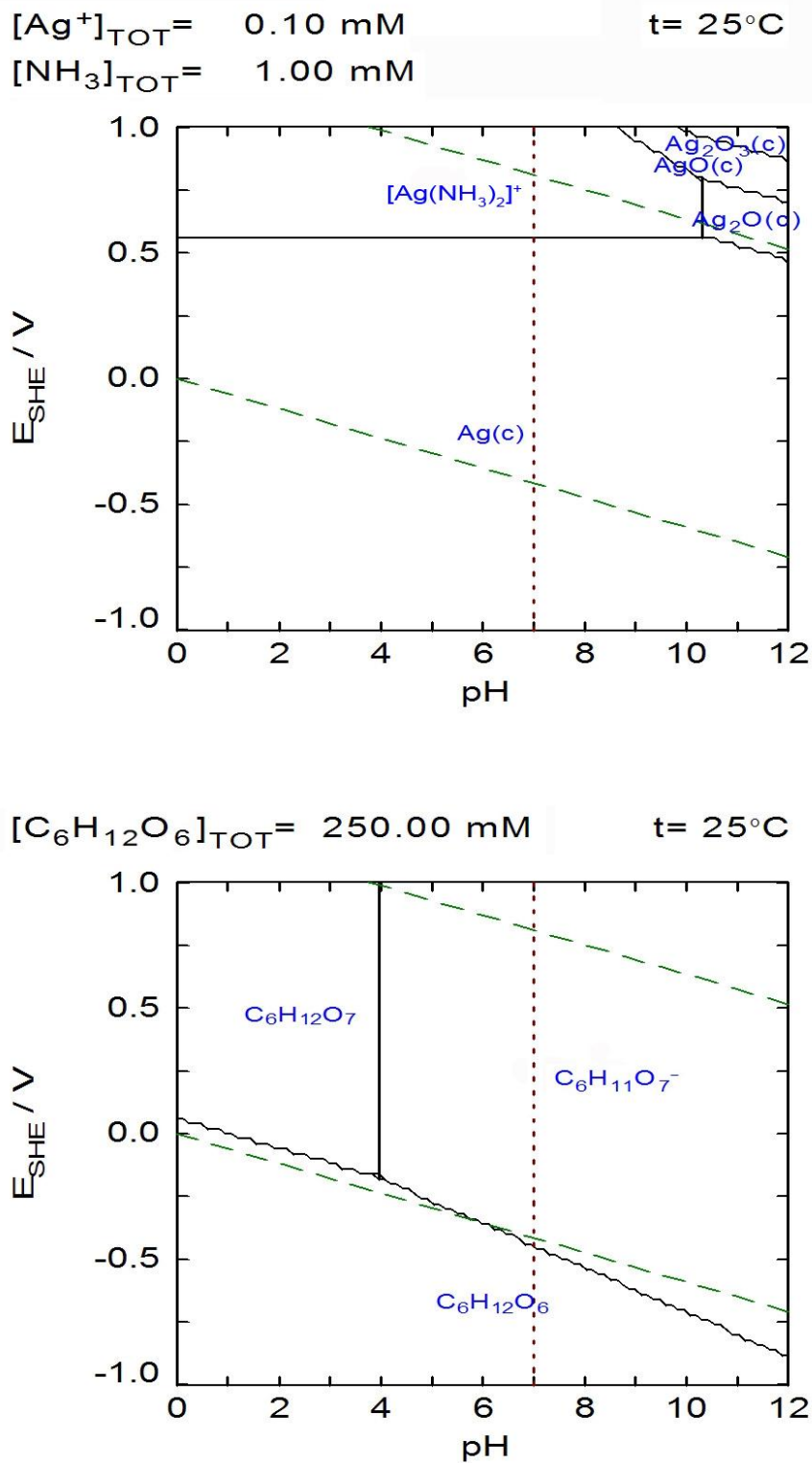


Figure 5.4 Pourbaix diagrams of Ag precursor and gluconic acid

From the Pourbaix diagrams in **Figure 5.4** it is possible to observe that a basic pH is required in order to have a good stability of the Ag precursor in solution and to decrease the reduction potential of the Gluconic Acid/Glucose couple. It is also clear that with a pH higher than 10, Ag_2O precipitates.

Thus, it is clear that in this case, the use of a rather low ammonia concentration ($1 \cdot 10^{-3}$ M) (higher Ag^+/Ag reduction potential) and the high value of pH, obtained by the addition to the reaction mixture of NaOH, (pH of the starting solution = 10; pH after formation of Ag NPs = 9.5) increases the difference in the reduction potentials of Ag^+/Ag (~ 0.5 V at pH =10) and Gluconic Acid/Glucose (~ -0.75 V at pH =10) thus allowing a high degree of oversaturation. It is also important to remind that an even higher reaction rate is obtained by heating the reaction mixture from room temperature up to 45°C (see experimental section).

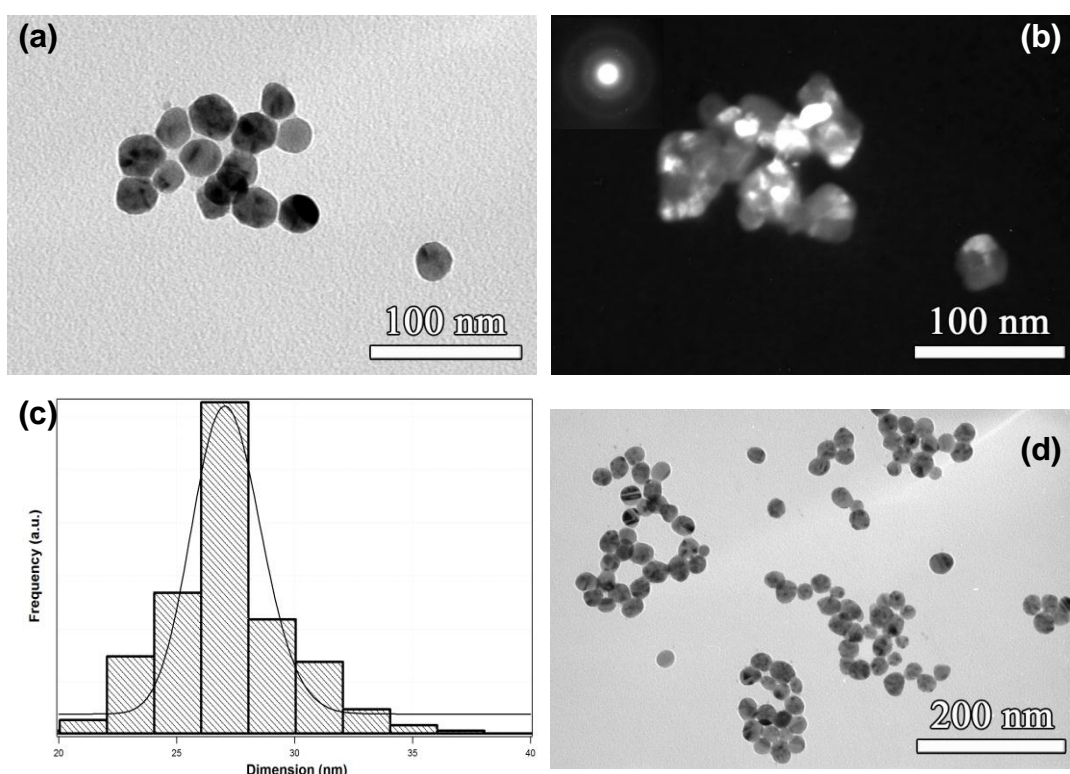


Figure 5.5 (a) TEM brightfield image of the as-prepared sample. (b) TEM darkfield image of the as-prepared sample and in the upper left corner its diffraction pattern. (c) Ag NPs diameter distribution. (d) TEM brightfield image of an as-prepared sample large area.

In **Figure 5.5d** one can see the presence of nearly spherical Ag NPs with an average diameter of 25 nm. The histogram (figure 5.5 (c)) confirms the good monodispersity of the sample, in agreement with UV-VIS data, that, as previously said, show a rather sharp plasmonic peak, typical of monodisperse systems. Figure 5.2a (bright field image) shows that the Ag NPs are actually formed by smaller crystallites, and this is even more evident in Figure 5.2b (dark field image) where it is possible to distinguish the single crystallites. The corresponding selected area diffraction pattern (SAED)

shows some halos that are due to the diffraction contribution of the smaller crystallites that form the Ag NPs aggregates (inset in Figure 5.2b).

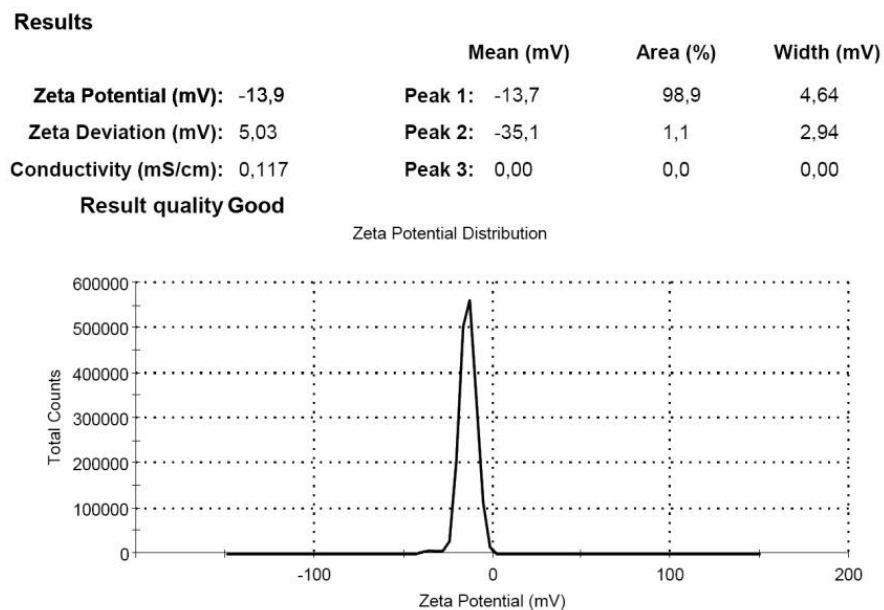


Figure 5.6 Zeta potential measurement of a fresh AgNPs solution

Zeta potential measurements (**Figure 5.6**) were carried out to understand and to study the AgNPs mobility in order to explore the possibility to deposit them by EPD. The zeta potential is the electrical potential at the junction between the Stern layer¹⁰ and the diffuse layer. If an electric field is applied, a charged particle will move with a velocity proportional to the applied field. The particle's mobility is related to the dielectric constant and viscosity of the suspending liquid and to the electrical potential at the boundary between the moving particle and the liquid. The magnitude of the surface potential (which is on the order of millivolts) is therefore related to the surface charge, to the thickness of the double layer and to the interaction with capping molecules. The measured zeta potential of the freshly prepared AgNPs solution is -13.9 mV. The negative zeta potential, probably due to the capping shell of gluconate anions that interact with the AgNPs surface in reversible way, indicates that the AgNPs synthesized by this "modified Tollens' method" can be effectively deposited by anodic EPD.

5.3.2 Preparation and characterization of the AgEPD substrates

The SiO₂/Si(100) 1cm x 1.5cm substrates are washed with deionized water and directly used for the EPD of the AgNPs. The samples can be prepared with a very easy procedure, as described in the experimental section. All the samples prepared by EPD will be called for simplicity AgEPD.

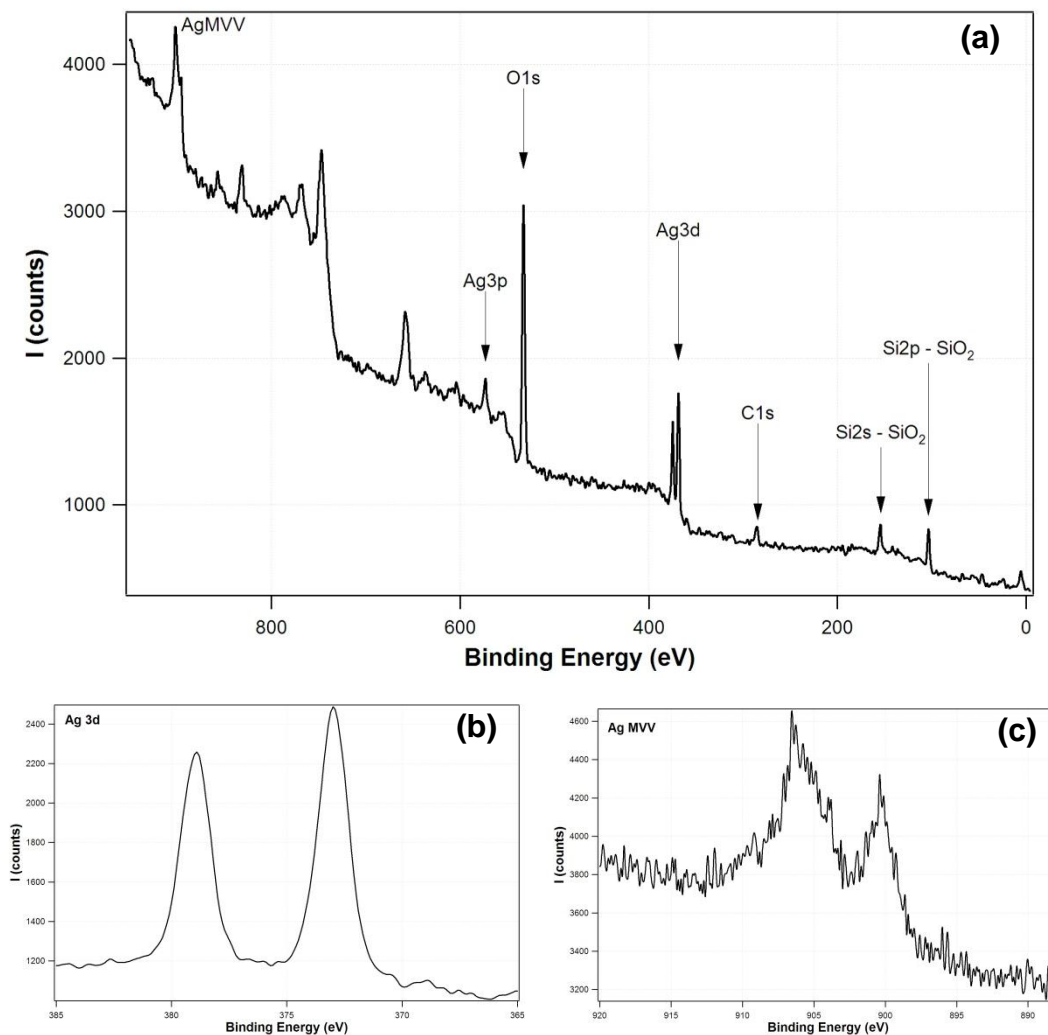


Figure 5.7 XPS spectra of the AgEPD_30min : (a) Survey, (b) Ag 3d XPS peak, (c) Ag MVV Auger peak

In **Figure 5.7a** an XPS survey scan of a freshly deposited sample at 1 mA/cm² for 30 min by anodic EPD (AgEPD_30min) is reported. Due to the insulating nature of the SiO₂ film that uniformly covers the Si wafer, in all cases the peaks are rigidly shifted to a higher BE by 4.2 eV. The data reported in the figure have been recalibrated by taking the Si 2p peak as reference. The Ag 3d (**Figure 5.7b**) and Ag MVV (**Figure 5.7c**) peaks, both

characterized by a single component, and the measured Auger parameter (726 eV) confirm the presence of only metallic Ag. The low carbon amount suggests that the AgNPs deposited on the SiO₂/Si(100) could be due to the presence of trace of organic substances adsorbed on the Ag NPs surface. In order to confirm the low contamination of organic substances, a series of FT-IR spectra of the sample as a function of EPD time were performed. The spectra were collected using a standard transmission FT-IR. Si(100) wafer are, in fact, transparent in the IR spectral region and for this reason they are ideal supports. By using IR spectroscopy, in this case, it is possible to identify the functional groups of organic species eventually adsorbed and the surface modifications of Si(100) can be clearly characterized. Silanes and silicates can be characterized easily by IR spectroscopy.¹¹

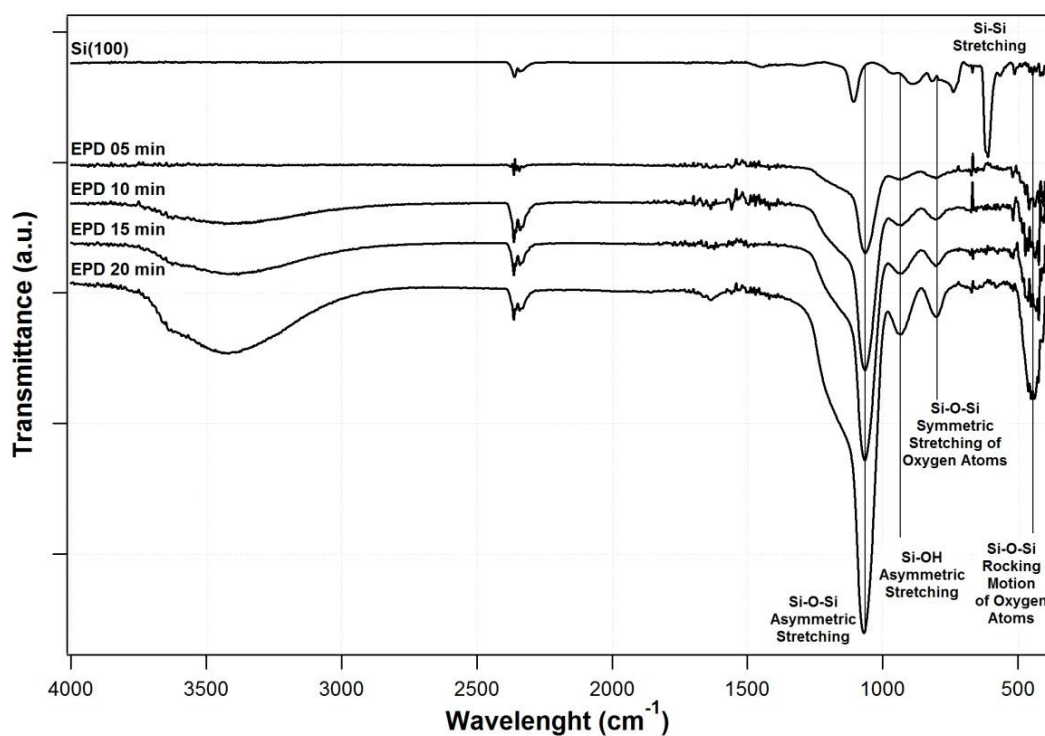


Figure 5.8 FT-IR spectra of an AgEPD sample as a function of EPD time

FT-IR spectra of the AgEPD sample as function of EPD time are reported in **Figure 5.8**. The samples spectra confirm a low organic contamination in agreement with the XPS data. The spectra appear perfectly clean and do not show glucose contamination. In the FT-IR spectrum of the AgEPD sample deposited for 20 minutes it is possible to observe the presence of a little band

at about 1600 cm^{-1} probably due to the presence of COOH groups possibly due to the gluconic acid adsorbed on the Ag NPs surface.

In the first FT-IR spectrum, recorded by using air as reference, it is possible to appreciate the low IR signal due to the SiO_2 passivation layer of the Si(100) wafer and the little absorption peak at 600 cm^{-1} due to the Si-Si-O vibration mode. Moreover, in the AgEPD spectra at 5, 10, 15 and 20 minutes of EPD four typical absorption peaks, that usually characterizes the FT-IR spectra of silanes or silicates, can be identified. In **Table 5.1** the most common FT-IR peaks of silicates are reported.

<i>Wavenumber(cm^{-1})</i>	<i>Structural Unit</i>	<i>Vibrational Mode</i>
1136 cm^{-1}	SiO_2 network	Si-O-Si Asymmetric Stretching
920 cm^{-1}	SiO_2 surface	Si-OH Asymmetric Stretching
800 cm^{-1}	Si bulk	Si-Si-O Stretching
440 cm^{-1}	SiO_2 network	Si-O-Si Rocking Motion of Oxygen Atoms

Table 5.1 Typical silanes and silicates FT-IR absorption peaks

It is clear that, during the EPD process, the anodic potential applied to the working $\text{SiO}_2/\text{Si}(100)$ electrode leads to an increase in the thickness of the SiO_2 layer. Fortunately, the increase of free Si-OH on the surface is very useful in this case. In fact, it is reported in the literature that free silanols increase the adhesion of Ag NPs on SiO_2 surfaces¹². It is possible to observe that the Si-OH peak is already visible after 5 minutes. Because of the strong interaction between Si-OH and Ag NPs the samples can be easily handled, rinsed and dried with a stream of nitrogen.

In order to better investigate on the presence of gluconic acid absorbed on the Ag NPs surface (acting as stabilizer agent), a series of SERS spectra of the Ag NPs in solution and of a freshly deposited AgEPD sample for 60 minutes, were performed.

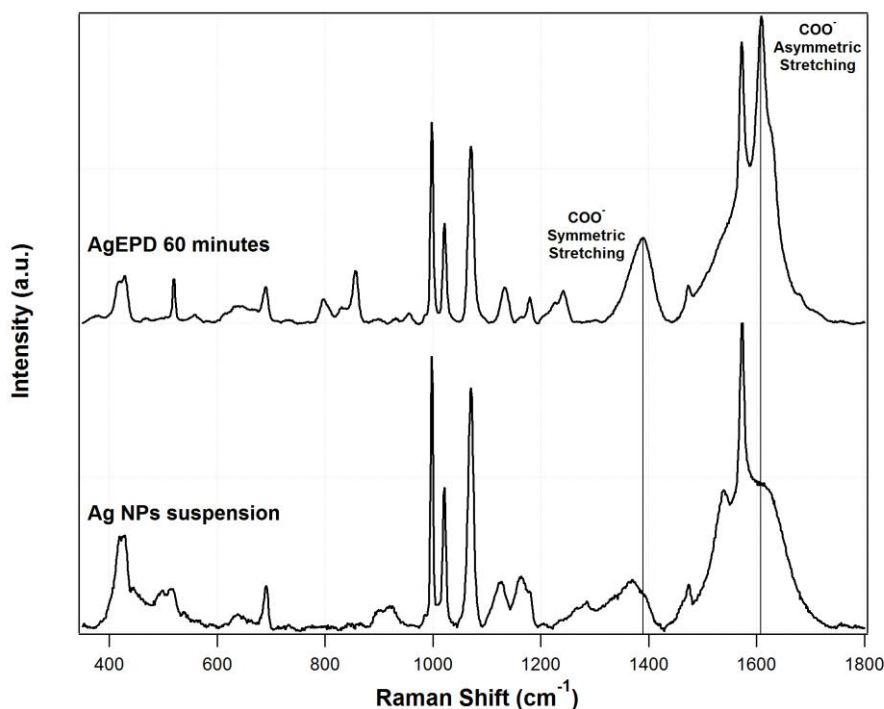


Figure 5.9 SERS spectra of gluconic acid adsorbed on Ag NPs in suspension and after 60 minutes of EPD

SERS measurements reported in **Figure 5.9**, confirm the presence of gluconic acid adsorbed on the surface of both analysed samples. The two SERS spectra have been normalized with respect the maximum in order to have qualitative information. As it is possible to observe both spectra are very similar. The stronger absorption at about 1385 cm^{-1} and 1606 cm^{-1} , due to the COO^- group of gluconate ions adsorbed on the Ag NPs surface of the AgEPD sample and their shift at higher energy, confirm the interaction between gluconate ions and the Ag NPs.

A similar procedure was performed by Osorio-Roman⁸ and in agreement with his work, the capping effect of gluconate ions on the Ag NPs was verified and confirmed. Moreover, El-Kheshen¹³, in his work, confirms that by using glucose as reducing agent it is possible to avoid stabilizers because it forms “in situ”. He studied the antimicrobial activities of Ag NPs prepared and stabilized by different ways. He demonstrates that the Ag NPs prepared by using glucose gave zero inhibition zones, because of a very effective encapsulation of Ag by gluconic acid so that there are no free Ag NPs that can damage the bacteria.

SEM measurements were performed in order to have detailed morphological information and to confirm the adhesion of the Ag NPs to the substrate. The analyzed sample is an AgEPD deposited for 30 minutes.

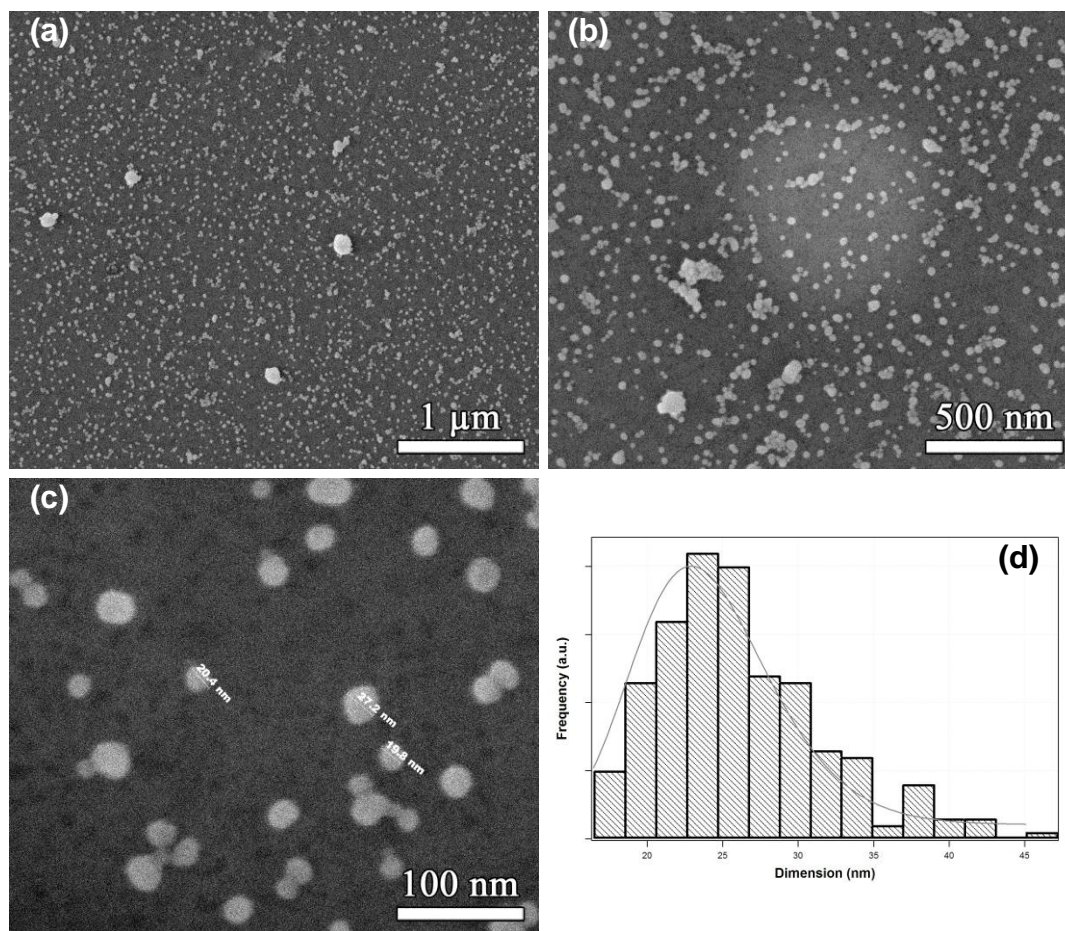


Figure 5.10 (a), (b) and (c) SEM images of an AgEPD sample deposited for 30 minutes at different magnifications; (d) Ag NPs distribution

As one can see in **figure 5.10**, the sample appears rather homogeneous with a good monodispersion of the Ag NPs. The Ag NPs maintain their original shape and do not aggregate into bigger particles on the substrate as in the case of the work published by Yang.¹⁴ In some areas aggregates are visible, but many “single” Ag NPs are visible with a defined round shape. In Yang’s work the Ag nanostructured films are prepared by Ag EPD on Si(100) with an identical methodology. The colloidal solutions used in his work were produced by laser ablation in water and were deposited under a constant current density of $50 \mu\text{A}/\text{cm}^2$. It is clear that in this case the Ag NPs average dimensions remain identical to the Ag NPs present in the starting colloidal suspension ($\sim 25 \text{ nm}$). This feature is even more evident if one compares the

histogram of the Ag NPs distribution of the Ag NPs in solution (Figure 5.5c) with that of the Ag NPs deposited on the Si(100) wafer (Figure 5.10d). On the other hand, in Yang's work the obtained films do not show particles with the same shape of those in the colloidal solution, because a significant crystal growth occurs and the Ag NPs act as building blocks of the bigger Ag NSs that forms during the EPD. The difference between the EPD method that was used in this thesis and the Yang's one is probably due to the presence of the gluconic acid and a much higher current density. It is possible, in fact, that gluconic acid, which is weakly absorbed on the Ag NPs in suspension, protects the Ag NPs from aggregation also during the EPD process and that it can be partly replaced by the free Si-OH on the Si(100) surface that anchor the Ag NPs.

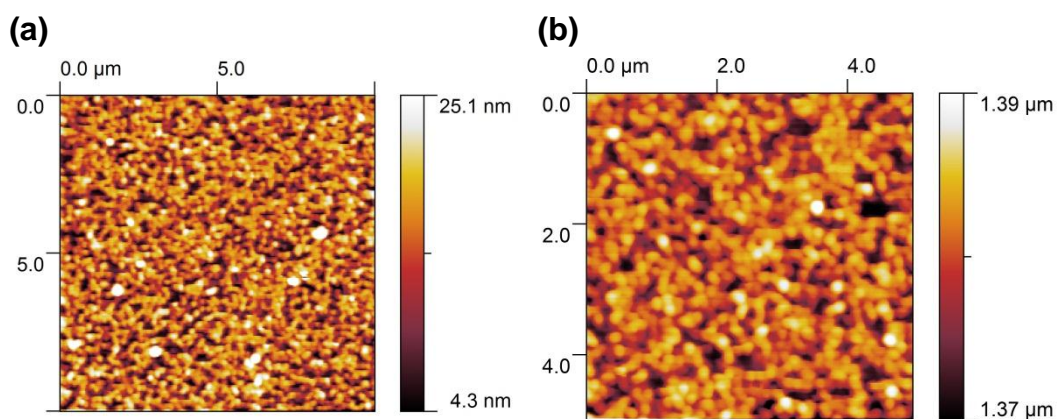


Figure 5.11 AFM images of a AgEPD sample deposited for 60 minutes

An AFM analysis was performed in order to have further information on the sample surface roughness. A series of AgEPD samples were analyzed to study the effect of the EPD deposition time on surface coverage and roughness. The AFM images of an AgEPD sample deposited for 60 minutes, reported in **Figure 5.11**, show a homogeneous Ag NPs distribution with similar dimensions. The deposited Ag NPs, as expected for an EPD, form a porous film of Ag NPs connected together, but still keeping a perfect round shape and the original dimensions. The images show that the Ag NPs couple with the close neighbors, forming a 3D network with a porous structure. From the AFM images a surface roughness of 4.7 nm was obtained and an effective SERS area, calculated assuming a threshold of 75% of the peak to valley difference, of 90% of the scanned surface (see following paragraph).

5.3.3 Optical characterization

In **Figure 5.12** the UV-Vis Diffuse reflectance measurements in the 350-850 nm range for of a clean Si(100) wafer and two AgEPD samples deposited respectively 30 minutes and 60 minutes are reported. The presence of the Ag NPs on the SiO₂/Si(100) surface can be inferred from the appearance of the plasmonic band at about 390 nm in the case of the AgEPD sample deposited for 30 minutes. Moreover it is possible to observe a broad band in the UV-VIS region between 450-700 nm due to the coupling between the Ag NPs^{15,16}, as already verified by the SEM and the AFM measurements.

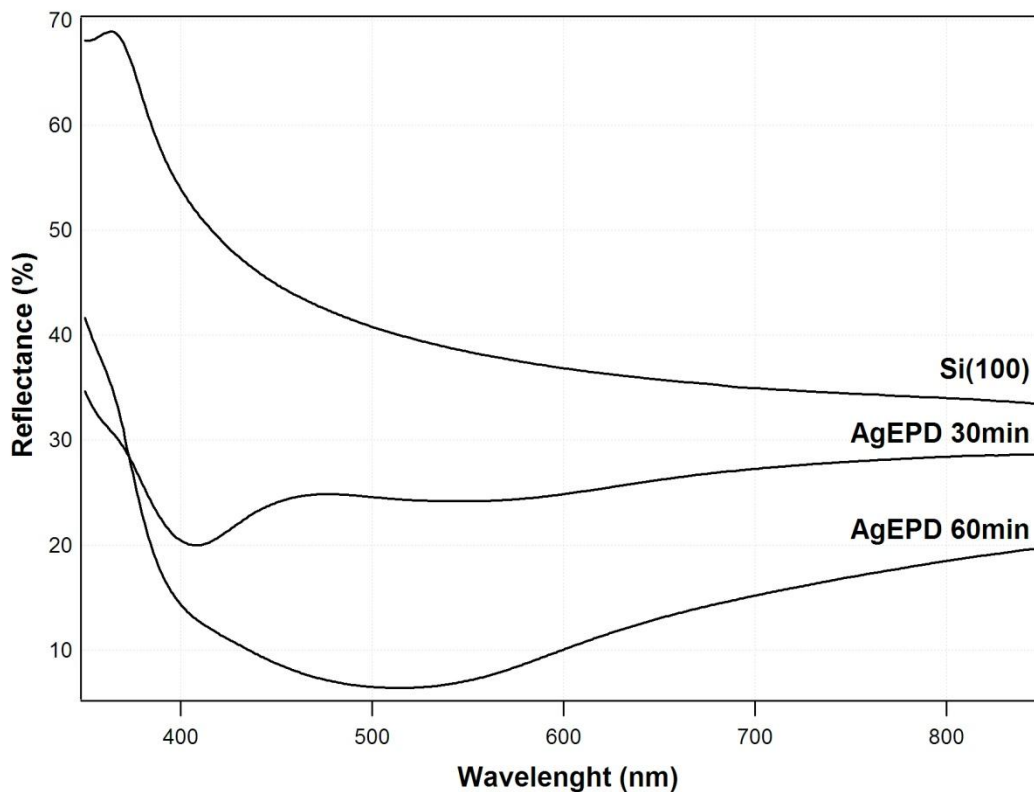


Figure 5.12 Diffuse reflectance UV-VIS spectra of a clean Si(100) wafer and two AgEPD samples deposited respectively 30 minutes and 60 minutes

It is also possible to observe that, after 30 minutes of EDP, the absolute reflectance decreases by about 15% in all the UV-ViS region and this decrease is even more evident in the AgEPD sample deposited for 60 minutes. In this case the reflectivity of the sample decreases by about 25%.

This behaviour could be very useful to improve the absorption and the efficiency of commercial silicon based photovoltaic cells in the UV-VIS region^{17,18}.

Finally, the samples were tested as SERS substrates. In this case there is no polarization dependence in the measured EF values. This is consistent with a random-like distribution of the NPs within the few μm^2 of the analyzed area (i.e. laser spot). Actually, the presence of a NPs network, that is evident from the reflectance measurements and from the SEM images, makes these supports SERS effective in the whole UV-VIS region.

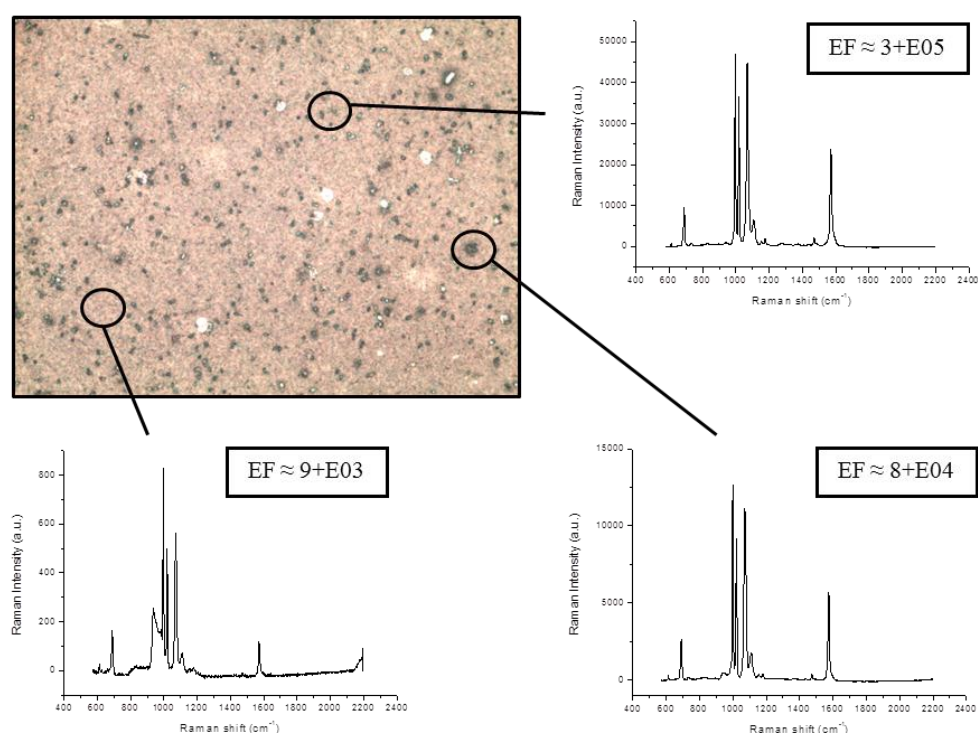


Figure 5.13 Optical microscope image and Raman map of an AgEPD sample deposited for 60 minutes

SERS characterization was carried out at 785 nm.

An Ag EPD sample deposited for 60 minutes was first analysed. The gluconic acid molecules, adsorbed on the Ag NPs surface, can be easily substituted by much stronger ligands like benzene thiols (BT). As it is possible to observe in **Figure 5.13**, the sample appears rather homogeneous on a large area. The measured EF of the BT functionalized sample is reported, for each marked area, above the corresponding SERS spectrum. It is clear that there are areas with higher EF where bigger aggregates of Ag NPs are present.

However, the average measured EF $(4.0 \pm 1.6) \times 10^4$ that be compared with those obtained using substrates prepared with more expensive techniques (see Figure 3.4 in chapter 3) is rather good.

An AgEPD sample deposited for 30 minutes was also then analyzed in order to verify the Ag NPs coverage on the SERS properties of the substrate.

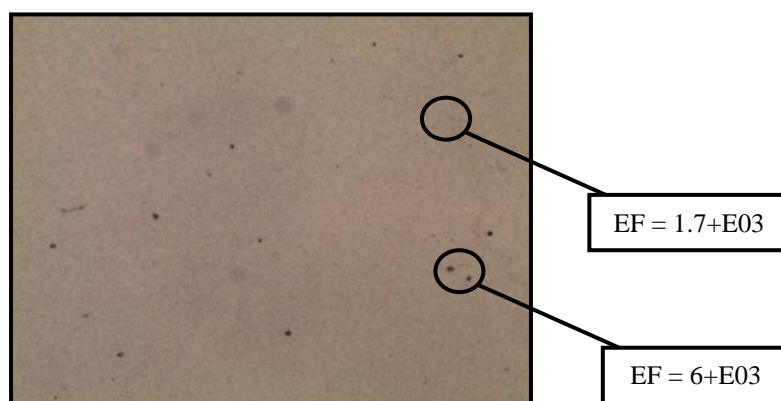


Figure 5.14 Optical microscope image and Raman map of an AgEPD sample deposited for 30 minutes

In **Figure 5.14** the optical microscope image of the sample with the measured EFs corresponding to the marked areas is reported. The sample appears more homogeneous with respect to the sample deposited for 60 minutes. In this case, on the contrary, the measured EFs result lower with respect to the previous case $((1.7 \pm 0.6) \times 10^3)$. It is obvious that the EF increases proportionally with the number of Ag NPs per unit area. However it is also clear, that by depositing for longer times, aggregation phenomena occur and the homogeneity of the sample decreases dramatically. So, it is fundamental to establish the right equilibrium between a high sensitivity (high Enhancement Factor) and a good reproducibility (low Standard Deviation). For this reason samples deposited for 60 minutes represent the right compromise between a good EF and reproducibility.

Finally, some surface enhanced infrared absorption (SEIRA) experiments on these substrates with a standard FT-IR spectrophotometer, using octadecanethiol (ODT) as probe molecule, were performed. ODT shows a strong signal in the CH_n IR region because of the presence of a C_{18} aliphatic chain. For this experiment an AgEPD sample deposited for 20 minutes was used. The sample was spray-coated with a 1% solution of ODT in ethanol

and rinsed with pure ethanol in order to remove the excess of ODT. The FT-IR spectrum of the sample was registered and a further Ag NPs EPD was performed for 5 minutes in order to create “hot spots” where ODT is “sandwiched” between 2 adjacent Ag NPs.

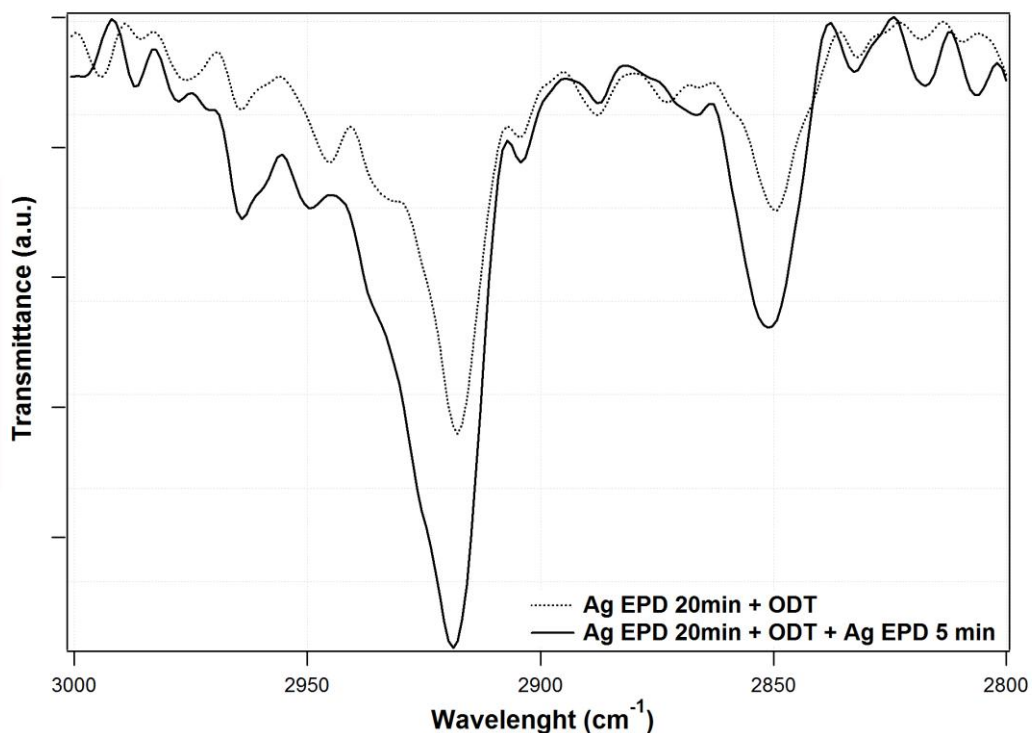


Figure 5.15 SEIRA effect on a ODT functionalized sample at the junction between the Ag NPs

In **Figure 5.15** it is possible to observe a strong signal increase due to the formation of “hot spots” after the second Ag NPs EPD¹⁹. This simple and quick experiment confirms that such samples can be easily exploited to develop analytical methodologies involving different optical characterization techniques in the plasmonic field.

5.4 Conclusions

In this last study it was demonstrated that with a simple “green synthesis” it is possible to obtain an Ag NPs suspension with a good dimensional monodispersity and good optical performances.

The EPD technique was tested and, as it was shown, can be exploited to have substrates with a high coverage of gluconic acid “protected” Ag NPs.

EDP performed on SiO₂/Si(100) wafers proved to be a valid alternative to other more expensive techniques.

The Ag NPs, after EPD, maintain their original dimension due to the “protection” of the adsorbed gluconic acid that forms during the redox reaction between the [Ag(NH₃)₂]⁺ complex and glucose. Molecules that bind more strongly to Ag, like thiols or amines, can easily substitute the gluconic acid.

This behaviour, together with the good SERS properties (EF), the easy and reproducible preparation make these AgEPD samples a practical alternative for the fabrication of cost-effective and disposable SERS substrates, possibly enabling mass production. This procedure could also be applied to commercial photovoltaic cells in order to improve the efficiency in the UV-VIS range as it was shown.

Finally, it was demonstrated that these substrates are also suitable to perform SEIRA experiments.

References

- 1 X. Yang, W. He, S. Wang, G. Zhou and Y. Tang, *J. Mater. Sci. Mater. Electron.* **2012**, 23, 108
 - 2 S. Manivannan and R. Ramaraj, *Pure Appl. Chem.* **2011**, 83, 2041
 - 3 K. M. Rahulan, S. Ganesan and P. Aruna, *Appl. Surf. Sci.* Ahead of Print
 - 4 L. Besra and M. Liu, *Prog. Mater. Sci.* **2006**, 52, 1
 - 5 M. Tejamaya, I. Romer, R. C. Merrifield and J. R. Lead, *Environ. Sci. Technol.* Ahead of Print
 - 6 Z. Khan, J. I. Hussain, S. Kumar and A. A. Hashmi, *Colloids Surf. B* **2011**, 86, 87
 - 7 P. Raveendran, J. Fu and L. Wallen Scott, *J Am Chem Soc* **2003**, 125, 13940
 - 8 I. O. Osorio-Roman, V. Ortega-Vasquez, V. C. Victor and R. F. Aroca, *Appl. Spectrosc.* **2011**, 65, 838
 - 9 L. Kvitek, R. Prucek, A. Panacek, R. Novotny, J. Hrbac and R. Zboril, *J. Mater. Chem.* **2005**, 15, 1099
 - 10 O. Stern, *Z. Elektrochem. Angew. Phys. Chem.* **1924**, 30, 508
 - 11 D. B. Mawhinney, J. A. Glass, Jr. and J. T. Yates, *J. Phys. Chem. B* **1997**, 101, 1202
 - 12 T. Tuval and A. Gedanken, *Nanotechnology* **2007**, 18, 255601
 - 13 A. A. El-Kheshen and S. F. G. El-Rab, *Pharma Chem.* **2012**, 4, 53
 - 14 S. Yang, W. Cai, G. Liu and H. Zeng, *J. Phys. Chem. C* **2009**, 113, 7692
 - 15 K. Kneipp, H. Kneipp, I. Itzkan, R. R. Dasari and M. S. Feld, *J. Phys.: Condens. Matter* **2002**, 14, R597
 - 16 E. C. Le Ru, C. Galloway and P. G. Etchegoin, *Phys. Chem. Chem. Phys.* **2006**, 8, 3083
 - 17 H. A. Atwater and A. Polman, *Nat. Mater.* **2010**, 9, 205
 - 18 S. K. Jana, A. Le Donne and S. Binetti, *J. Phys. Chem. Solids* **2012**, 73, 143
 - 19 G. H. Gu and J. S. Suh, *Langmuir* **2008**, 24, 8934
-

Chapter 6

Conclusions

Come scritto nel primo capitolo, l'obiettivo di questa tesi era la fabbricazione di substrati adatti per misure SERS ed eventualmente per sensoristica LSPR. L'esigenza era un approccio facile e possibilmente a buon mercato, naturalmente con l'idea di un possibile trasferimento per applicazioni di tipo industriale. Il primo tentativo è stato quello di usare un DVD registrabile come un substrato nano-decorato in modo da avere un migliore controllo sulla uniformità delle Ag NPs sulla superficie. Infatti ci si può aspettare, se il substrato DVD viene utilizzato come catodo in una semplice apparecchiatura elettrochimica in corrente continua, di avere una maggiore densità di corrente sulle creste delle scanalature e di conseguenza una maggiore densità di particelle. Si è così effettivamente ottenuto un substrato caratterizzato da linee di Ag NPs in corrispondenza delle creste, mentre sul fondo delle scanalature la densità delle particelle è risultata essere inferiore. Nonostante l'approccio molto semplice, la forma dendritica delle Ag NPs ha consentito di ottenere un elevato SERS enhancement factor, maggiore di 10^5 , che rende il substrato derivato dai DVD l'approccio più conveniente, considerando il rapporto prestazioni/prezzo. Il picco ben localizzato e stretto corrispondente al plasmone dell'Ag a circa 400 nm potrebbe anche trovare applicazione in un apparecchiatura per sensoristica LSPR.

Per quanto riguarda l'approccio AAO, le prime osservazioni utili ottenute sono state la crescita auto-limitata e l'effetto ombra, dovuti chiaramente alla formazione sul fondo dei pori di Ag NRs seguite da NTs quasi fino alla superficie. Il tentativo di erodere la nanostruttura di allumina, in modo da far collassare le Ag NRs per formare degli "hot spot", è stato l'esperimento

chiave che ha permesso di capire che il processo di erosione può essere effettivamente ben controllato mediante AR-XPS o spettroscopia UV-Vis. La scomparsa dell'effetto ombra o delle frange di interferenza corrisponde sempre ad una superficie con le Ag NRs ancora incorporate nella matrice residua di AAO e il resto delle Ag NSs collassate, che formano fasci di nanotubi. E' stato sorprendente constatare che quelle strutture molto interessanti (i NTs) non sono così attive durante un esperimento SERS. L'unica possibilità di avere le Ag NRs esposte, ma ancora incapsulate nella matrice di AAO era quella di provare a lavarle via mediante un trattamento in bagno ad ultrasuoni. Questa procedura molto semplice ha permesso di ottenere una disposizione ordinata di Ag NRs. La forma delle NRs non è così regolare (la loro parte superiore è caratterizzata da una forma poco definita), come evidenziato dalle immagini SEM, ma la spaziatura tra le NRs adiacenti è molto stretta e come mostrato dai calcoli DDA vi è infatti la formazione di una serie regolare di "hot spots" che si estendono oltre aree di qualche μm^2 . Semplicemente cambiando lo spessore dell'AAO (da 1 μm a 3 μm) è stato possibile ottenere un substrato adatto per la sensoristica LSPR, dove la risonanza plasmonica dell'Ag accoppiata all'interferenza di tipo Fabry-Perot hanno permesso di ottenere un comportamento sensoristico molto riproducibile. Sarebbe interessante implementare questo tipo di substrati in una cella microfluidica per misurare la concentrazione di campioni biologici in tempo reale.

Inoltre, la procedura di deposizione in corrente alternata può essere facilmente trasferita ad altri metalli come il Cu e, come è stato dimostrato, è possibile ottenere una decorazione dei pori da parte dell'Ag semplicemente immergendo la struttura AAO in una soluzione di AgNO_3 . Lo strato sottile di Ag che si forma sulla parte superiore delle Cu NRs è probabilmente anche protetto dall'ossidazione per effetto della "protezione anodica" offerta dal Cu. In fine è stata esplorata la "sintesi verde" di Ag NPs a partire da $[\text{Ag}(\text{NH}_3)_2]^+$ e glucosio, accoppiata alla deposizione elettroforetica. Questo è di fatto un approccio facile ed economico per la fabbricazione di substrati SERS. Il risultato è particolarmente interessante se si considerano le prestazioni piuttosto buone durante gli esperimenti SERS e considerando il fatto che le Ag NPs sono protette da uno strato di acido gluconico. Questo strato può

essere facilmente sostituito da leganti forti contenenti gruppi -SH o -NH₂ e al tempo stesso rende questo substrato compatibile con i campioni biologici (le NPs ricoperte dall'acido gluconico non sono bioinerti).

Ogni campione preparato in questa tesi è stato ingegnerizzato ottimizzando dimensioni e forma a seconda della sua applicazione. E' stato eseguito uno screening accurato di tutti i parametri di ogni sensore fabbricato in modo da avere una sintesi semplice, economica e ripetibile che possa assicurare un basso costo, alte prestazioni ed accuratezza analitica: i primi passi per l'implementazione su scala industriale.

Conclusions

As written in chapter one, the aim of this thesis was the fabrication of substrates suitable for SERS measurements and eventually for LSPR sensing. The requirement was an easy and possibly cheap approach, of course with the idea of a possible transfer to industrial application. The first attempt was that of using a recordable DVD as a nano-patterned substrate in order to have better control on the uniformity of Ag NPs on the surface. In fact, one can expect, if the DVD substrate is used as the cathode in a simple DC electrochemical apparatus, to have higher current density on the ridges of the DVD grooves and therefore a higher particle density. The result was indeed a substrate characterized by lines of Ag NPs in correspondence with the ridges, while at the bottom of the grooves there was a lower particle density. Despite the very simple approach, the dendritic shape of the Ag NPs allowed the obtainment of a very good SERS enhancement factor, as high as 10^5 , which makes the DVD derived substrate the most convenient approach, considering the performance/cost ratio. The well localized and narrow peak corresponding to the Ag plasmon at about 400 nm could also find application in a LSPR sensing apparatus.

Concerning the AAO template approach, the first useful obtained observations were the self-limited growth and the shadowing effect, clearly due to the formation at the bottom of the pores of Ag NRs followed by NTs almost up to the surface. The attempt to etch the alumina nanostructure so that the Ag NRs were collapsing together to form “hot spots”, was the key experiment that allowed to understand that the etching process can actually be nicely controlled by AR-XPS or UV-Vis spectroscopy. The disappearance of the shadowing effect or the interference fringes always corresponds to a surface with the AG NRs still embedded in the residual AAO matrix and the

rest of the Ag NSs collapsed, forming bunches of nanotubes. It was then surprising to see that those very nice structures (the NTs) were not so active in a SERS experiment. The only possibility to have the Ag NRs exposed, but still embedded in the AAO matrix was to try to wash them away by an ultrasonic bath treatment. This very simple procedure allowed to obtain an ordered array of Ag NRs. The shape of the NRs is not so regular (their top is characterized by an irregular shape) as evidenced by the SEM images, but the spacing between adjacent NRs is very narrow and as shown by the DDA calculations there is indeed the formation of a regular array of “hot spots” which extend over at least μm^2 areas. By simply changing the thickness of the AAO (from 1 μm to 3 μm) it was possible to obtain a substrate suitable for LSPR sensing, where the Ag plasmon resonance coupled with the Fabry-Perot like interference effect allowed to obtain a very reproducible sensing behaviour. It would be interesting to implement this type of substrates in a microfluidic cell in order to measure the concentration of biological samples in real time.

Moreover, the AC deposition procedure can be easily transferred to other metals like Cu and, as it was shown, it is possible to obtain a decoration of the pores by Ag by simply dipping the AAO structure in a AgNO_3 solution. The thin Ag layer that forms on top of the Cu NRs is probably also protected from oxidation by the “anodic protection effect” of Cu.

Finally, the “green” synthesis of Ag NPs from $[\text{Ag}(\text{NH}_3)_2]^+$ and glucose coupled with the electrophoretic deposition were explored. This is indeed an easy and cheap approach to the fabrication of SERS substrates. The result is particularly interesting considering the rather good performances in a SERS experiment and considering the fact that the Ag NPs are protected by a gluconic acid layer. This layer can be easily replaced by stronger ligands containing $-\text{SH}$ or $-\text{NH}_2$ groups and at the same time makes this substrate compatible with biological samples (the gluconic acid capped NPs are not cytotoxic).

Every prepared sample in this thesis work was engineered in order to by optimizing dimensions and shape depending on its application. An accurate screening of all parameters of every fabricated sensor was performed in order to have an easy, cheap and reproducible synthesis that can ensure low

cost, high performance and analytical accuracy: the first steps for the implementation on an industrial scale.

Ringraziamenti

Questa tesi di dottorato è stata sviluppata nell'ambito del Progetto Strategico PLATFORMS (Plasmonic Nano-Textured Materials and Architectures for Enhanced Molecular Sensing) dell'Università degli Studi di Padova ed è frutto di tre anni di duro lavoro, durante i quali, tra alti e bassi, ho ottenuto dei buoni risultati partendo letteralmente da "zero". D'altronde questo è quello che si richiede ad un dottorando.

In primis vorrei ringraziare il mio supervisore, nonché amico, Gian Andrea Rizzi, che ha sempre creduto in me e nelle mie idee, alcune volte a dir poco bislacche. Con il suo aiuto e il suo sostegno sono riuscito a crearmi un filone di ricerca nuovo all'interno del gruppo di ricerca del Prof. Granozzi, che ringrazio per avermi fornito tutti i mezzi necessari per il mio progetto di ricerca.

Ringrazio inoltre i Prof. Gennaro, Bozio, e Romanato per avermi ospitato nei loro laboratori di ricerca e per i loro preziosi consigli su alcune branche scientifiche che, fino a prima di intraprendere l'avventura del dottorato, avevo soltanto visto sulla carta.

Un particolare ringraziamento va a Christian Durante, Robertino Pilot, Vincenzo Amendola, Denis Garoli, Agnese Sonato, Verena Weber ed Enrico Della Gaspera, con i quali ho collaborato durante questi tre anni.

Inoltre voglio ringraziare i miei colleghi di lavoro e amici Luca Artiglia, Stefano Agnoli, Enrico Reeder, Marco Favaro, Dmytro Chirkov e Jian Zheng con i quali ho condiviso questi tre anni.

Infine, un grazie molto speciale alla mia Sara per avermi supportato/sopportato durante questi tre anni, e a tutta la mia famiglia per avermi sostenuto e aver appoggiato tutte le mie scelte.

